Vapor Transport Sintering of Calcium Phosphate Ceramics

Zur Erlangung des Grades eines Doktors der Naturwissenschaften (Dr. rer. nat.)
vorgelegt von Margarete Therese Schloßer, M. A., aus Rosenheim in Oberbayern
am Fachbereich Material- und Geowissenschaften
Darmstadt im Oktober 2012 (D 17)

TECHNISCHE
UNIVERSITÄT
DARMSTADT

Gutachter	1. Prof. Dr. Hans-Joachim Kleebe
	2. Prof. Dr. Christoph Schüth
Tag der Einreichung	30. Oktober 2012
Tag der Disputation	14. Dezember 2012

Erklärung der Urheberschaft

Hiermit versichere ich, die vorliegende Arbeit ohne Hilfe Dritter und ohne Benutzung anderer als der angegebenen Hilfsmittel angefertigt zu haben. Die aus fremden Quellen direkt oder indirekt übernommenen Gedanken sind als solche kenntlich gemacht. Die Arbeit wurde bisher keiner anderen Prüfungsbehörde in gleicher oder ähnlicher Form vorgelegt.

Darmstadt, den 30. Oktober 2012

_____

Margarete Therese Schloßer

To my father

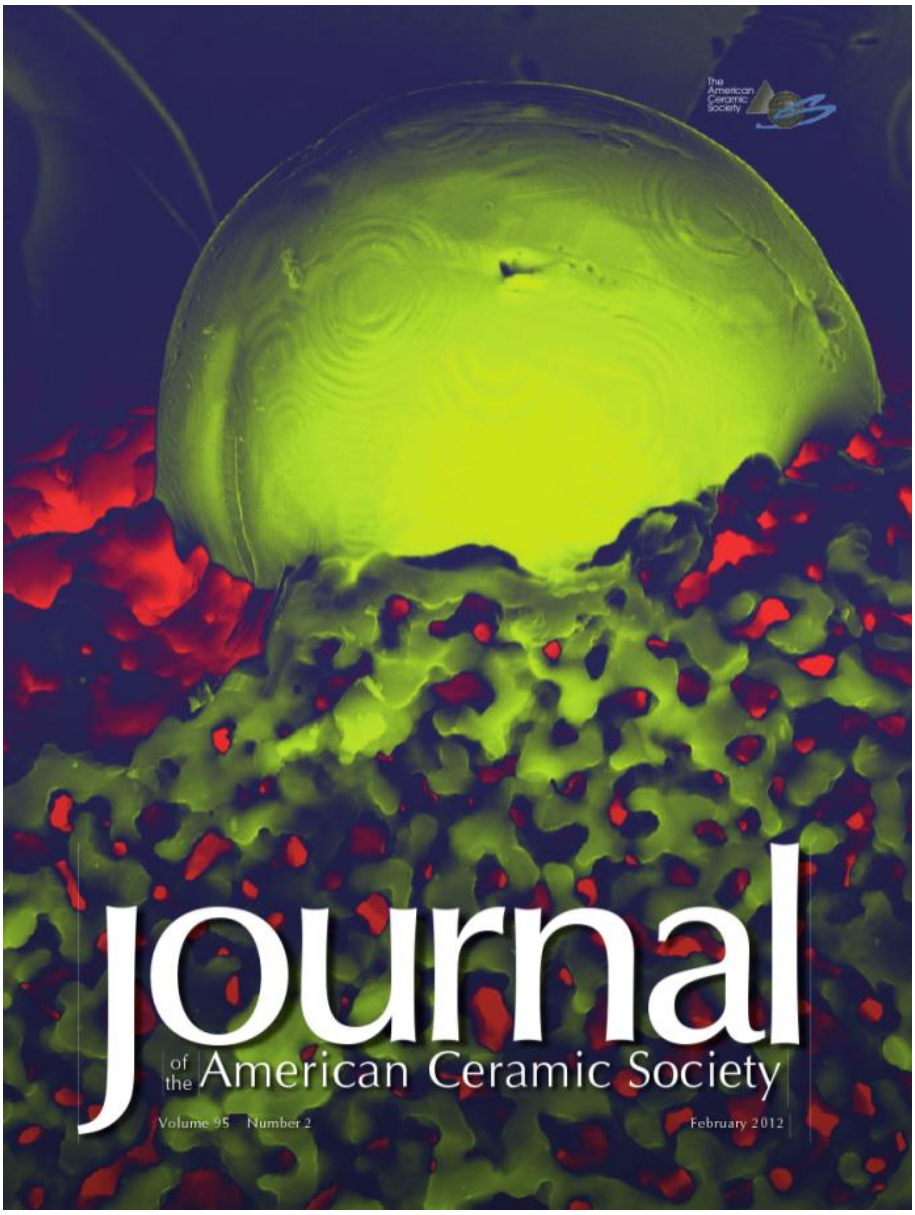

Cover image corresponding to Schlosser and Kleebe (2012) JACerS, Vol. 95(5), 1581–1587.

Table of Contents

1. Abstract / Zusammenfassung

In modern plastic and reconstructive surgery the application of biocompatible materials with adequate mechanical and chemical properties has become indispensable. For the treatment of skeletal defects, hydroxyapatite (HA) is well-established as a bone graft material. As its chemical composition is very similar to the mineralized part of human bone, this material offers excellent biocompatibility and direct mechanical bonding to the host tissue. The healing process can be further enhanced by mixing HA with the more soluble tricalcium phosphate (TCP) to adjust the implant's resorption rate to that of new tissue formation. Moreover, to stimulate bone ingrowth, it is crucial to produce ceramic scaffolds with interconnected porosity and pore diameters of 100-500 µm. Various processing methods have been proposed for the fabrication of such scaffolds. However, due to both technical and economic considerations, few of them have been scaled up for industrial production.

Our motivation was to explore vapor transport sintering (VTS) as a novel and potentially cost-effective process for the near-net shape manufacturing of custom-made implants. Starting from synthetic powder precursors, the microstructure development of HA and TCP ceramics, as well as biphasic mixtures thereof, was studied for systems with both halide acids and solid chloride agents. Chemical and phase analysis were performed to monitor potential substitutional reactions and phase conversions upon processing. Analyses were carried out with scanning electron microscopy (SEM) with integrated energy-dispersive X-ray spectroscopy (EDS), X-ray diffraction (XRD), Fourier-transformed infrared spectroscopy (FTIR) and X-ray fluorescence (XRF). Furthermore, for gathering a theoretical understanding of the vapor transport process, thermodynamic calculations were carried out for various systems. Among the foremost aims of the investigation was the identification of suitable halide reagents to enhance material transport through the vapor phase, as well as the validation whether large enough pore diameters could be generated by this processing method. As it turned out, pore coarsening stagnates after reaching diameters of about 5 µm. Thus, the combination of VTS with other processing techniques is necessary to create adequate macroporosity. The promising results obtained for sintering in AgCl atmosphere, suggested the combination of macroporous precursors with vapor transport sintering as a potential technique to create a novel composite material. For this purpose, coral skeletons and sea urchin spines were hydrothermally converted into calcium phosphate scaffolds. Subsequent AgCl-sintering not only stimulated enhanced material transport through the vapor phase, but also caused the condensation of fine Ag-bearing particles throughout the ceramic scaffold. The resulting surface modification lends anti-

bacterial properties to the composite material which are expected to decrease post-surgical inflammation risks.

In der modernen plastischen und rekonstruktiven Chirurgie ist der Einsatz biokompatibler Materialien mit geeigneten mechanischen und chemischen Eigenschaften unverzichtbar geworden. Für die Behandlung von Knochendefekten hat sich Hydroxylapatit (HA) als ein Werkstoff mit hervorragender Biokompatibilität erwiesen. Da seine chemische Zusammensetzung der des mineralisierten Anteils des menschlichen Knochens weitgehend entspricht, bietet dieses Material hervorragende Biokompatibilität und direkte mechanische Anbindung an das Gewebe. Der Heilungsprozess lässt sich durch Beimischung des leichter löslichen Tricalciumphosphats (TCP) zu HA weiter verbessern, da auf diese Weise die Resorptionsrate des Implantats an die Neubildungsrate von Knochengewebe angepasst werden kann. Um die Versorgung der knochenbildenden Zellen mit Nährstoffen zu gewährleisten, ist es von entscheidender Bedeutung, keramische Gerüste mit interkonnektierender Porosität und Porendurchmessern von 100-500 µm herzustellen. Unter Berücksichtigung dieser Anforderungen wurde eine Vielzahl von Herstellungsverfahren für derartige „Scaffolds" vorgeschlagen. Aufgrund von technischen und wirtschaftlichen Erwägungen wurden bisher jedoch nur wenige zur industriellen Produktionsreife geführt.

Unser Forschungsinteresse galt Gasphasensintern als einem neuartigen und potentiell kostengünstigen Verfahren zur endkonturnahen Herstellung individuell gefertigter Implantate. Von synthetischen Pulvern ausgehend wurde die Gefügeentwicklung von HA, TCP und biphasischen Mischungen der beiden Stoffe (BCP) für Systeme untersucht, denen entweder Halidsäuren oder feste Chloride als Sinteradditiv zugegeben waren. Chemische Analysen und Phasenbestimmungen wurden durchgeführt, um mögliche Substitutionsreaktionen und Phasenumwandlungen während des Herstellungsprozesses nachzuvollziehen. Die Untersuchungen wurden mittels Rasterelektronenmikroskopie (SEM) mit integrierter energiedispersiver Röntgenspektroskopie (EDS), Röntgendiffraktometrie (XRD), Fourier-transformierte Infrarot-Spektroskopie (FTIR) und wellenlängendispersiver Röntgenfluoreszenzspektroskopie (XRF) vorgenommen. Um darüber hinaus ein theoretisches Verständnis des Gasphasenprozesses zu erhalten, wurden für zahlreiche Systeme thermodynamische Berechnungen durchgeführt. Zu den wesentlichen Zielen der Untersuchung zählte einerseits die Identifizierung geeigneter Halid-Reagenzien, um den Materialtransport in der Gasphase entscheidend zu verbessern, andererseits die Überprüfung, ob mit diesem Herstellungsverfahren ausreichend große Porendurchmesser erzielt werden können. Wie sich herausstellte, stagniert die Porenvergröberung nach Erreichen von Durch-

messern in der Größenordnung von 5 µm. Um eine adäquate Makroporosität zu erzeugen, ist daher die Kombination von Gasphasensintern mit anderen Verfahren erforderlich. Die vielversprechenden Ergebnisse der Sinterversuche in AgCl-Atmosphäre legten nahe, makroporöse Ausgangsmaterialien dem Gasphasensintern zu unterziehen, um einen neuartigen Kompositwerkstoff herzustellen. Zu diesem Zweck wurden Korallenskelette und Seeigelstacheln hydrothermal in Calciumphosphat-Gerüste umgewandelt. Anschließendes AgCl-Sintern verstärkte nicht nur den Materialtransport in der Gasphase, sondern führte außerdem zur Kondensation fein verteilter Ag-haltiger Partikel im Inneren des keramischen Gerüsts. Diese Oberflächenmodifikation verleiht dem Kompositwerkstoff antibakterielle Eigenschaften, von denen eine Senkung post-operativer Entzündungsrisiken zu erwarten ist.

2. Literature Review

2.1. Biominerals and Biomaterials*

Biomineralization denotes the formation of inorganic solids deposited in biological systems (Mann 2001).[1] The often intricate and light-weight structures synthesized under ambient conditions from compounds abundant in nature have long been a source of inspiration for material scientists. Once designed by nature's changing course, biominerals may serve a specific purpose, such as the hard apatite fibers vertebrate teeth are composed of,[4,5] or the magnetite crystals (Fe_3O_4) of so-called magnetotactic bacteria that guide them within the earth's magnetic field.[6] Other conspicuous properties seem to have developed rather by chance, such as the characteristic shimmer of nacre, a composite material which has an astounding durability under strain, shielding mollusks from predators and tidal forces.[7] From an anthropological point of view, the most relevant class of biominerals is calcium phosphates, as hydroxyapatite (HA; $Ca_{10}(PO_4)_6(OH)_2$) forms part of our bones, tendons and teeth. According to Weiner and Wagner (1998), the term bone "refers to a family of materials each with a somewhat different structural motif, but all having in common the basic building block, the mineralized collagen fibril."[8] Human bone tissue is an intriguing example for a complex composite material with a hierarchical structure made of inorganic, organic and living components. It consists of hard apatite platelets mineralized within a fabric of tough protein fibrils, some interstitial water, as well as a variety of bone-forming (*osteoblast*), -colonizing (*osteocyte*) and -resorbing (*osteoclast*) cells, constantly remodeling the bone to adapt it to changing mechanical loads (Figure 1). Moreover, the material bone is organized on several hierarchical levels, ranging from the nano-sized basic constituents over the mineralized fibril, fibril arrays and array patterns, cylindrical arrangements of the osteons over regions of spongy or compact bone, up to the macroscopic whole.[8] There has been extensive research on the relationship between the structure of bone, including the degree of mineralization that determines stiffness (Young's modulus), and its mechanical properties;[9] values for human bone are given in section 2.3.4, Table 1. The mineral content of mammal bone depends on tissue age as well as functional requirements, ranging from 50 wt% for the cancellous bone of an agile deer to 80 % for the lumbering whale. However, the function of bone is not restricted to the mechanical stabilization of the organism, but it also acts as a reservoir for calcium and phosphate which are necessary for various metabolic processes.

* If no other source is referred to in this chapter, recourse has been made to the handbooks of Mann (2001),[1] Epple (2003),[2] as well as Wong and Bronzino (2007).[3]

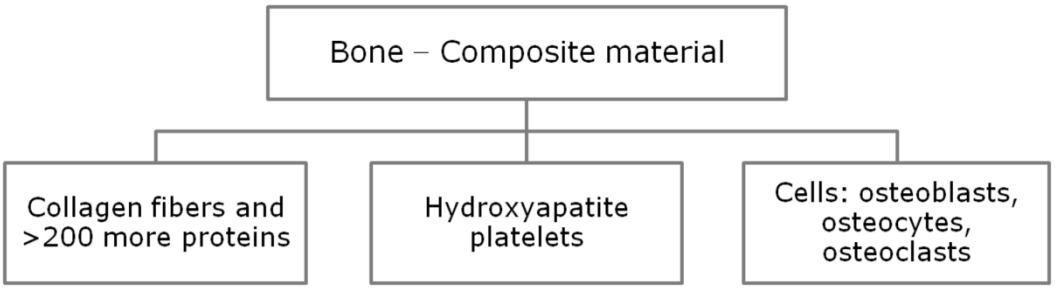

Figure 1: Constituents of human bone (after Epple 2003).[2]

Crystallites synthesized under physiological conditions are generally rather small, so that their structure is not easy to determine. "Biological" HA (mineral name: dahllite) contains Na, Mg and carbonate, among other impurities.[10,11] HA platelets in mature bone are about 50 x 25 x 4 nm in size.[12-14] In view of the hexagonal crystal symmetry of dahllite ($P6_3/m$), the oblong morphology seems unusual and may indicate growth via an octacalcium phosphate (OCP; $Ca_8(HPO_4)_2(PO_4)_4{\cdot}5H_2O$) transitional phase.[14,15] OCP has a platy and tape-like habit and its triclinic structure ($P\bar{1}$) comprising intercalated hydrated layers – metastable under the given conditions – will hydrolyze to form HA.

Some biominerals are used as precursors for the fabrication of bone replacement materials. Apart from calcined bovine bone which offers a similar chemical composition,[16,17] the highly porous structures of calcareous algae and corals have striking resemblance with human *interstitium* (interstitial bone) and can be applied directly or after hydrothermal conversion into HA.[18-21] Thus, they are transformed from a biomineral into a biomaterial.

Biomaterials restore body functions, either alone or in conjunction with electric or electronic devices (Epple 2003).[2] Modern biomaterials in clinical use, such as artificial skin or veins, hip prostheses, cardiac pacemakers or dental implants all rely on the development of materials meeting high standards regarding their mechanical, chemical and biological compatibility with bodily functions.

Mechanical compatibility comprises the reliable fixation within the host tissue, as well as sufficient strength and toughness, ideally for the remaining lifetime of the patient. However, the stiffness of the implant material should not exceed that of the adjoining host tissue to avoid the latter's degeneration (*stress shielding*).[22]

Chemical compatibility is given for a material that integrates well into the surrounding tissue without irritating it. It should be noted that bodily fluids are aggressive chemical media, due to their salt content, elevated temperature, as well as the biological activity of enzymes, macrophages and bacteria. If resorption of the implant is desired, as for most

bone graft applications, the degradation rate should match that of new tissue formation. Otherwise degradation due to corrosion or abrasive wear should be either non-existent or controlled without the release of toxic degradation products.

Biological compatibility comprises the absence of an immune response that may lead to inflammations or encapsulation of the implant, as well as non-toxic and non-carcinogenic behavior. Suitable conditions for the proliferation of bone-forming osteoblasts can be actively created by setting the appropriate pH, adjusting the surface morphology, encouraging the release of certain ions, and so on. For classification purposes, further distinctions can be made between *bioinert*, *biocompatible* and *bioactive* materials, denoting the degree of interaction with the host tissue.

2.2. Bone Implant Materials

2.2.1. General Remarks

According to the German Medical Technology Association (BVMed),[23] nearly 12.8 billion Euro are spent on medical devices annually, not including related services, making Germany the third largest market after the U.S. and Japan. Constantly rising case numbers of degenerative joint disease are the direct result of an ageing population.[24] More than 200,000 artificial hip implantations per year in Germany demonstrate the routine character of these surgical interventions.[23] Regarding bone graft applications in non-load bearing sites, the main objective is the repair of defects caused by trauma or tumor resection. Autogenous cancellous bone harvested from the iliac crest has been used as the standard graft procedure for many decades, since it combines all major requirements for the formation of new bone:[25-28]

i. Scaffolding for *osteoconduction*, i.e. the implant acts as a support for bone ingrowth to achieve strong interface bonding (HA, collagen).
ii. Growth factors for *osteoinduction*, i.e. the active stimulation of progenitor cells to differentiate into bone-forming osteoblasts (non-collagen bone matrix proteins).
iii. Progenitor cells for *osteogenesis*, i.e. the mineralization of new bone tissue.

Although considered as the ideal graft material, autogenous bone is sometimes not available in sufficient quantity, and harvesting carries the risk of complications, such as additional pain and blood loss as well as infection and donor site instability, leading to an increased patient recovery time.[29-32] To circumvent those problems, allograft bone, which is obtained from another subject of the same species (i.e. human corpses), can be freeze-dried and stored in large bone banks for later utilization. However, this approach involves

considerable expense and the risk of transmitting viruses or bacteria,[33] as well as of a deleterious immune system response.[34,35]

To avoid the general drawbacks of autografts and allografts, there is a critical need to develop new materials for bone substitution. The ideal bone substitute should be (i) tolerated by the host tissue without any adverse reaction, (ii) reveal mechanical properties similar to bone with high reliability, and (iii) be completely resorbed through the natural bone remodeling process after fulfilling its initial function to stabilize the defect.[2] Due to the differing functional demands directed at, for example, an artificial hip coating or fillers for bone regeneration in atrophic sites, compromises between material properties are necessarily made when choosing a suitable material. Over the last century, a broad range of both experimental and commercialized materials for bone repair, substitution, or augmentation have been developed comprising metals, ceramics, bioactive glasses and polymers.[3,36-39] Stress shielding due to the mismatch of the elastic moduli of implant and bone can be avoided by designing composite materials.

2.2.2. Metallic Biomaterials

Metallic prostheses are valued for their high mechanical strength. Due to their inherent elasticity and unlike brittle ceramics, they are not prone to catastrophic failure, although they may be subject to fatigue. Furthermore, their processing is comparatively cheap. However, corrosion and abrasive wear pose a medical risk, as the release of particles or ions may cause allergic or toxic reactions. The widespread use of metal implants for bone graft applications began with the invention of stainless steel in the 1920ies. Further progress was made following the ascent of titanium and its alloys after the Second World War. Due to the formation of a passivating oxide layer (TiO_2), the light metal titanium remains insoluble even under aggressive chemical conditions. For porous implant materials, tissue ingrowth has been observed which facilitates their permanent fixation.[40,41] Moreover, coating with calcium phosphates is possible, lending bioactive properties to the material.[42]

2.2.3. Polymeric Biomaterials

Polymers are another important class of materials for medical applications. Due to the advances of modern polymer chemistry, material properties (elastic/hard, degradable/durable, etc.) can be adjusted within a wide range by variation of the polymer chains. Processing techniques such as extrusion, foaming, or weaving are well-established for the

creation of complex shapes. Moreover, the chemical and/or biological functionalization of the implant's surface is possible. However, critical mechanical properties, such as mechanical strength, hardness and wear resistance, remain inferior to that of metals, whereas the relatively low density might be of advantage. In clinical practice, degradable polymers, i.e. mainly polyglycolide and polylactide, may be used as surgical threads, for wound dressings or systems for controlled drug release. Moreover, they serve as substrates for *tissue engineering* making use of extracorporally grown cells to restore bodily functions. Among the non-degradable polymers, ultra-high molecular weight polyethylene (UHMWPE) is part of tribological pairings in knee and hip prostheses, due to its high wear resistance. For fixation of artificial hips within the femur, but also to cover cranial defects, the bioinert polymethylmethacrylate (PMAA) is used as cement that hardens within minutes during surgical treatment.

2.2.4. Ceramic Biomaterials

The third major category of biomaterials is ceramics. Termed *bioceramics*, they are specially designed for the repair, reconstruction and replacement of diseased or damaged parts of the body (Hench 1998).[43] Bioceramics fall into two broad categories: *Bioinert* oxide ceramics, as well as *biodegradable* and/or *bioactive* ceramics that are mostly calcium phosphate-based. The advantageous hardness of many ceramics goes along with characteristic brittleness, making implants prone to catastrophic failure.[44-47] Thus, sophisticated processing techniques, as well as great care during handling, are required to prevent the formation of crack-inducing flaws.

Among the bioinert ceramics,[24,48,49] high-purity alumina (α-Al_2O_3; corundum) is the most widely used oxide ceramic material. It has proven particularly valuable for surgical implants subject to high mechanical loads, such as dental crowns, or joint heads and sockets of artificial hips. Its exceptional hardness – defining Mohs hardness 9 – provides structural integrity as well as outstanding resistance to abrasive wear, as surfaces with very low roughness can be obtained by polishing. Friction is further reduced by the formation of a fluid film, owing to the good wettability of alumina. Pairings of alumina-alumina yielded better clinical results than other tribological systems, such as alumina-UHMWPE and metal-UHMWPE, for total hip replacement.[22] For long-term stability in orthopedic applications, ceramic processing is optimized to achieve a microstructure that is fine-grained, homogeneous and near-theoretical density. Another advantage of alumina is the excellent corrosion resistance under aggressive physiological conditions. However, its presence in the human body provokes the formation of a fibrous membrane encapsulating

the implant. Thus, bioinert ceramics can only be attached to the host tissue by mechanical interlocking or tissue ingrowth into jagged surfaces.

An alternative hard ceramic material is zirconia (ZrO_2; Mohs hardness 8½) used in orthopedic and dental applications. Specific advantages over alumina are its higher fracture toughness and flexural strength due to a transformation toughening mechanism impeding crack propagation.[50] However, due to an increasing awareness of high fracture rates related to implant ageing, the formerly widespread use of Yttria-stabilized zirconia balls (Y-TZP) for femoral head replacements has stalled.[51-53] In search of alternatives, research has focused on alumina-zirconia composites.[54] Also, zirconia ceramics are increasingly used in dental applications, partly because of their aesthetic benefits. Other types of dental ceramics are based on alkali feldspars used for the embellishment of metal-ceramic bridges as well as for all-porcelain crowns. Also into the category of bioinert ceramics fall pyrolytic carbon coatings deposited on metal substrates, making mechanical heart valves resistant to blood clot formation.[55]

Introduced by Hench,[56,57] silica-based bioglasses derive their bioactive properties from their CaO (30-35%) and P_2O_5 content (10-15%). Depending on the amount of SiO_2 added, they can be made bioinert or -degradable. Bioactive behavior, i.e. direct bonding between implant and bone, is facilitated by the creation of suitable conditions at the implant's surface causing the nucleation of carbonate-substituted HA followed by cell attachment and bone mineralization. Biodegradable ceramics are subject to resorption upon implantation, while new bone tissue is formed in their place. Regarding other biodegradable ceramics, natural corals (Biocoral®)[21,58,59] and the rapidly dissolving calcium sulfate hemihydrate,[60,61] better known as Plaster of Paris, have received less consideration despite good clinical results. However, the materials that most closely resemble the composition and properties of human bone are based on calcium phosphate.[62,63] In the following, the discussion will focus on calcium phosphate ceramics as a well-established bone graft material that combines acceptable mechanical properties with excellent bioactivity.

2.3. Calcium Phosphate Ceramics

2.3.1. General Remarks

The first clinical attempt to use a calcium phosphate (CaP) material to repair a bone defect was reported by Albee as early as 1920.[64] For the last 30 years, CaP bioceramics have been routinely used in medicine and dentistry.[65-68] Recent applications include bone substitution or augmentation, cement pastes for implant fixation, coating of orthopedic

and dental prostheses, as well as controlled drug delivery through material degradation.[63,69,70] Depending on whether mechanical stability, resorbability or related properties have priority for a given application, different CaP phases or phase mixtures may be used. CaP materials generally show excellent biocompatibility, osteoconductive properties, and the capability to bond directly to newly formed bone tissue.[71,72] Despite these advantages, insufficient mechanical stability of the brittle CaP ceramics is considered a major drawback and, thus, purely ceramic (non-composite) materials have not achieved wide acceptance.[37,73]

Based on their specific composition, commercially available calcium phosphate biomaterials are classified as sintered or unsintered hydroxyapatite (HA), calcium deficient apatite, biphasic calcium phosphate (BCP), α- or β-tricalcium phosphate (TCP; $Ca_3(PO_4)_2$), and so on. Stoichiometric CaP phases have Ca/P ratios in the range of 0.5-2.0. Their thermodynamic stability is dependent on temperature and humidity.[74] As a general rule, lower Ca/P ratios correspond to higher solubilities in water.[75] At body temperature and physiological pH, HA with a Ca/P ratio of 1.67 will form as the stable phase (Figure 2). However, owing to kinetic effects during precipitation, amorphous CaP and octacalcium phosphate (OCP) occur as transient phases.[76]

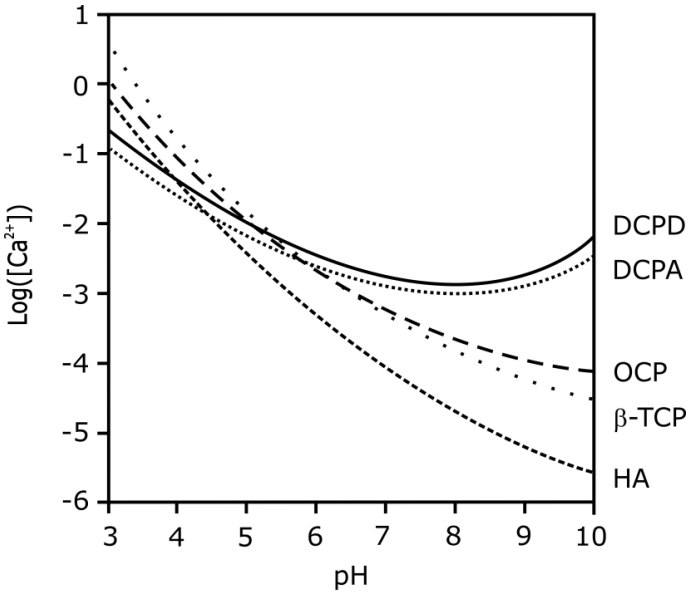

Figure 2: Stability of calcium phosphate phases as a function of pH (after Nancollas and Zhang 1994).[77] DCPD: dicalcium phosphate dihydrate ($CaHPO_4 \cdot 2H_2O$), DCPA: dicalcium phosphate ($CaHPO_4$), OCP: octacalcium phosphate ($Ca_8(HPO_4)_2(PO_4)_4 \cdot 5H_2O$), β-TCP: β-tricalcium phosphate ($Ca_3(PO_4)_2$), HA: hydroxyapatite ($Ca_{10}(PO_4)_6(OH)_2$).

Pure HA has a monoclinic structure ($P2_1/b$) at room temperature,[78] converting to hexagonal ($P6_3/m$), if the columnar anion ordering is destroyed at elevated temperatures or due to the presence of impurities and/or vacancies.[79] The apatite structure is quite flexible and various substitutions are possible at all ionic sites (Ca^{2+}, PO_4^{3-} and OH^-).[80] Commercial HA materials can be derived from natural precursors including certain corals, algae, or bovine bone.[16-20] Similar to human bone, these HA products contain impurities; for example, coral-derived HA typically contains Na, Mg and Sr derived from the marine habitat of the precursor, as well as CO_3 incorporated during processing (c.f. chapter 5).[81,82] Stoichiometric HA can be synthesized via precipitation from solutions prepared from a range of calcium- and phosphate-bearing compounds.[81,83-85] Another possibility is synthesis via solid state reaction using a stoichiometric precursor mixture that converts at temperatures above 950°C.[86,87] In the presence of water, HA remains stable up to 1550°C, whereas unhydrated phases such as TCP and tetracalcium phosphate (TTCP; $Ca_4(PO_4)_2O$) will form in dry atmospheres and may persist as metastable phases upon cooling.[74]

TCP occurs in two structural modifications, α-TCP (monoclinic: $P2_1/a$) and β-TCP (rhombohedral: $R3c$). As TCP cannot precipitate from solution, it is commonly produced by calcination of Ca-deficient HA (CDHA; $Ca_{10-x}(HPO_4)_x(PO_4)_{6-x}(OH)_{2-x}$ with $0<x<1$) with a Ca/P ratio adjusted to 1.5 at temperatures above 700°C.[84,88] Solid state synthesis is equally possible.[89,90] At 1125°C, the reversible conversion of β-TCP into the high-temperature modification α-TCP takes place; the latter phase is stable up to 1430°C.[70] However, the α–β transformation temperature is strongly influenced by impurities, so that a range of values can be found in literature.[91] By quenching, α-TCP can be stabilized at room temperature. The Mg-bearing variety of β-TCP (Mg-TCP; $(Ca,Mg)_3(PO_4)_2$; mineral name: whitlockite) has been discovered in pathological mineralizations, such as dental calculus, salivary and bladder stones. Its solubility is lower compared to pure β-TCP and hydrolysis into apatite is hindered.[92,93] As observed experimentally, the Mg-substitution stabilizes β-TCP also during VTS (c.f. 5.3.1). Moreover, Zn-substituted β-TCP was reported to slow down resorption, while stimulating bone formation.[94,95]

2.3.2. Ceramic Processing

Densification of calcium phosphate ceramics is usually performed via sintering at temperatures above 1000°C.[66,96] Overheating to temperatures above ca. 1250°C both enhances excessive grain growth and causes the β → α-TCP phase transformation, accompanied by a volume increase of 7.1 % that weakens the fabric.[70,97] Also, overheating may cause HA decomposition inflicting damage on the ceramic due to uncontrolled gas release from de-

hydroxylation.[98] Dense HA ceramics, defined as having less than 5 % porosity by volume, can be obtained by compaction and free sintering or by hot isostatic pressing (HIP).[91,99] However, for many orthopedic and dental applications, highly porous scaffolds are the material of choice, e.g. for bone graft materials,[69,100] granulates used for drug-delivery,[101-103] as part of composite materials,[104-107] or as substrates for tissue engineering.[108-112] Various methods have been proposed for manufacturing CaP ceramics with interconnected porosity such as the hydrothermal conversion of marine invertebrate skeletons,[82] sintering with porogens,[101,113,114] gravity sintering,[115] infiltration of polymer foams,[116,117] gel-casting,[118,119] freeze casting,[120] colloidal crystal templating,[103] and rapid prototyping.[121] Moreover, CaPs are used as coatings of Ti-based prostheses applied in load-bearing sites where the superior mechanical properties of metals are indispensible.[122] Layers of ca. 50-200 µm thickness are sufficient to facilitate strong bonding between implant and host tissue without the need for cementation.

2.3.3. Implant Resorption and Tissue Response

Calcium phosphate ceramics are bioactive, meaning that they are capable of forming direct interfacial bonds with the host tissue.[123] However, various clinical studies have produced partly inconsistent results about the success of treatments with CaP bone graft, alone and in combination with organic additives, depending on processing parameters of the different materials (grain size, surface properties, impurities, etc.), the cell lines used for testing, as well as the specific applications.[70,124-130] Improved results have been reported for CaP as an extender combined with autograft or osteoinductive bone protein extract.[126,130]

As yet, commercial biomaterials do not imitate the complex composite structure of human bone. However, modern calcium phosphate implants mimic the scaffold structure of the so-called *interstitium* (interstitial bone) that acts as a supporting framework without being physiologically active.[100] Osteogenesis (i.e. bone formation) crucially depends on vascularization and, thus, presupposes an interconnected pore structure with average pore diameters of 100-500 µm.[131-136] In addition, tissue ingrowth into the porous scaffold promotes the biomechanical fixation of the implant. Moreover, it has been reported that pore geometry and volume influence protein production and osteogenic differentiation of human mesenchymal stem cells.[137,138] Alternatively, osteoinductive behavior may rely on the concentration of bone growth factors within the pore space of ceramic scaffolds,[139] but there are conflicting hypotheses abound regarding the mechanisms of CaP osteoinduction, as summarized by Daculsi.[69]

Generally, HA ceramics degrade only very slowly, thus impeding resorption through the natural bone remodeling process.[140] Although chemically similar to the mineral content of human bone, pure HA implants gave unsatisfactory results in clinical applications, since they showed good osteoconductive properties, but no intrinsic osteoinductive ability.[125,141-144] Regarding TCP, α-TCP is more reactive than β-TCP in both aqueous media and *in-vivo*. It hydrolyses readily into CDHA or, occasionally, into OCP.[93,145-147] Therefore, its biomedical applications are mostly confined to self-setting cements.[148] In contrast, β-TCP does not dissolve or hydrolyze spontaneously *in vivo* in the absence of cell activity,[93,147] but it is fully resorbed during new bone formation and remodeling within a period of two years.[149] In a comparative study, pure β-TCP combined with bone marrow aspirate gave results better than HA and its performance came closest to autograft.[125] However, β-TCP resorption is rather too fast, thus promoting mechanical instability of the implant site.[66,149] It is nevertheless one of the major ceramic bone substitutes today and widely used for the fabrication of porous granules and scaffolds with applications in bone reconstruction, augmentation of the alveolar ridge, the correction of deformities, and many others.[70]

As osteoclastic degradation of β-TCP is much faster than that of HA,[150] the properties of biphasic mixtures of both phases can be adjusted to the rate of new bone formation.[69] Coined by Nery et al., the term BCP designates a ceramic material with variable amounts of 20-65% HA blended with TCP.[151] In the late 1980ies, systematic studies were conducted to optimize biodegradation controlled by the phase ratio.[152-157] Several commercial products have been developed on this basis and a phase mixture of about 60 % HA and 40 % TCP has become most common (e.g. MBCP®, Biomatlante, France; Osteosynt®, Einco Ltd., Brazil; Triosite®, Zimmer, U.S.A.).[69] Macroporous BCP ceramics offer good osteoconduction, as proven by bone formation within the pores after a few months.[158-160] "Ultraporous" BCP scaffolds carrying autogenous osteoprogenitor cells from bone marrow aspirate gave particularly good results in animal testing.[161] Due to mechanical limitations, however, the application of CaP scaffolds is generally confined to non-load bearing sites.[162,163]

2.3.4. Mechanical Properties

Relatively poor mechanical properties of calcium phosphate ceramics still prevent their application as bone graft materials in load-bearing sites. Moreover, as pointed out by Zyman,[164] values given in the literature for HA vary considerably between 200-918 MPa for compressive strength and 15-196 MPa for fracture strength of bulk ceramics. It has been demonstrated in various studies that apart from porosity,[117] ceramic processing conditions

play a crucial role in determining the mechanical properties of both HA and BCP ceramics.[163,165-167] Target values for bulk and scaffold materials are set by the mechanical properties of human cortical and cancellous bone, respectively, as summarized in Table 1.[163,168]

Table 1: Reference data for the mechanical properties of human bone (after Wagoner Johnson and Herschler 2011).[163]

	Compressive strength (MPa)	**Flexural strength (MPa)**	**Tensile strength (MPa)**	**Young's Modulus (GPa)**	**Porosity (%)**
Cortical bone	130-180	135-193	50-151	12-18	5-13
Cancellous bone	4-12	n/a	1-5	0.1-0.5	30-90

Numerous attempts have been made to improve the mechanical properties of both monolithic and scaffold Ca-phosphate ceramics by reinforcement with stronger and tougher oxide ceramics, i.e., TiO_2, Al_2O_3 and/or ZrO_2.[169-177] Similarly, ceramic metal composites have been developed using the reinforcing properties of metal fibers[178] and particulates.[179] Moreover, additions of β-TCP to HA reportedly have some positive effect on the mechanical properties. Raynaud et al.[97] observed a strengthening effect for hot-pressed HA ceramics due to β-TCP loading which could not be related to a variation of porosity or grain size. Phase fractions of about 10 wt% β-TCP were shown to double tensile strength as compared to pure HA. However, in the meantime, diverging results have been published by independent groups that on the one hand confirmed the mechanical strengthening effect for BCP ceramics relative to pure HA, but on the other hand gave inconsistent optimum values for β-TCP contents of about 30 and 40 wt%, respectively (Figure 3).[180,181] As hardness, mechanical strength and toughness of pure β-TCP ceramics are inferior to those made of pure HA,[70,81] the cause of this strengthening effect for phase mixtures remains unclear. Other research groups reported a deterioration of mechanical properties for HA/β-TCP ceramics with increasing β-TCP-contents,[163] but this may partly be caused by overheating (c.f. 2.3.2).

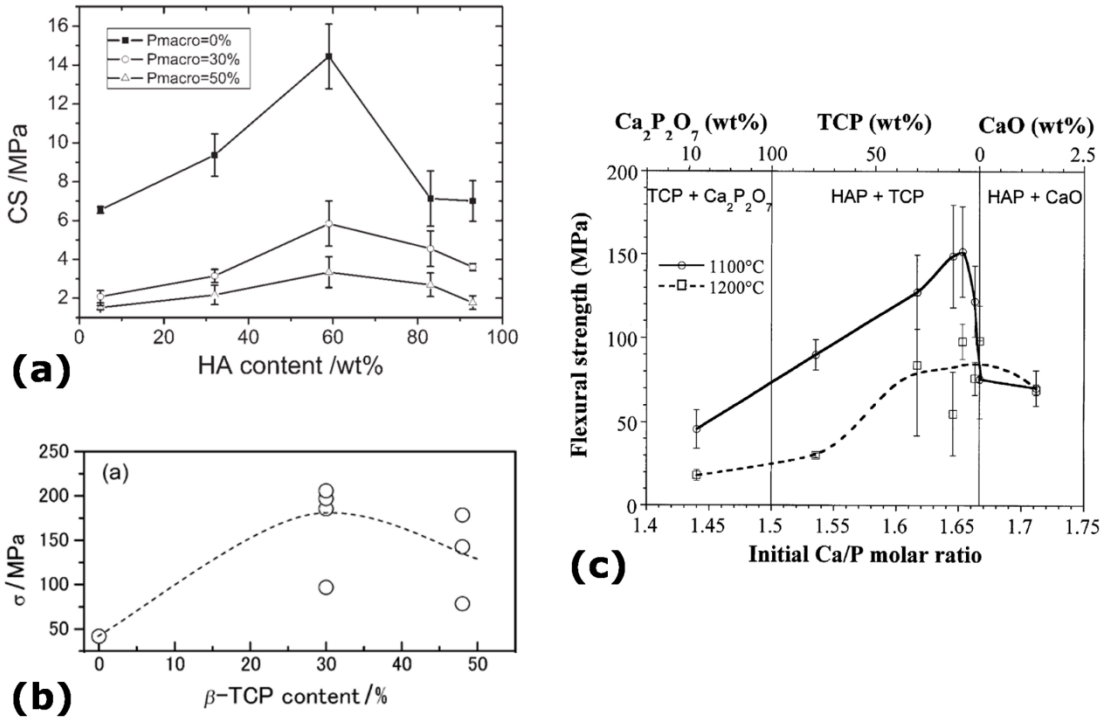

Figure 3: Literature data for (a, c) flexural and (b) compressive strength for BCP ceramics as a function of phase content.[97,180,181]

2.3.5. Antibacterial Modifications

In recent years, numerous studies have been conducted on Ag-modified calcium phosphate ceramics, as they are expected to decrease post-surgical inflammation risks.[182,183] The antibacterial properties of silver have been demonstrated in various studies for both HA and β-TCP ceramics. HA powders,[184-187] coatings,[188-192] and bulk ceramics[193,194] have been investigated as carrier materials for Ag (nano-)particles, whereas only very few studies have been concerned with β-TCP,[195,196] and BCP ceramics.[197,198] It is generally accepted that the antimicrobial effect is directly related to the release of Ag^+ ions which inhibit the proper functioning of the bacterial ribosome, as well as that of some enzymes and proteins, and have an adverse effect on bacterial DNA replication without impairing the cytocompatibility (i.e. compatibility with human cells) when present in moderate amounts.[199-201] There has been speculation on the substitution of Ag^+ for Ca^{2+} during wet synthesis of HA, but this reaction has not been verified convincingly, as yet.[186,190,194] Better supported seems the formation of silver orthophosphate (Ag_3PO_4) during the wet synthesis of HA powders. [187] As this compound is very sensitive to light, it may have escaped detection with XRD in some cases. Generally, microbial growth is inhibited in the presence of metallic, ionic and colloidal silver.[202-204] In chapter 5, a novel CaP-AgCl composite with antibacterial properties will be presented.

3. Analytical Methods

3.1. X-Ray Diffraction (XRD)[†]

X-rays are electromagnetic waves with wavelengths of approximately 100 pm. As this is on the same order as the interatomic distances of crystalline matter, the latter may act as a three-dimensional diffraction grating under irradiation. This was recognized by Max von Laue in 1912 who, by his theoretical work, laid the foundations for X-ray diffraction as the principal technique for structure determination. To interpret interference patterns formed by diffraction, lattice planes can be regarded as a stack of mirrors with spacing d_{hkl} that reflects the incident radiation (Figure 4).

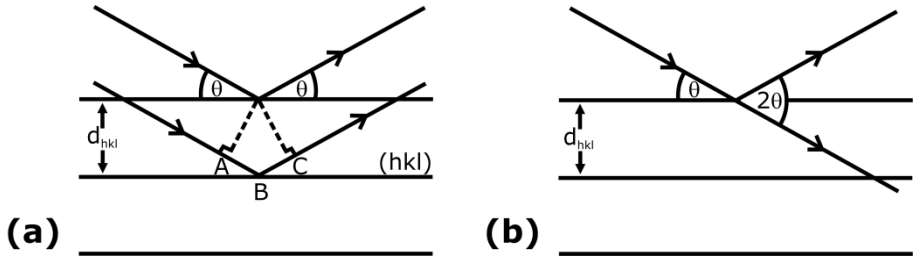

Figure 4: Graphic representation of the Bragg condition: (a) path difference between X-rays "reflected" from successive planes; (b) X-rays incident on a set of planes at Bragg angle θ are diffracted through an angle 2θ (after Putnis 1992).[206]

The portion of the beam that passes the first "mirror" unscattered may interact with the second or third layer of atoms and so on. The correlation between wavelength, λ, Bragg angle, θ, and lattice plane ("mirror") spacing, d_{hkl}, is given by the Bragg equation.

$$n\,\lambda = 2\,d_{hkl}\,sin\theta \qquad \text{(Bragg equation)}$$

Constructive interference occurs if the path difference between reflections from adjacent planes is equal to an integral multiple, n, of λ. For monochromatic X-radiation (λ = const.), constructive interference takes place at certain glancing angles (*Bragg angles*). For the identification of crystalline phases, the glancing angles measured are used to calculate lattice plane spacings which are then compared to data sets of well-defined structures. For this study, reference to the *Powder Diffraction Files* (PDF) database of the Joint Committee on Powder Diffraction Standards was made.

In the original experimental setup of von Laue, polychromatic X-rays were collimated onto a single crystal, as certain wavelengths would fulfill the Bragg condition without requiring

[†]In writing this section, recourse has been made to the handbooks of Atkins (1994),[205] Putnis (1992),[206] and Skoog et al. (1997).[207]

an exact orientation of the sample. An alternative method using monochromatic radiation was soon developed by Peter Debye, Paul Scherrer and, independently, Albert Hull. By preparing powder samples, they found a simple way of obtaining crystallites with statistical orientation. For example, a fraction of the crystallites will be oriented in such a way that their (1 1 1) planes with spacing d_{111} produces a reflection at glancing angle $2\theta_{111}$. Due to the random angular orientation around the incident beam axis, the reflections are confined to the surface of a cone with aperture semi-angle 2θ (Figure 4b). As other crystallites contained in the sample meet the Bragg condition for different d_{hkl} values, they will produce reflections corresponding to a set of cones whose positions and intensities are recorded as the diffractogram.

Powder XRD is a standard technique for phase identification and the determination of lattice parameters for single phases and mixtures. The phase composition of powdered samples was analyzed in Bragg-Brentano geometry using Cu-K_α radiation (PW 1050/25 Goniometer, Philips, Almelo, The Netherlands) and 40 kV acceleration voltage. Interaction of the electrons with the anode material causes the emission of a continuous X-ray spectrum (*Bremsstrahlung*) superimposed by characteristic lines of the target (c.f. 3.3, Figure 8). Monochromatic radiation is obtained using a graphite filter to isolate the Cu Kα line which is then collimated onto the sample. More information on the generation of X-rays is provided in section 3.3. During measurement, continuous rotation of the sample around its axis increases the number of particles contributing to the diffraction pattern.

The most common instrumental setup is the reflection configuration in Bragg-Brentano geometry, where the specimen is mounted at the center of the *measurement circle* on which X-ray source and detector are positioned (Figure 5). Moreover, the sample is oriented tangentially to the *focusing circle*. To retain focusing conditions during measurement, sample and detector are simultaneously rotated through an angle θ and 2θ, respectively. Ideally, the sample should be curved with a radius changing along with that of the focusing circle. In practice, however, the error introduced by the flat sample geometry is negligible in many cases and the configuration is called "para-focusing". The diffracted intensity at each position 2θ is recorded by a dedicated counter.

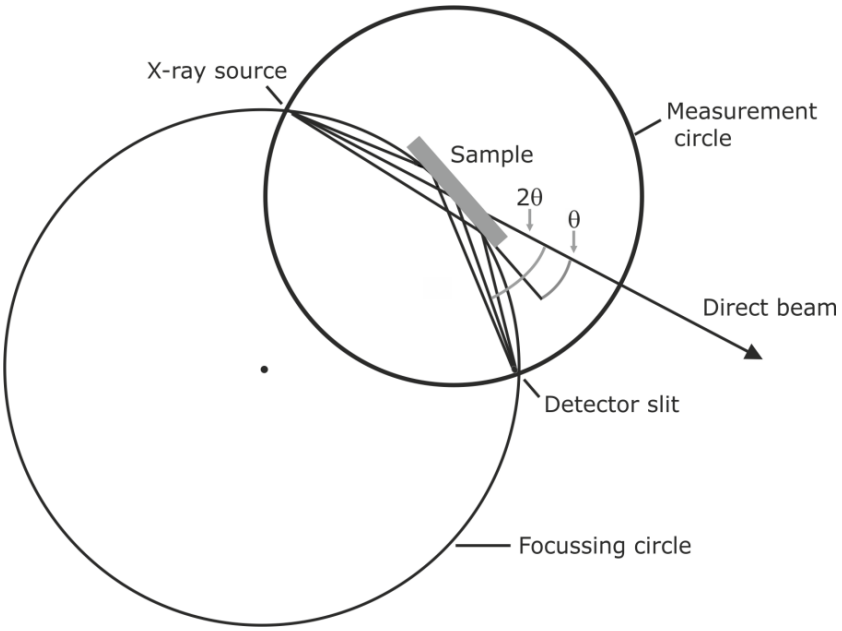

Figure 5: Bragg-Brentano geometry for X-ray powder diffraction (after http://upload.-wikimedia.org/wikipedia/commons/4/4a/Bragg-Brentano-Geometrie.jpg).

3.2. Fourier-Transformed Infrared Spectroscopy (FTIR)[‡]

Molecules are made of atoms with a given mass and geometrical arrangement which are connected by elastic bonds in periodic motion. Molecular bonds have fundamental vibrational frequencies that correspond to specific energy states of the molecule. If all atoms in a molecule vibrate with the same frequency and phase, although the amplitude may differ, this is called a *normal vibration*. All atomic motions relative to each other can be described as a superposition of normal vibrations together defining the vibrational spectrum of a substance. There are two main types: *stretching vibrations* that change the bond length and *bending vibrations* which modify the angle between two bonds (Figure 6). In a Cartesian coordinate system, each atom has three degrees of motional freedom. Defining the motion of a molecule, translational, rotational and vibrational motions need to be taken into account. A molecule containing n atoms possesses 3n degrees of freedom and, thus, 3n-6 vibrational motions which change the distances between atoms, or 3n-5 in case the molecule is linear.

Transitions between vibrational energy levels can be induced by infrared (IR) radiation which will be absorbed at the frequency corresponding to the vibrational modes in the sample. For a mode to be IR-active, an oscillating electric field of the incident IR radiation must be able to interact with a changing molecular dipole moment associated with the

[‡]In writing this section, recourse has been made to the handbooks of Putnis (1992),[206] Schrader (1995),[208] and Skoog et al. (1997).[207]

vibration (c.f. Raman spectroscopy: polarizability). For example, the HCl molecule has a strong dipole moment, as the chlorine has a higher electron density than the hydrogen. Thus, the resulting charge distribution is not symmetric and an electrical field is established. As the molecule vibrates, a regular variation of the dipole moment occurs. Incident IR-radiation is absorbed, if its frequency exactly matches the vibrational frequency of the molecule. Most molecular species absorb IR-radiation. Exceptions apply where symmetry prevents a net change in dipole moment from a particular vibration, such as in homonuclear compounds like H_2 and Cl_2, or the symmetric stretching vibration in the linear CO_2 molecule.

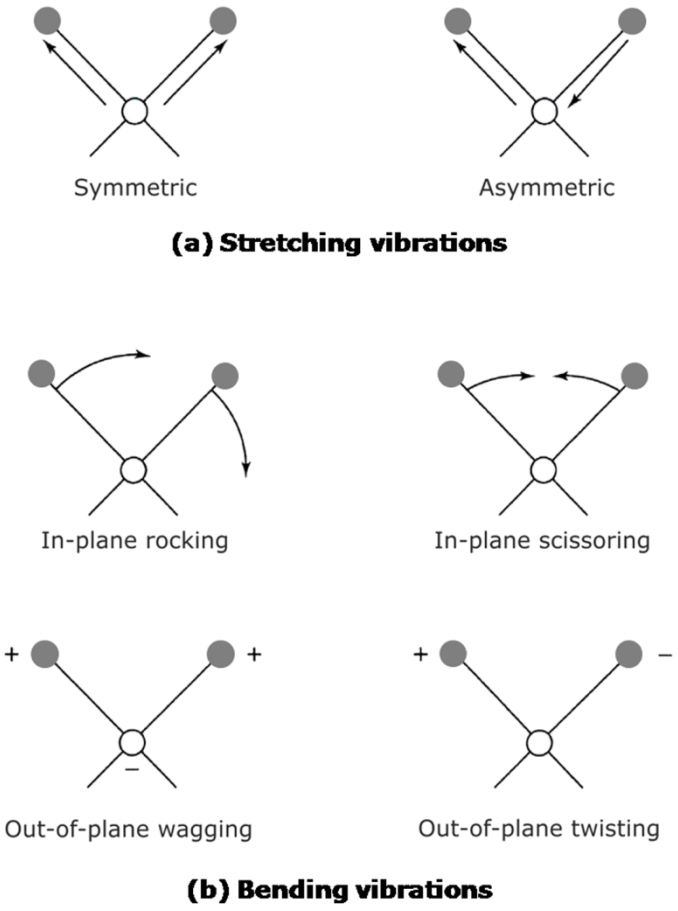

Figure 6: Schematic of molecular vibrations: (a) stretching vibrations and (b) bending vibrations (after Skoog et al. 1998, Fig. 16.2).[207]

Moreover, vibrational spectra can be recorded for substances in any physical state – solid, liquid or gaseous – and the method is particularly suitable for the analysis of low atomic weight compounds. In molecular aggregates, such as crystals, vibrations of the individual components are coupled producing overtones and combinations of normal modes. Consequently, one particular peak cannot be simply related to a molecular group as if it was

isolated and substances are identified by comparison with reference spectra. Qualitative and quantitative analysis is possible, as band intensities in the spectrum of a mixture are usually proportional to the concentration of the individual components.

Fourier-transform spectrometers are the most widely used instrument type today, as they facilitate rapid qualitative and quantitative measurements with high spectral resolution and reproducibility. As the measurement is carried out simultaneously over the whole spectral range, another notable advantage is the high signal-to-noise ratio that can be achieved in relatively short time. Basically, an interferometer splits the IR beam into two and recombines them introducing a variable phase shift to obtain periodic intensity fluctuations (Figure 7). The Fourier transform operation is then used to reconstruct the sample signal modulated onto the incident beam.

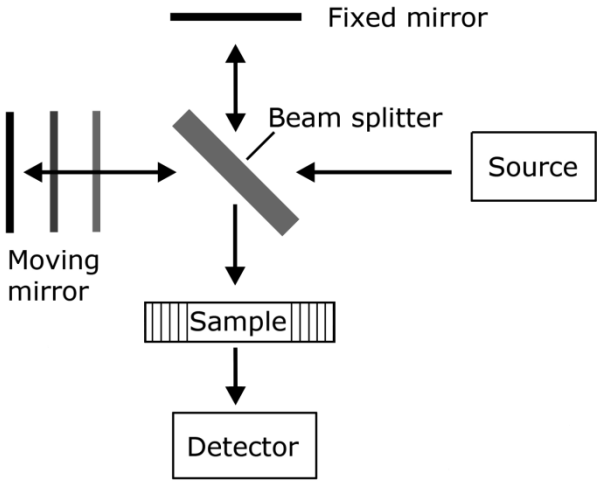

Figure 7: Schematic setup of a Fourier-transformed infrared spectrometer (after Rocksolid manual, Bruker, Karlsruhe, Germany).[209]

For the analysis of rough surfaces and powder samples, diffuse reflectance infrared Fourier-transform spectroscopy (DRIFTS) is a particularly suitable method. Other than in the conventional transmission geometry, the DRIFTS signal consists of both radiation reflected from the sample's surface and some part that has been scattered, often several times, due to interaction with the sample material. Due to the rough sample surface, radiation is diffusely reflected in all directions.

Measurements were carried out with a VERTEX 70™ instrument (Bruker, Karlsruhe, Germany) with Praying Mantis™ diffuse reflection attachment (Harrick Scientific Products, Pleasantville, U.S.A.) and a nitrogen-cooled MCT-detector (HgCdTe). A Globar source (SiC rod) was electrically heated to 1500 K, thereby emitting a continuous radiation spectrum

approximating that of a blackbody. This experimental setup allows qualitative analysis of powders and rough surface solids without further preparation in the spectral range of 7500-850 cm^{-1}. Resolution was set to 4 cm^{-1} and 1200 spectra were measured for each sample. Non-absorbing KBr powder was used as a reference to determine the background signal.

3.3. X-Ray Fluorescence Analysis (XRF)[§]

Fluorescence is the spontaneous emission of light by materials under irradiation, whereby the emitted photons have a lower energy than the absorbed ones. X-ray fluorescence denotes the emission of "characteristic", i.e., element-specific, X-radiation corresponding to the discrete energy transitions of electrons from a higher to a lower orbital. The emission of a strongly bonded inner shell electron may be caused by X-rays, electron or particle beams. Resulting electron "holes" are subsequently filled up from an outer orbital under the emission of an X-ray quant. Electron transitions are classified with respect to the location of the hole, whereas the Greek subscript denotes the outer shell orbital from which the electron that fills up the vacant site originates. Derived from the German words *kurz* and *lang*, the shortest wavelength group is called the K series, followed by the longer L series; towards the outer orbitals, if present, the classification is then going on in alphabetical order.

The relationship between the wavelength of the K_α-line radiation, λ, and the atomic number, Z, is linear, as stated by Moseley's law:

$$\frac{1}{\lambda} = A\,(Z - B)^2 \qquad \text{(Moseley's law)}$$

With constants A and B.

Maximum absorption is obtained if the energy of incident photons is slightly above the binding energy of the inner shell electron which needs to be overcome. Higher photon energies favor transmission, but an overvoltage ratio of 1.5 to 3 is common for maximum quantum yield.

For the analysis of biogenic carbonates, samples were ground to a fine powder, blended with wax and pressed into tablets (40 mm). Wavelength-dispersive XRF (WDXRF) analysis was conducted with an S8 Tiger™ instrument (Bruker, Karlsruhe, Germany). By applying a voltage of 30 kV, electrons emitted from a heated tungsten filament are accelerated to-

[§]If no other source is referred to in this section, recourse has been made to the handbooks of Hahn-Weinheimer et al. (1984),[210] Mommsen (1986),[211] Putnis (1992),[206] and Skoog et al. (1997).[207]

wards a rhodium anode. Interaction of the electrons with the metal target causes the emission of a continuous X-ray spectrum (*Bremsstrahlung*) overlain by characteristic lines of the anode material (Figure 8).

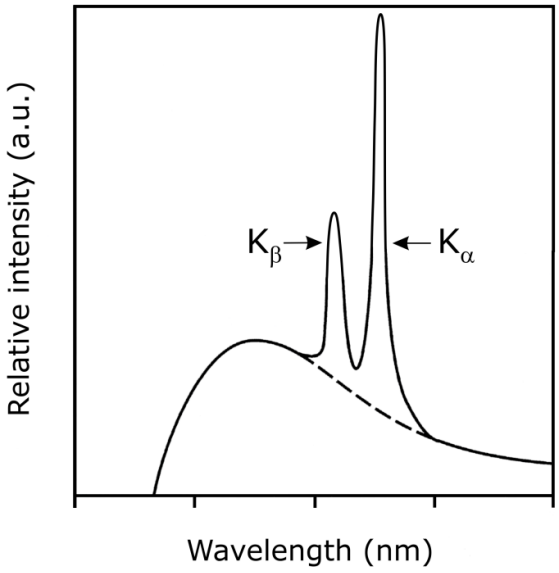

Figure 8: Schematic line spectrum of an X-ray tube with metal target (after Skoog et al. 1997).[207]

The maximum energy of the emitted spectrum, expressed in keV, is equal to the value of the acceleration voltage in kV, whereas the minimum energy is limited by absorption in the beryllium (Be) window of the X-ray tube. This instrument setup allows the measurement of Be – U, as those elements all have characteristic lines below 30 keV. The probe beam is collimated onto the sample from which characteristic X-ray quants are emitted.

In a WDXRF setup, the sample signal is diffracted by an analyzing crystal of known lattice parameters and orientation (c.f. 3.1). To cover the whole energy or wavelength range, several crystals with variable lattice spacings are rotated for sequential peak measurement. Only wavelengths satisfying the Bragg equation will be detected at a given setup angle. Peak intensities are measured by either a gas-flow (Be – Cu) or scintillation detector (Cu – U). For background correction, the signal is measured within a frame comprising the theoretical peak position.

A typical X-ray fluorescence spectrum shows the characteristic lines of all electron transitions that fall into the given energy range, as well as peaks deriving from Rayleigh and Compton scattering of the probe beam within the sample. As the wavelength of the emitted X-radiation is element-specific, immediate qualitative determination of the chemical composition is possible. In first approximation, the intensity of the fluorescence signal is

proportional to the concentration of the element in the sample. To account for the variable absorption properties of the sample's constituents, as described by the *mass attenuation coefficient*, μ/ρ, quantification is facilitated by comparison with standards of similar chemical composition. The *mass absorption coefficient*, μ, is dependent on the wavelength of the incident radiation, as well as the atomic number of the absorbing element, but not on the latter's chemical or physical state. For a specific sample, it is derived by adding the specific attenuation coefficients in proportion to the weight fractions of the elements contained. Tables for μ/ρ are provided in the literature.[210] The beam intensity after passage through the sample, I_x, is described by the Lambert-Beer law:

$$I_x = I_0 \cdot e^{-(\mu/\rho)\rho x} \qquad \text{(Lambert-Beer's law)}$$

With incident beam intensity, I_0, sample (absorber) density, ρ, and absorber thickness, x.

Apart from absorption effects, fluorescence radiation emitted by one element may cause the excitation of another within the sample (*secondary fluorescence*), adding to the signal intensity. WDXRF instruments are valued for their high peak resolution and sensitivity for major and trace element analysis. By calibration with standards of similar chemical composition, relative error of <1% can be achieved for major elements. Another quantification method, the fundamental parameter approach, can be applied if all elements present in a sample are qualitatively known. With regard to fundamental physical parameters, matrix effects are accounted for and the chemical composition can be calculated. However, errors of 2-5 % for major elements are rather common.

3.4. Scanning Electron Microscopy (SEM)**

Electron microscopy extends our visual resolution capacity to the nanometer scale. With little preparative effort, scanning electron microscopy (SEM) provides a wealth of information about a sample's surface topography and chemistry. Further advantages of electron imaging over light microscopy are the large depth of field and a broad magnification range of 10x to >100.000x accessible within a single instrument.

For imaging and analysis, a fine electron beam is generated, accelerated and focused with electromagnetic lenses to a spot size of ca. 5-200 nm (Figure 9). Guided by two pairs of electromagnetic coils with variable potential, the probe beam scans over the sample's surface in parallel lines covering a rectangular area of the sample's surface. Among the various interactions of the probe beam with the sample, the emission of both *secondary*

**In writing this section, recourse has been made to the handbooks of Flegler et al. (1993),[212] Goldstein et al. (2003),[213] Putnis (1992),[206] and Skoog et al. (1998).[207]

electrons with energies of a few tens of eV, as well as of high-energy *backscattered electrons*, is particularly relevant for SEM imaging. The respective signal is detected, amplified and displayed in synchronism with the scanning movement of the electron probe. Another important beam – sample interaction, the electron-induced emission of characteristic X-ray photons, is discussed in chapter 3.5.

Interactions of the primary beam with the specimen take place within a pear-shaped sample volume, whose size depends directly on the acceleration voltage and inversely on the average atomic number. Generally, the penetration depth from which analytical information is derived is on the order of a few µm.

Back-scattered electrons (BSE) derive from the probe beam. After numerous collisions within the sample, they exit the surface with about 60-80% of their former energy, carrying information about both chemical composition and surface topography. The probability of repeated elastic scattering events, which may deflect an electron by angles of more than 90°, correlates positively with the atomic number. Thus, local variations in the sample's chemistry are directly visible as an image contrast on the screen. As the back-scattered beam has a diameter of a few µm for bulk samples, image resolution is principally limited to this value.[212] For the detection of highly energetic BSEs, a solid-state detector is commonly employed.

Under bombardment from the primary beam, weakly bound *secondary electrons* (SE) are ejected from the solid. Although they are produced throughout the penetration volume, SEs reaching the detector originate from a depth of only 5-50 nm, due to strong absorption within the sample. With energies of 3-5 eV, they exit the sample as a beam with a diameter that is only slightly widened relative to the incident beam. Therefore, they are suitable for high-resolution imaging. The amount of SEs detected correlates with the sample's topography: higher signal intensities are recorded from areas facing the detector, as compared to averted ones. Moreover, few SEs are emitted from flat planes, whereas many more exit at edges and pikes because of reduced absorption. Taken together, the image formed by SEs reproduces the sample's topography in fine detail and can be readily interpreted. The emitted current is measured by a so-called Everhardt-Thornley detector: collected from a wide solid angle, the low-energy electrons are "sucked" into a Faraday cage by a small positive potential (300 V), then accelerated (12 kV) and detected as electrical impulses by a scintillation transducer. High-energy BSEs, which are more difficult to deflect from their path, will contribute to the signal only if they are incidentally moving towards the scintillator.

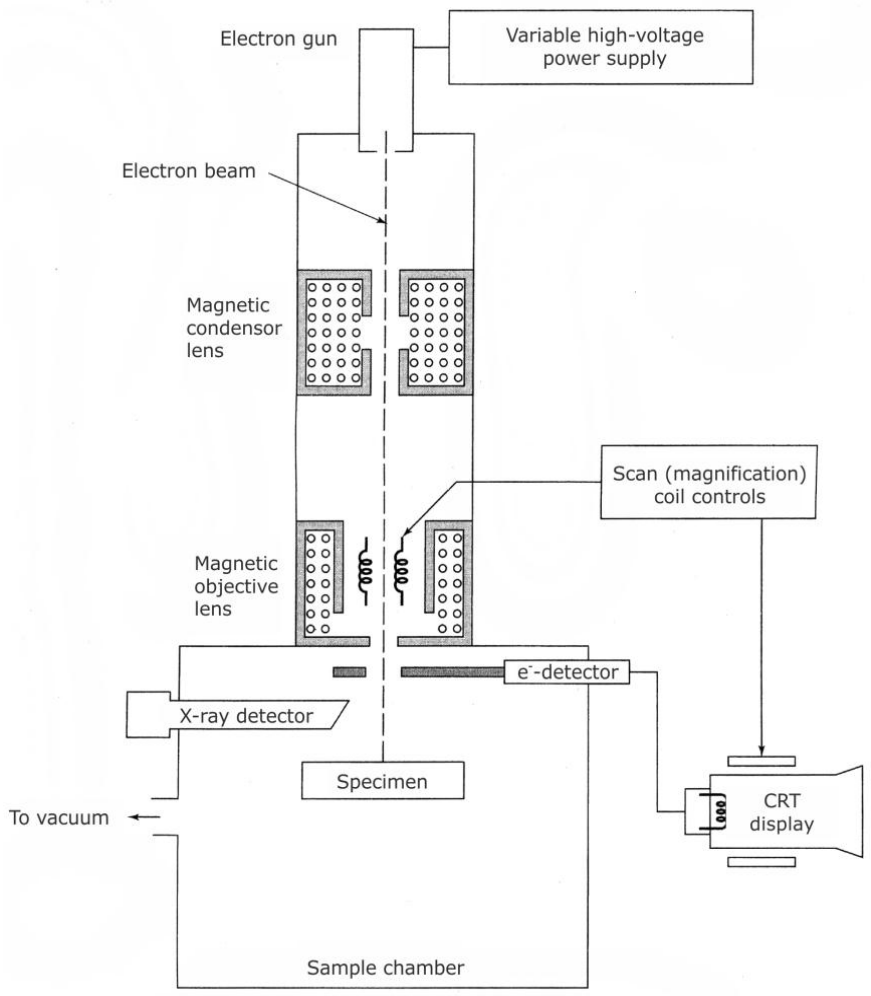

Figure 9: Schematic setup of a scanning electron microscope (after Skoog et al. 1998).[207]

Sample characterization was performed using a Quanta 200F instrument (FEI, Eindhoven, The Netherlands; high-vacuum mode) with field emission electron gun (FEG) operated at 20 kV. The instrument is equipped with an EDS system (EDAX, Mawah, NJ, United States), as specified in chapter 3.5. Fracture and polished surfaces of bulk ceramics were carbon sputtered to minimize charging by the electron beam.

3.5. Energy-Dispersive Spectroscopy (EDS)[††]

Analogous to X-ray fluorescence analysis (c.f. 3.3), the emission of characteristic X-ray quants can be stimulated by an electron beam. Characteristic X-radiation can be used to obtain qualitative and quantitative chemical information using an SEM instrument (c.f.

[††] If no other source is referred to in this section, recourse has been made to the handbooks of Flegler et al. (1993),[212] Goldstein et al. (2003),[213] Hahn-Weinheimer et al. (1984),[210] and Skoog et al. (1997).[207]

3.4) with an integrated energy-dispersive detector, employing a common electron source and focusing system. With an energy-dispersive detector setup, the simultaneous measurement of the whole energy spectrum facilitates rapid spot and line scans, as well as mappings revealing the spatial distribution of elemental concentrations. However, a major drawback is the reduced spectral resolution of energy-dispersive systems (135 eV), as compared to wavelength-dispersive ones (10 eV), and the chemical sensitivity is limited to parts per thousand. The spatial resolution depends on material properties and ranges from 5 µm for metals to 30 µm for organic matter.[212] Imaging capability (SE, BSE) and the precise control of the location analyzed provide major advantages over methods in which X-ray sources are used for excitation.

Energy-dispersive X-ray spectroscopy (EDS) was performed with an EDAX spectrometer (Mawah, NJ, United States) integrated into the SEM specified in chapter 3.4. As all elements have at least one spectral line in the range of 0-20 keV, a scan measurement was performed prior to mapping. Then, the operating voltage was reduced to 10 kV, corresponding to an overvoltage ratio adjusted to the highest relevant energy line, i.e. the $K\alpha_1$-line of calcium (3.69 keV).[214] Characteristic X-radiation was detected with a nitrogen-cooled semi-conductor transducer equipped with an ultra-thin window (UTW). Incident X-ray quants produce electron-hole pairs in the detector that lead to increased conductivity, whereas the height of the current pulse is directly proportional to the energy of the quant absorbed. For data processing and evaluation, the EDAX Genesis software package (version 6.20) was used.

3.6. Ion-Selective Potentiometry[‡‡]

An electrochemical cell (also *voltaic* or *galvanic cell*) is a device that produces an electrical potential as a result of spontaneous chemical reactions taking place within it. These reactions occur at the surfaces of two electrodes, each of which dips into an electrolyte (Oxford Dictionary of Chemistry).[216] The potential of a half-cell, i.e. between a single electrode and the electrolyte, cannot be measured directly. However, it can be determined relative to another half-cell used as a reference. Ion-selective electrodes (ISE) are customized to determine the concentration of a specific ion in solution by measuring the *electromotive force*, which is a historical designation for the potential of an electrochemical cell, against a reference electrode. Commercially available ISE setups consist of two such half-cells, either implemented as two separate electrodes, as shown in Figure 10, or as

[‡‡]If no other source is referred to in this section, recourse has been made to the handbooks of Mortimer (1986)[215] and Skoog et al. (1997),[207] as well as the WTW instrument manual.

combined instruments with an internal reference. The most common application is the pH-meter which is sensitive to H^+ ions.

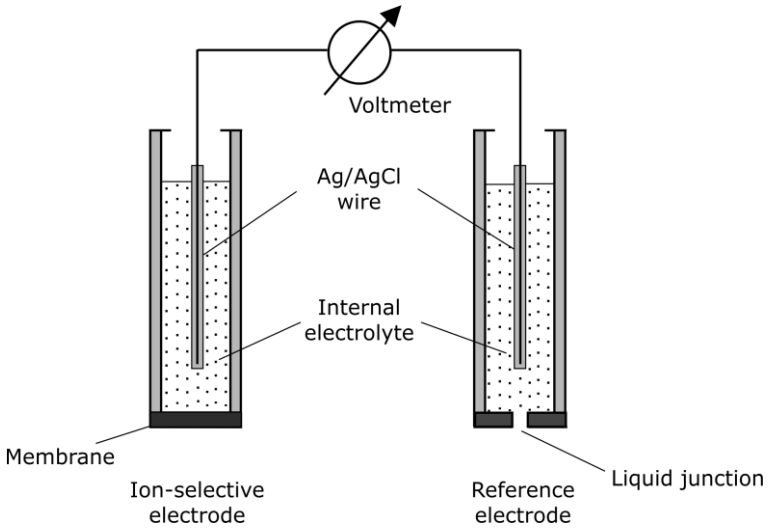

Figure 10: Schematic setup of an ion-selective measurement chain (after http://www.chemistry.nmsu.edu/Instrumentation/ISE_1.gif).

A robust and widely applied reference setup is the Ag/AgCl electrode consisting of a silver wire coated with an AgCl layer and immersed in KCl solution of a given concentration. Ag^+ ions are released from the wire into the electrolyte, thus establishing both an equilibrium ionic concentration and a constant half-cell potential.

The half-reaction at the reference electrode is:

$$AgCl_{(s)} + e^- \rightleftharpoons Ag_{(s)} + Cl^-$$

A liquid junction connects the reference electrode with the sample solution. Inevitably, a *junction potential* of up to 30 mV will build up and influence the measurement, due to the varying diffusion rates of the ions involved. It should be noted that for monovalent ions a measurement error of 1 mV already results in a relative error of 4 % for the concentration value. However, the magnitude of the junction potential can be much reduced by adding an ionic strength adaptor to each sample, i.e. a conducting salt consisting of anions and cations with a similar diffusion rate.

The ISE counterpart, also called *working electrode*, probes the sample solution by means of an interface that, ideally, interacts only with the ionic species to be measured. For Ag^+ determination, a solid-state membrane is commonly used that separates an internal electrolyte from the sample solution. This membrane consists of solid Ag_2S which is electrical-

ly conductive due to Ag^+ mobility in the solid phase. Ag_2S has very low solubility in water, according to the following dissociation reaction:

$$Ag_2S \rightleftharpoons 2\,Ag^+ + S^{2-}$$

The dissolved ions are in specific equilibria with the membrane on both sides, causing the build-up of a potential across it. As the membrane itself releases Ag^+ into the sample solution, it will contribute, if little, to the total concentration. This is evident from the non-linear behavior of the electrode for low ionic concentrations (<0.1 mg/l).

Generally, concentration and activity of ionic species are identical in dilute solutions only. Due to the repellent force of ionic charge, increasing quantities of ions will interfere with each other, thus lowering the potential values measured. Electrode calibration with standard solutions of known concentrations, as well as the addition of a conducting salt to equalize the activity coefficient, compensate for such deviations. For our measurements, the electrode was calibrated against a series of $AgNO_3$ solutions with concentrations of 0.01, 0.1, 1, 10 and 100 mg/l. For ionic strength adaption, 2 vol% of aqueous $NaNO_3$ solution (5 mol/l) were added to each sample. Using a silver ion-selective electrode (ISE; WTW Ag/S 800, Weilheim, Germany), dissolved Ag^+ was measured as a function of time. Under these measuring conditions, the Nernst equation allows the calculation of the ion concentration from the cell potential measured:

$$\Delta E = \Delta E^0 - \frac{2.303\,RT}{nF}\log c \qquad \text{(Nernst equation)}$$

with cell potential, ΔE, standard cell potential, ΔE^0, ideal gas constant, R, temperature, T, ionic net charge, n, Faraday constant, F, and ion concentration, c.

The electrode can only interact with the dissolved species present in the immediate vicinity of the electrode surface. Thus, apart from the potential across the electrode, a second potential will build up between near-surface and bulk solution. This phenomenon is termed the *electrical double layer*, as the potential first decreases linearly, then exponentially, with increasing distance from the electrode. Therefore, to accelerate replenishment of the Ag^+ ions at the membrane, constant stirring of the sample solution is necessary.

To conclude, ISE measurements require little preparative effort and results can be obtained within minutes. ISEs are available for a large range of ionic species at comparatively low cost. However, the accuracy is limited and temperature needs to be strictly controlled.

4. Vapor Transport Sintering of Synthetic Powders

4.1. Introduction to Shrinkage-Free Sintering[§§]

Vapor transport sintering (VTS) is a versatile, though rarely used process to produce highly porous ceramics. In the following, the application of VTS as a novel method to produce calcium phosphate scaffolds with fully interconnected porosity is reported for the first time.

Among the various material transport processes that occur simultaneously during sintering, only two, namely vapor transport and surface diffusion, lead to particle coalescence and coarsening without densification (Figure 11). Atomic mobility is enhanced along surfaces, as there are less spatial constraints. Thus, the activation energy is small compared to both lattice and grain boundary diffusion which are the major densifying mechanisms during conventional sintering. Therefore, surface diffusion starts at relatively low temperatures, while industrial sintering of ceramics is commonly performed at homologous temperatures of 0.7-0.8 times the melting point (in Kelvin) to achieve high densification rates. With increasing process temperature, the relative importance of surface diffusion ceases. According to the standard textbooks, surface diffusion denotes the migration of adatoms and vacancies along the particle surface within a layer thought to be less than 1 nm thick.[217,218] However, quite recently, direct observation via transmission electron microscopy (TEM) revealed that surface diffusion proceeds via the collective motion of several atomic layers.[220]

Similar to surface diffusion, vapor transport of solid matter via evaporation and recondensation contributes to shrinkage-free neck and grain growth. The driving force behind vapor transport is the energetically favorable reduction of surface area. This reduction is achieved due to the differential partial pressures over curved surfaces causing a mass flow from grains to necks, as well as from smaller to larger grains. With regard to calcium phosphate ceramics, phase conversion also needs to be taken into account, as will be discussed in section 4.3.3. As the pores coarsen along with the grains, their interconnectivity is fully retained. Usually, the rate of material transport through the gas phase is negligible compared to lattice and grain boundary diffusion, as very few ceramic materials have sufficiently high vapor pressures under atmospheric sintering conditions. Readey and collaborators first proposed the sintering of metal oxides within a reactive atmosphere to facilitate the formation of volatile species and, thus, enhance vapor

[§§] If no other source is referred to in this section, recourse has been made to the handbooks of Kingery et al. (1976)[217], Rahaman (2008),[218] as well as Salmang and Scholze (2007).[219]

transport.[221-224] For this purpose, various halides can be introduced into the sintering system. The aims of this feasibility study were (i) to identify suitable halide agents and (ii) to verify whether or not large enough pore diameters can be generated by VTS.

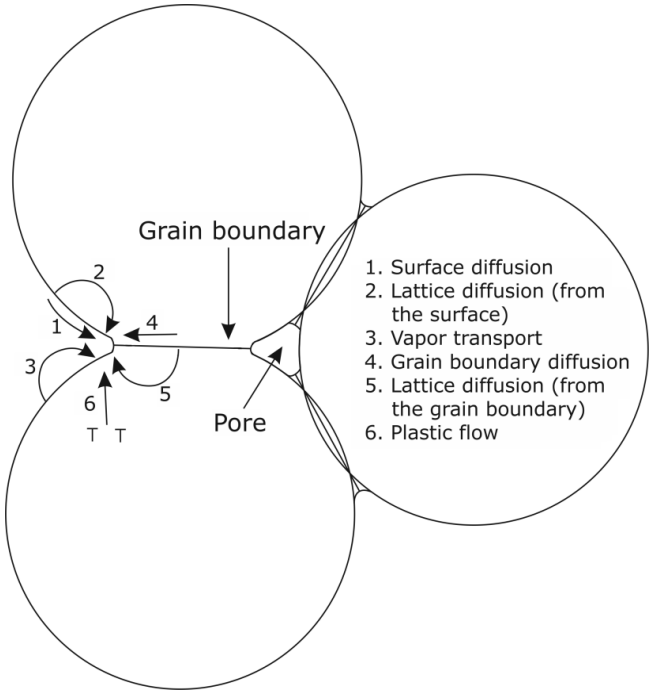

Figure 11: Material transport mechanisms during sintering (after Rahaman 2008).[218]

4.2. Experimental Procedure

4.2.1. Sample Preparation and Sintering

Ceramic samples were prepared from three precursor materials, namely β-tricalcium phosphate (β-TCP), hydroxyapatite (HA) and a 2:3 mixture of both, designated as biphasic calcium phosphate (BCP). Commercially available calcium phosphate powders (Merck, Darmstadt, Germany) were used as starting materials. To confirm the phase purity of the HA reagent, the as-received powder was subjected to XRD analysis before and after 6 h of free sintering at 1100°C, yielding a positive result. The "tri-calcium phosphate" reagent, in fact identified by XRD as a stoichiometric mixture of hydroxyapatite (HA; $Ca_{10}(PO_4)_6(OH)_2$) and monetite ($CaHPO_4$), was calcined at 1100°C for 3 h in air resulting in a full conversion to β-TCP. After calcination, a 50 g batch of the β-TCP powder was subjected to dry zirconia ball milling for 6 h. For the preparation of BCP powders, two processing routes are commonly followed: (i) precipitation of Ca-deficient HA followed by thermal decomposition into HA and β-TCP, or (ii) mechanical blending of single-phase powders;[157,225,226] the latter approach was followed here. Thus, the calcined β-TCP powder was mixed with HA in a 2:3 weight ratio. After the addition of 6 wt% polyethylene glycol

(PEG), a lubricant, all starting powders were homogenized by dry ball milling for 6 h. For each sample, 0.5 g of powder was first pressed manually, then cold-isostatically at 200 MPa. Subsequently, the samples were presintered at 900°C for 1 min to burn out PEG and produce rigid ceramics. The apparent density was determined by measuring the geometrical volume and dry weight of the sample. Relative density, i.e. sample density relative to a non-porous body of the same substance, was then calculated with relation to values provided in the literature, [11] yielding 67% ±1% for HA, 64% ±1% for β-TCP and 56% ±8% for BCP. The diameters of the presintered specimens were approximately 7.2 mm for HA, 7.3 mm for β-TCP and 7.7 mm for BCP with some variation due to the manual pressing step.

One part of the presintered samples was soaked with 0.04 ml of halide acids in their respective saturation concentrations – i.e. aqueous HCl (37 wt%), HBr (47 wt%) and HI (57 wt%) –, as well as in H_2O, and sealed off in evacuated silica ampoules (Figure 12). The amount of acid that can be added is limited by the pressure developing within the ampoule at sintering temperature (ca. 30 bar for 0.04 ml H_2O). The utilization of silica for containment prohibits the use of HF acid for that purpose, as the glass is severely corroded by it. To limit the damage caused by the occasional explosion, the ampoules were put within a refractory container within the furnace.

To another set of samples 0.05 g of solid AgCl, $CaCl_2$ or $MgCl_2$ were added, respectively, before evacuation and sealing in silica ampoules. During sintering, the availability of the solid chloride reagents was limited to their equilibrium partial pressure in the atmosphere, as boiling temperatures were not reached. Vapor transport sintering (VTS) was carried out at 1100°C with holding times from 0.5 to 12 h. In the same furnace runs, untreated samples of the precursor materials were sintered freely to compare densification behavior.

To assess the influence of surface diffusion on pore and grain coarsening, low-temperature sintering experiments were conducted with HA, TCP and BCP samples prepared as described above. Free sintering was carried out at 500°C, 600°C, 700°C and 900°C in air for holding times from 0.5 to 12 h.

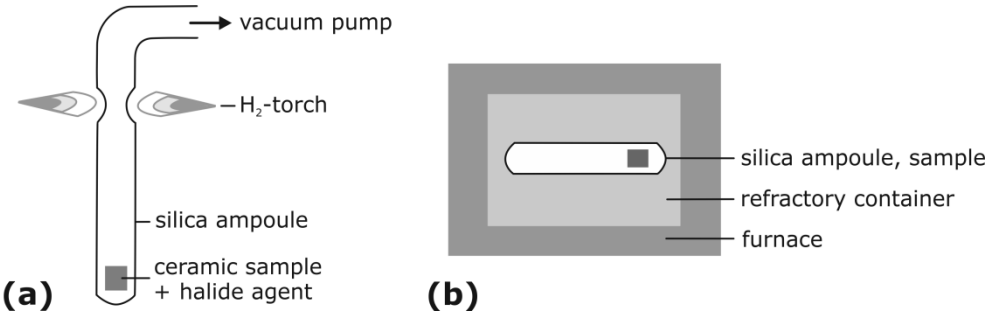

Figure 12: Schematic of the experimental setup: (a) sealing off the sample in a silica ampoule, (b) sample position during vapor transport sintering.

4.2.2. Analytical Methods

Characterization of the microstructure and chemistry was performed at all processing stages by SEM with integrated EDS. For this purpose, ceramic bodies that had been in contact with acid solutions or water were dried at 400°C for 2 h in air after VTS to remove excess humidity. Moreover, the phase composition and molecular structure of selected samples was analyzed by powder XRD and FTIR. To determine the average pore diameters (Feret's diameter) from SEM images of polished samples, the Image J software package (National Institutes of Health, U.S.A.) was used.

4.3. Results and Discussion

4.3.1. Chemical and Phase Analysis

4.3.1.1. XRD

To investigate potential substitutions and phase transformations due to sintering within halide atmospheres, selected HA, β-TCP and BCP samples were submitted to XRD analysis. Vapor transport sintering of pure β-TCP samples in HCl resulted in conversion into Cl-apatite ($Ca_{10}(PO_4)_6Cl_2$; Figure 13a, c). The apatite phase is necessarily Ca-deficient to retain stoichiometry, due to the differing Ca/P ratios of TCP (1.5) and HA (1.67). However, stoichiometric and Ca-deficient apatites could not be distinguished with the routine powder XRD methods applied. However, even after extended holding times of 6 h at 1100°C, some β-TCP remained stable, since the molar amount of added Cl^- was just sufficient for a conversion of about half the β-TCP present, due to experimental constraints (c.f. 4.2.1). Similar observations were made upon HBr sintering, with some of the β-TCP converted into an apatite phase. However, the lack of reference data prevents its identification as Br-apatite (data not shown here). Moreover, upon sintering in HI atmosphere for 6 h, some amount of β-TCP was converted into an apatite phase (Figure 14). As the incorpora-

tion of I^- into the apatite lattice is only possible in trace amounts, no halide apatite can condensate in this system (c.f. 4.3.3 for discussion). Instead, the newly formed phase can be assigned to hydroxyapatite.

For comparison, upon sintering in ambient atmosphere for 6 h, ceramic β-TCP remained fully stable, as atmospheric moisture was not taken up by the ceramic to any measurable extent. Equally, β-TCP powder remained fully stable upon sintering in water vapor for 3 h at 1100°C (Figure 13b). Thus, a conversion of β-TCP into Ca-deficient HA can be excluded in the absence of halides. This is notable, as HA is generally more stable than Cl-apatite, both in physiological settings and at elevated temperatures.[11,227,228] However, only in conjunction with a halide can Ca^{2+} be mobilized in relevant amounts to facilitate substantial material transport through the vapor phase (c.f. chapter 6).

Regarding the BCP samples, β-TCP was still detected together with an apatite phase after sintering in HCl for 6 h, although Cl^- was available in sufficient amounts for a full conversion. Obviously, during the sintering process some β-TCP particles were encapsulated by the newly formed apatite, thus preventing their volatilization. Therefore, both starting materials – β-TCP and BCP – show potential for the fabrication of biphasic calcium phosphate scaffolds with an adjustable phase ratio.

To study phase conversions due to sintering with solid chloride agents, the focus was put on β-TCP samples, because of their single-phase starting composition. The addition of AgCl caused a partial conversion of β-TCP into Cl-apatite upon 2 h of sintering (Figure 15a). AgCl reagent was probably still present in the sample, but major diffraction peaks at 27.8° and 32.2° (2θ) overlap with those of the calcium phosphates present, thus prohibiting identification. By contrast, the presence of $CaCl_2$ and $MgCl_2$ resulted in an almost complete conversion into Cl-apatite (Figure 15b, c). Regarding $CaCl_2$, this is not surprising, as apatite is generally more stable than β-TCP and surplus ions of Ca^{2+} and Cl^- are available to balance stoichiometry. Accordingly, the diffractogram of the $CaCl_2$-sintered sample shows a good match with the Cl-apatite structure (Figure 15b; PDF 00-027-0074). However, a minor fraction of additional phase(s) was present which could not be identified. Equally, the diffraction pattern of the $MgCl_2$-sintered sample is in good agreement with Cl-apatite (Figure 15c). Moreover, EDS analyses confirmed the presence of both Cl and Mg in the bulk material. It has been reported that Ca^{2+} can be substituted by Mg^{2+} in the apatite lattice at least to some extent (c.f. 5.3.1.2 for discussion).[11,80] Alternatively, in systems where additional Ca^{2+} or Mg^{2+} is lacking, it seems plausible that Ca^{2+} vacancies are formed. This would be the case for Cl-apatite condensated during AgCl-sintering. The

observation that only a partial conversion of β-TCP into apatite occurred in AgCl atmosphere can be explained by the limited availability of Cl^- in the system.

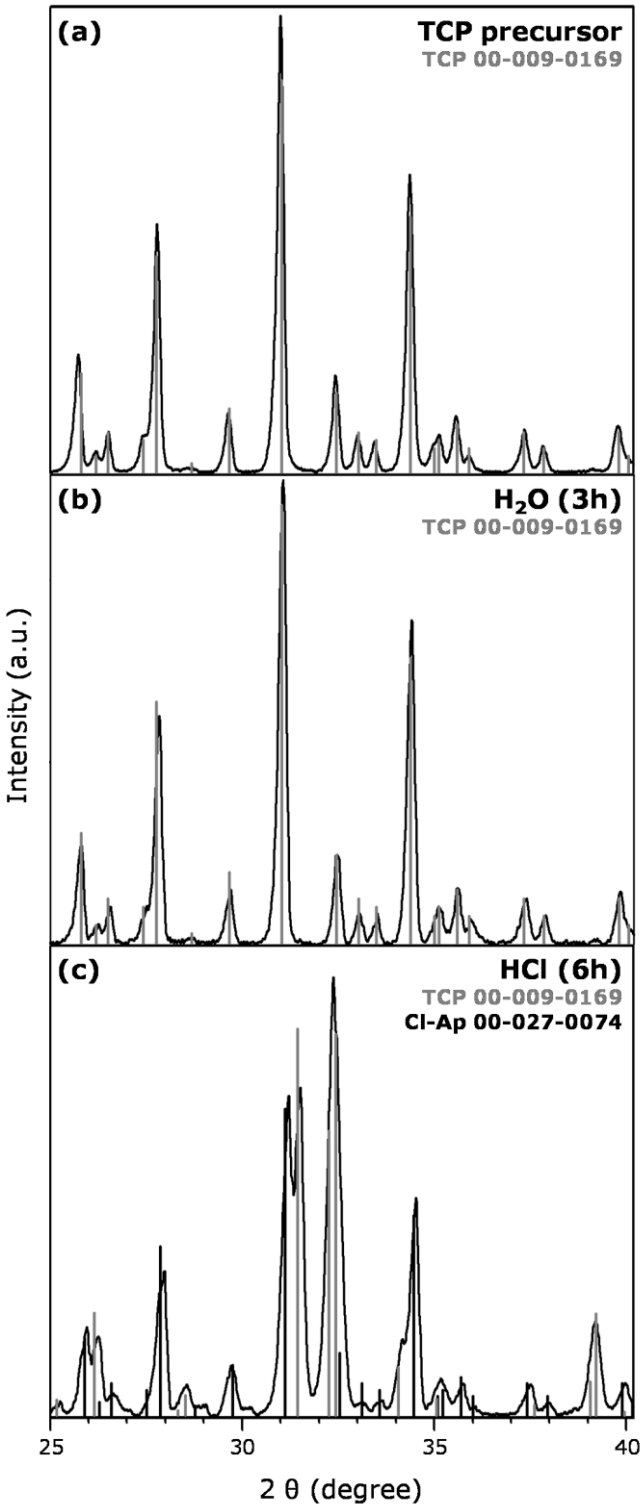

Figure 13: X-ray diffractograms of (a) β-TCP precursor powder; (b) β-TCP powder sintered at 1100°C for 3 h in water vapor; (c) β-TCP ceramic sintered at 1100°C for 6 h in HCl atmosphere. Apatite formation exclusively takes place in the presence of a halide reagent.

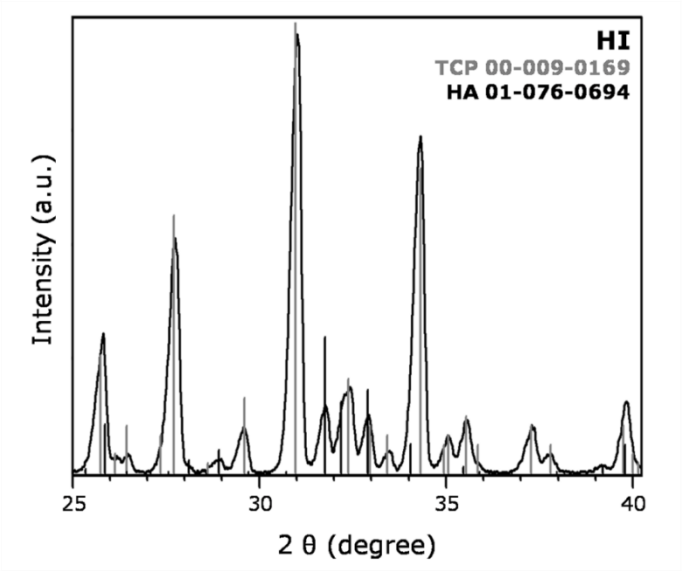

Figure 14: Diffractogram of a β-TCP ceramic after sintering at 1100°C for 6 h in HI atmosphere. While some amount of HA is formed, I^- is not incorporated into the apatite lattice to a measurable extent.

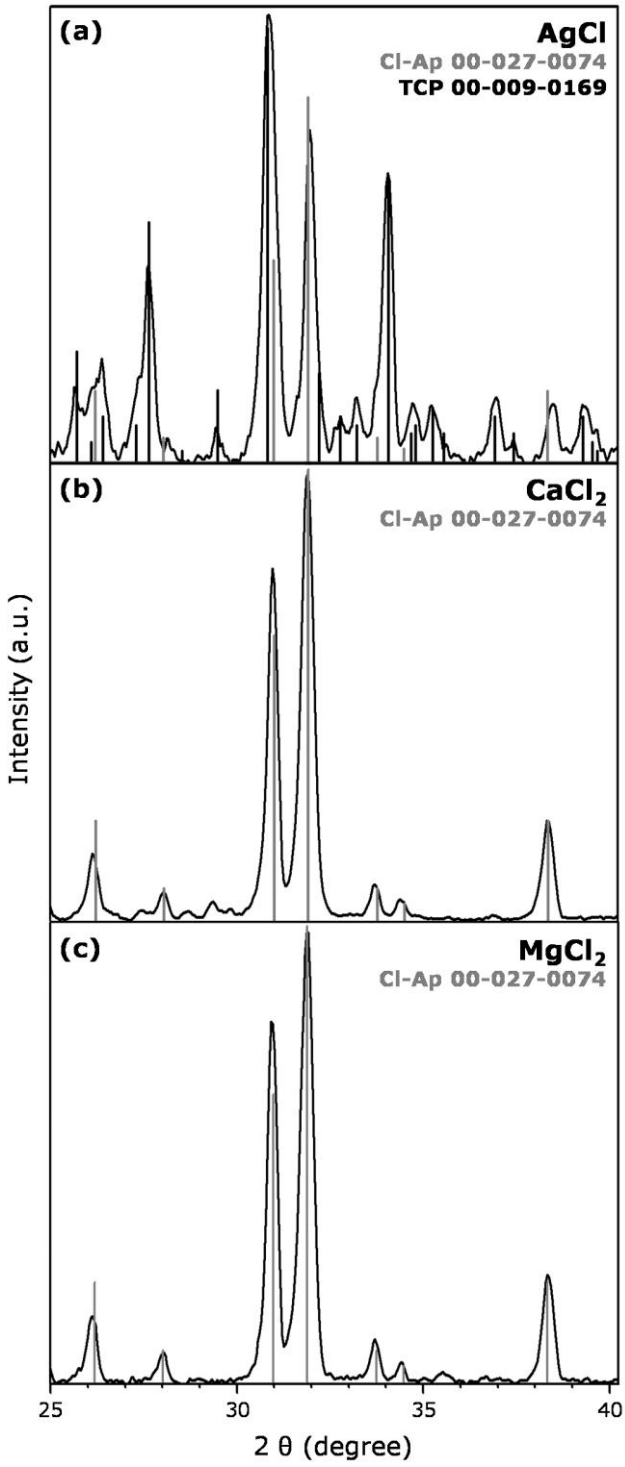

Figure 15: Diffractograms of β-TCP ceramics after sintering at 1100°C for 2 h in (a) AgCl, (b) $CaCl_2$ and (c) $MgCl_2$ atmosphere. Due to limited availability of Cl^- in (a), only a partial conversion to Cl-apatite occurs, whereas samples in (b) and (c) undergo nearly full conversion.

XRD analyses were also carried out HA ceramics sintered in air and HCl for 6 h, respectively (Figure 16). Both diffractograms are in good agreement with monoclinic apatite structures, as is common for synthetic apatites of very high purity.[229] The XRD pattern for

HA sintered in air corresponds to diffraction files of pure HA (PDF 01-076-0694), whereas HCl-sintered HA can be identified as Cl-bearing hydroxyapatite (PDF 01-070-0794). When comparing the two diffractograms measured, a considerable shift of the HA (-2 2 2) peak towards higher 2θ values can be observed upon sintering in HCl. This corresponds to a partial replacement of the OH^- groups by Cl^-, resulting in an apatite solid solution.[79] This substitutional reaction is independent of the phase conversion from β-TCP to Cl-apatite described above.[228,230] The structural change causing an additional peak at 29.6° (2 θ) could not be identified (Figure 16b).

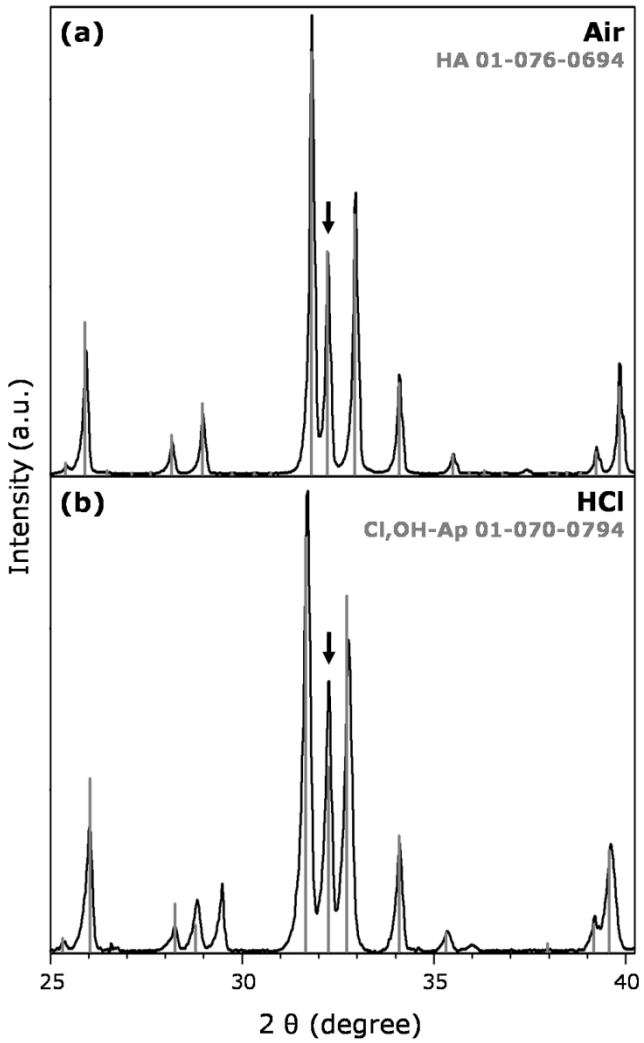

Figure 16: Diffractograms of HA ceramics after sintering at 1100°C for 6 h in (a) air and (b) HCl atmosphere. Shifting of the HA (-2 2 2) peak towards higher 2 θ values indicates the substitution of OH^- by Cl^- (marked by arrow).

With regard to the proposed application of vapor transport sintering for the fabrication of bone graft materials, issues of contamination by halide agents need to be addressed. Although no phase diagrams are presently available for the given experimental conditions,

namely for vapor pressures of up to 30 bar within the silica containers caused by the addition of halide acids at sintering temperature, it can be derived from the literature that various calcium phosphate phases may be stable thermodynamically, depending both on the Ca/P ratio of the precursors[74,231] and on the presence of impurities.[232,233] Due to the "flexible" crystal structure of apatite, a large number of substitutions may occur.[11,80] As can be derived from the sintering of pure HA in HCl for 6 h, the substitution of OH^- by Cl^- is a reaction favored under the specific sintering conditions. XRD, FTIR and EDS analyses confirmed that during sintering halogen ions (Cl^-, Br^-) enter the apatite lattice substituting for OH^- ions. In the case of the Cl^- ions this seems less of a concern, as they are a common impurity in human bone, dentine and enamel.[234] In contrast, there are no natural occurrences of apatites containing more than trace amounts of Br^-, although substitution is possible to some extent.[80,235] Br^- is highly toxic and, thus, its use cannot be recommended for other than academic purposes.

4.3.1.2. FTIR

To obtain a better understanding of the substitutional reactions detected with XRD, selected samples were subjected to FTIR analysis. Analysis of pure HA ceramic sintered freely for 6 h showed a strong vibrational mode at 3572 cm^{-1} that is caused by the hydroxyapatite OH^- stretching vibration (Figure 17).[11] In contrast, the spectrum obtained for a HA sample sintered in HCl for 6 h shows a distinct "splitting" into a set of peaks at 3495-3570 cm^{-1}. Similar sets of peaks were observed for HA-containing BCP and β-TCP after sintering in various reactive atmospheres (Figures 18 and 19).

Dykes and Elliott were first to report an "additional" OH stretching mode at 3498 cm^{-1} caused by c-axis substitution of limited amounts of Cl^- for OH^-.[236] Best agreement of our results, however, was found with the study of Maiti and Freund on the incorporation of high amounts (10-96 %) of Cl^- into HA.[228] The authors concluded that the appearance of several additional bands was caused by the formation of O-H ⋯ Cl hydrogen bonds. An analogous mechanism is here proposed for the HBr-sintered samples (Figures 18c and 19c). Furthermore, the authors suggested that the incorporation of a small amount of OH^- was energetically favorable, as compared to pure Cl-apatite. This helps to explain why some OH^- is incorporated into the newly formed (i.e. β-TCP derived) apatite phase, as indicated by the corresponding vibrational bands (Figure 19). The uptake of OH^- during sintering in the nominally water free and non-hygroscopic AgCl was probably caused by water vapor remaining in the ampoule after evacuation with a water jet pump. Thus, the

phases resulting from the β-TCP conversion can be characterized as halide apatites with a small fraction of OH^- substituting for Cl^- or Br^- in the anion column along the c-axis.

Summing up, as further supported by XRD and EDS data, the observed peak splitting corresponds to two distinct processes: (i) c-axis substitution of OH^- groups by halogen ions in the apatite lattice, and (ii) phase conversion of β-TCP into Cl-apatite with some degree of OH^- incorporation.

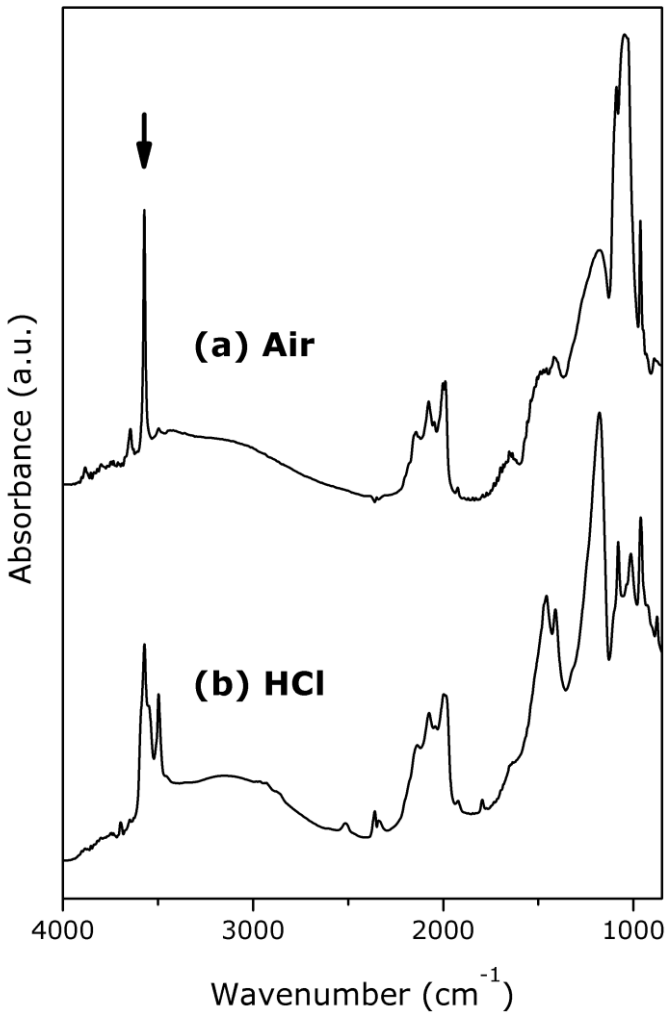

Figure 17: FTIR spectra of HA ceramics after sintering at 1100°C for 6 h in (a) air and (b) HCl atmosphere. The stretching band of the OH-group at 3570 cm^{-1} (marked by arrow) degenerates into a set of peaks due to the c-axis substitution of OH^- by Cl^-.

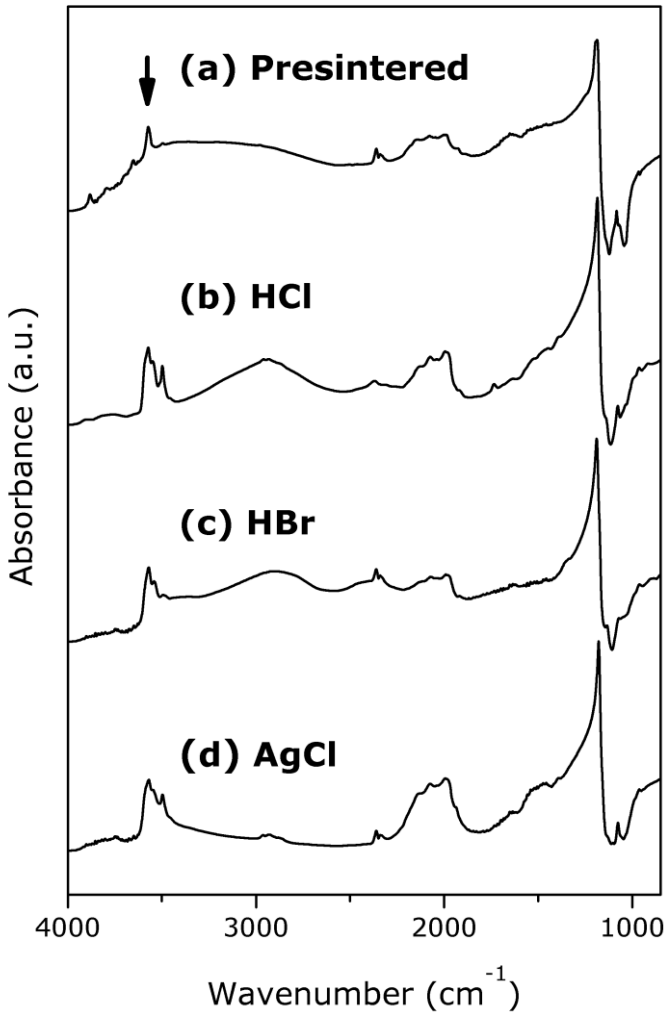

Figure 18: FTIR spectra of BCP ceramics after sintering at 1100°C (a) presintered for 1 min in air; sintered for 6 h in (b) HCl, (c) HBr and (d) AgCl atmosphere. Halide apatite formation in (b-d) is indicated by the degeneration of the OH group's stretching band (marked by arrow) into a set of peaks at 3495-3570 cm^{-1} as well as an overall increase of intensity.

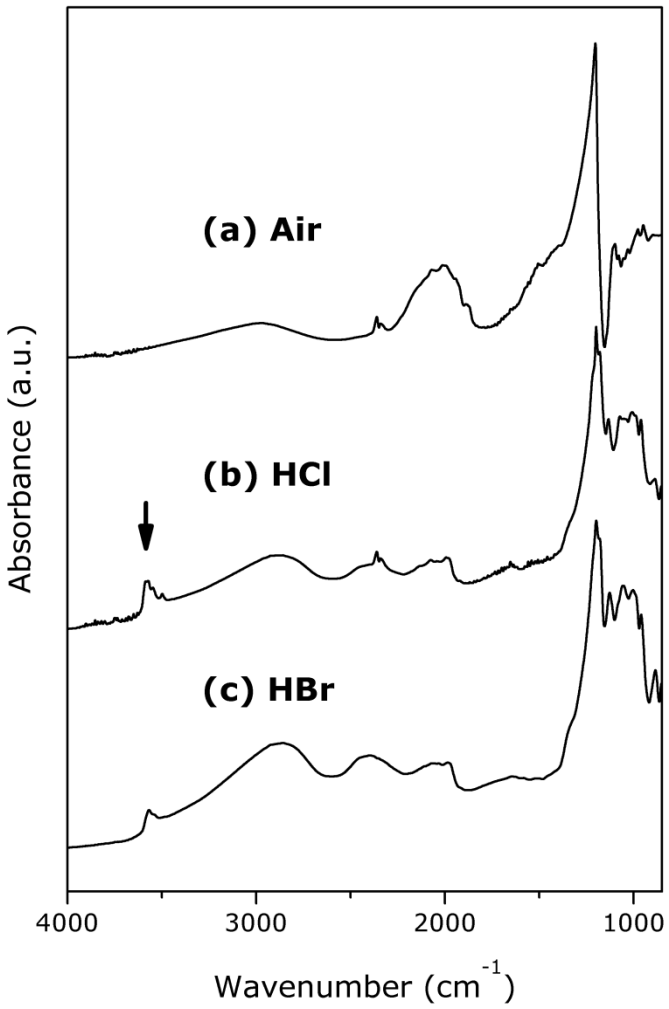

Figure 19: FTIR spectra of β-TCP ceramics after sintering at 1100°C for 6 h in (a) air, (b) HCl and (c) HBr. Apatite formation is indicated by peaks in the range of 3495-3570 cm^{-1} (marked by arrow).

4.3.2. Microstructure Development

4.3.2.1. Vapor Transport Sintering with Various Halide Agents

For many of the systems tested, creating a reactive halide atmosphere proved successful regarding the stimulation of simultaneous pore and grain coarsening (Figures 20-22). Vapor transport was considerably enhanced for both β-TCP and BCP in the presence of various reagents, with the sole exception of HI acid (c.f. 4.3.2.2). Sintering in HCl atmosphere for 6 h at 1100°C produced average pore diameters of 4.3 ±2.8 µm for BCP ceramics, and 6.1 ±4.8 µm for β-TCP (Figures 20d and 22a). By extending the holding time further to 12 h, the average pore diameter of the resulting BCP ceramic eventually shrank to 2.0 ±1.8 µm, indicating a stagnation of the vapor transport process. For comparison, sintering under otherwise identical conditions in ambient atmosphere yielded pore diameters of 1.1 ±0.51 µm and 0.91 ±0.40 µm for BCP, after 6 h and 12 h, respectively, and 4.3 ±3.5 µm

for β-TCP after 6 h. Densification of the BCP samples was determined geometrically via the increase in relative density which amounted to 6.6 % after 6 h of sintering in HCl atmosphere. This is a significant reduction compared to free sintering in air which resulted in up to 37 % densification under the given experimental conditions (Figure 23). Comparing BCP and β-TCP samples, the former showed much higher sinterability in terms of densification. Shrinkage of β-TCP after 6 h amounted to less than 1 % in HCl atmosphere, and only to about 2 % in air. This observation – together with the relatively large pore size obtained for β-TCP upon free sintering – confirms its generally poor densification behavior that has already been noted by other authors.[91,231] In the current experimental setup, the maximum pore size obtainable by VTS is on the order of 5 µm for both BCP and β-TCP, due to a stagnation of the coarsening process for holding times beyond 6 h (Figure 23). Thus, the pore geometry obtained under the given conditions is still far off the size required for the intended application as a bone graft material (i.e. 100-500 µm).

Regarding pure HA ceramics, however, our results were rather inconclusive (Figure 24). Apparently, vapor pressures of the relevant compounds had not been raised to a level permitting substantial vapor transport. For sintering in HCl acid, no pore coarsening was evident, whereas grain growth was comparable to that observed upon sintering in air. However, exaggerated grain growth – also known as *secondary recrystallization* – and faceting occurred upon sintering with all other halide reagents tested, and most strongly so in the presence of water vapor (Figure 24d). Exaggerated grain growth leads to inclusion of pores within oversized grains,[217] with deleterious effects on both mechanical stability and osteoconduction (c.f. chapter 2).

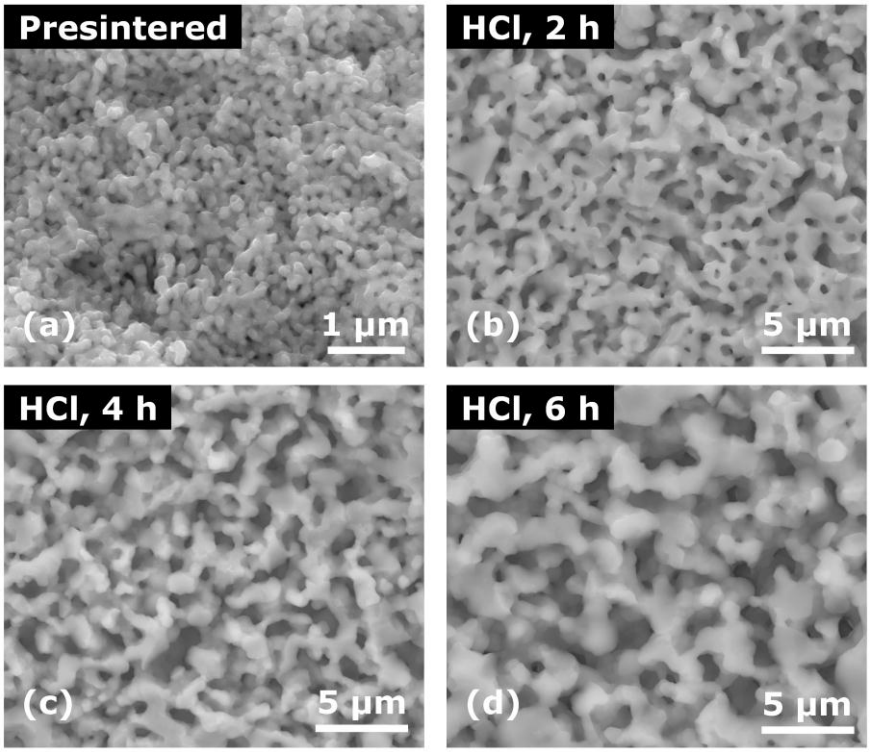

Figure 20: SEM images of BCP ceramics: (a) after presintering at 900°C for 1 min in air, (b) after sintering at 1100°C in HCl for 2 h, (c) 4 h and (d) 6 h. Vapor transport sintering in HCl atmosphere leads to simultaneous pore and grain coarsening over time. Please note the change of scale between (a) and (b-d).

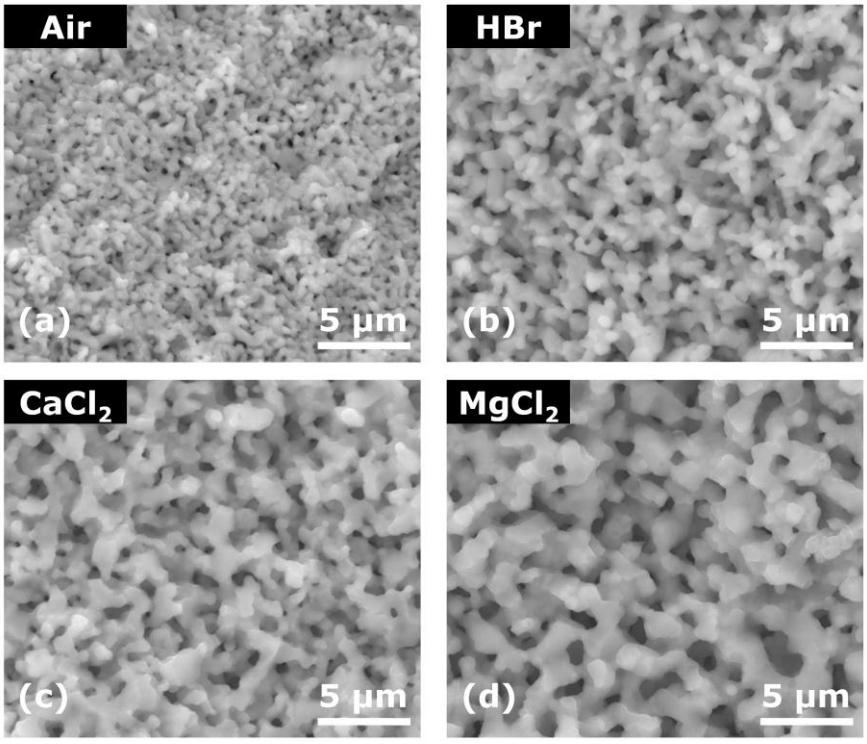

Figure 21: SEM images of BCP ceramics: (a) after sintering at 1100°C for 2 h in air, (b) HBr, (c) $CaCl_2$ and (d) $MgCl_2$ atmosphere. Simultaneous pore and grain coarsening occurs during vapor transport sintering in various halide atmospheres.

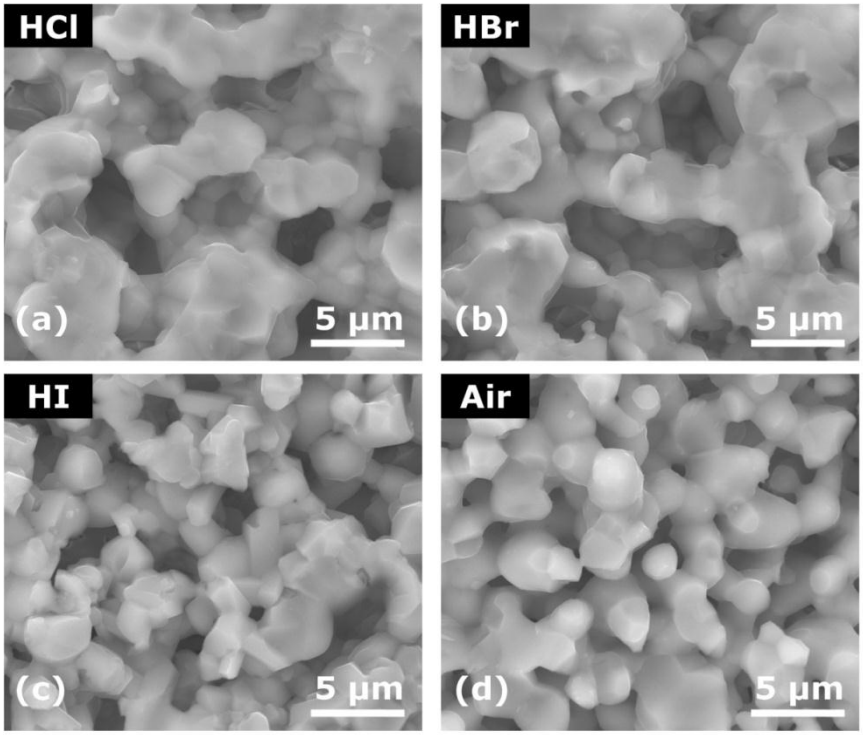

Figure 22: SEM images of β-TCP ceramics after sintering at 1100°C for 6 h in (a) HCl, (b) HBr, (c) HI and (d) air. Simultaneous pore and grain coarsening occurs in various halide atmospheres, with the exception of HI.

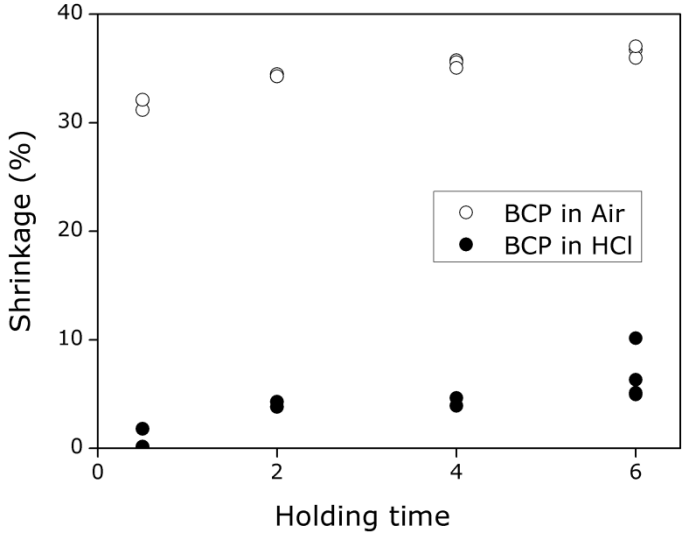

Figure 23: Shrinkage of BCP ceramics upon sintering in air and in HCl atmosphere at 1100°C for various holding times.

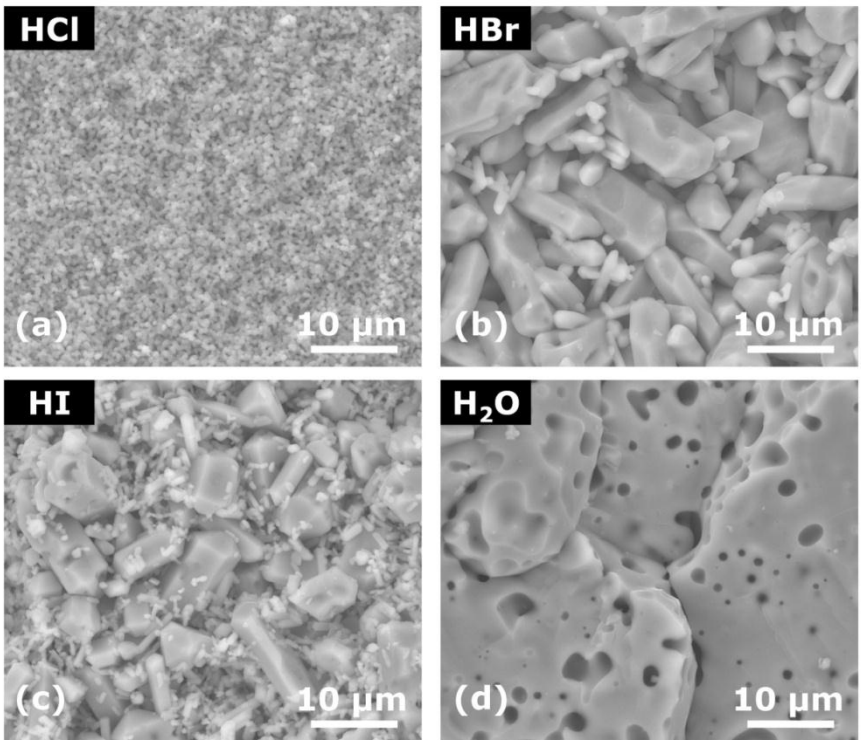

Figure 24: SEM images of HA ceramics sintered for 2 h in (a) HCl, (b) HBr, (c) HI and (d) H_2O. Whereas no simultaneous pore and grain coarsening is evident in the presence of HCl, sintering in various other atmospheres induces exaggerated grain growth and faceting.

4.3.2.2. Vapor Transport Sintering in HI Atmosphere

For sintering experiments with hydroiodic acid (57 %), the microstructure development differed from the other sample-halide reagent systems. Sintering experiments were carried out for HA, BCP and β-TCP ceramics for 0.5-12 h holding time. Although our thermodynamic calculations point to relatively high amounts of all relevant volatile species in the sintering atmosphere, material transport is evidently not enhanced (c.f. Appendix, Figure 52b). Instead, in the presence of HI acid, both microstructural coarsening and densification were impeded during BCP and β-TCP sintering, as compared to sintering in the presence of other halide reagents or free sintering in air (Figures 22c and 25). Apart from that, sintering of HA was affected by exaggerated grain growth destroying the cohesion of the ceramic fabric (Figure 24c). These observations support our view that vapor transport of calcium phosphates is not simply driven by evaporation and re-condensation, but by the phase conversion of β-TCP into apatite. In fact, phase conversion is impeded in HI-containing sintering systems, as further discussed in section 4.3.3.

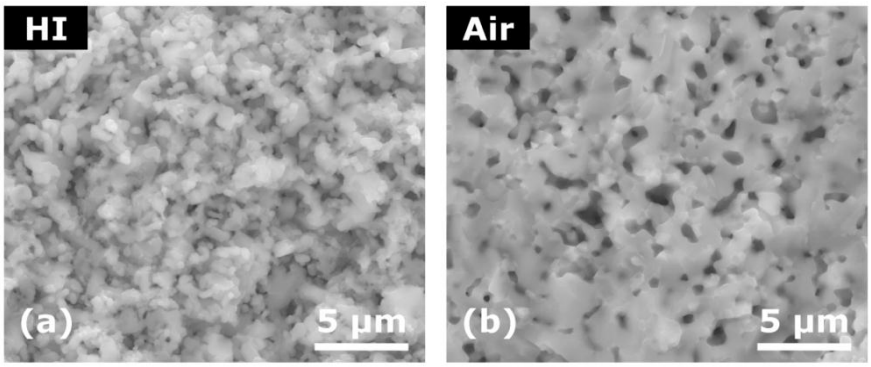

Figure 25: SEM images of BCP ceramics sintered at 1100°C for 6 h (a) in HI atmosphere and (b) in air. Both densification and grain growth are retarded in the presence of HI, as compared to free sintering in air.

4.3.2.3. Vapor Transport Sintering in AgCl atmosphere

Most remarkable is the effect of AgCl as a sintering additive which not only facilitates VTS, but at the same time condenses as finely dispersed Ag-containing particles across the sample's interior (Figure 26). AgCl is the only sintering agent used in this study to show such behavior. In this section, results of our experiments with β-TCP and BCP samples will be presented. Concerning HA ceramics, deviating effects were observed which are discussed in chapter 5.3.

Sintering agent-derived Cl^- is structurally incorporated into newly formed apatite, as confirmed by chemical and phase analysis (c.f. 4.3.1.1 and 4.3.1.2). Thus, the AgCl compound condenses as finely dispersed $AgCl_{1-x}$ and, eventually, as Ag particles in pores and on the outer surface (Figure 26). After extended holding for 12 h, it is for the most part reduced to metallic silver, as confirmed by EDS. The Ag-containing particles grow unrestrictedly at the sample's rims to sizes of several 10 µm (Figure 27), whereas their growth within the scaffold's interior is confined by the pore diameter (Figure 26b). The deposition of small Ag-bearing particles seemed promising with regard to the well-known antibacterial properties of the metal (c.f. 2.3.5). As the Ag particles are only partially wetting the ceramic surface with a contact angle near 90° (Figure 27), the bioactive properties of the calcium phosphate scaffold should not be compromised. An assessment of Ag^+ ion release into solution, as well as antibacterial tests for macroporous ceramics suitable for bone graft applications are presented in chapter 5.

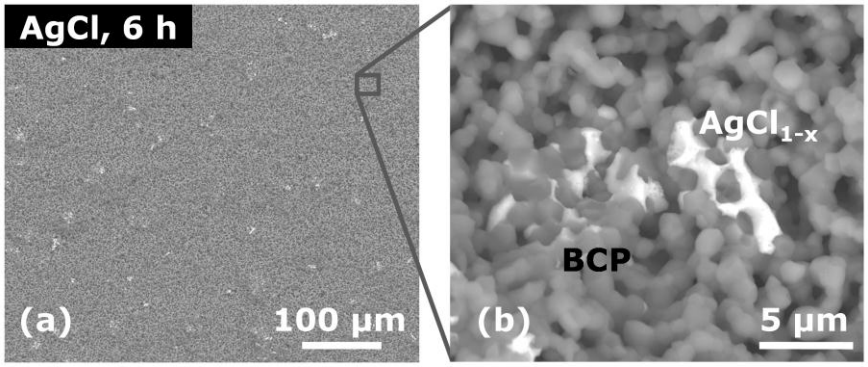

Figure 26: SEM images of a BCP ceramic sintered at 1100°C for 6 h in AgCl atmosphere (a, b). AgCl-sintering combines enhanced vapor transport with $AgCl_{1-x}$ condensation (white; Z-contrast) across the sample's interior.

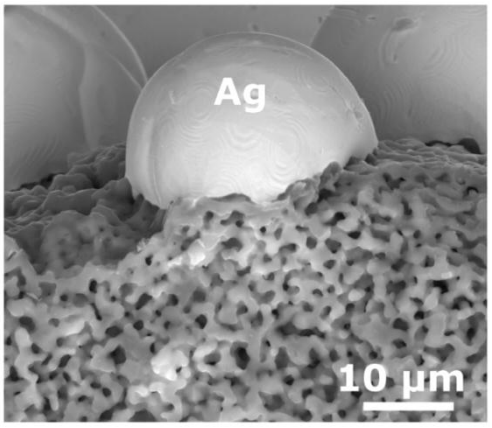

Figure 27: SEM image of a BCP ceramic after sintering for 12 h at 1100°C in AgCl atmosphere showing partial wetting of the outer surface by Ag particles. Metallic silver condenses as Cl^- is incorporated into the apatite lattice.[237]

4.3.3. Material Transport during Vapor Phase Sintering

Although VTS in halide atmospheres was proposed almost 30 years ago, the exact mechanism of material transport had not been fully understood, as yet. Readey and collaborators assumed Ostwald ripening to account for particle coarsening during VTS, but had to acknowledge deviations from this model with regard to the resulting particle size distribution and activation energies.[221,238] As a standard model for coarsening processes, Ostwald ripening describes the growth of large particles (or pores) at the expense of smaller ones (Figure 28).[239,240] The process can be either controlled by interface reactions or by the diffusion rate in the surrounding medium.[222] Alternatively, the Greskovich-Lay model describes coarsening of highly porous ceramics as a process of neck filling followed by grain boundary "sweep" through the smaller of two adjacent grains (Figure 29).[241] Thus, grain growth depends on the relative size of the immediate neighbor, but not on a critical parti-

cle size. Although Greskovich and Lay assumed surface diffusion to play a dominant role in neck growth, the same microstructural development may equally be caused by enhanced vapor transport. In both models, the driving force for coarsening is the reduction of interfacial free energy that can be achieved via surface reduction.[218] Our investigations with EDS elemental mappings confirm that Ostwald ripening is the appropriate model to describe the coarsening process of calcium phosphate ceramics via VTS.

According to the reaction equations provided by Readey and collaborators, material transport via the vapor phase is a process of evaporation and re-condensation of the same phase, as observed for all materials studied by their group (i.e. Fe_2O_3, Si, TiO_2, ZnO and ZrO_2).[221,222] However, we found that in the case of calcium phosphate ceramics, VTS is driven by the phase conversion of β-TCP into the more stable apatite phase. During sintering within the reactive atmosphere, volatile species are preferentially formed from small β-TCP grains, due to their comparatively high surface energy (c.f. 6.1). Continuous apatite condensation in turn consumes the volatile species, while filling up necks and covering surfaces of the precursor grains. To retain equilibrium partial pressures, more β-TCP evaporates, thus perpetuating the mass flow. Direct evidence of this process was obtained by EDS elemental mappings: in Figure 30 the distribution of Cl within a β-TCP ceramic sintered in HCl at 1100°C for 2 h is shown. Under the given experimental conditions, VTS was carried out successfully. The presence of Cl indicates the condensation of Cl-apatite from volatile species, as determined by XRD analyses (c.f. 4.3.1.1). Thus, Cl mapping reveals the accretion of Cl-apatite on β-TCP grains which results in particle coarsening. During sintering, the rate of material transport can be assumed to be constant, at most, or declining. Therefore, major causes for the observed stagnation of microstructural coarsening after several hours of sintering are (i) dependency of material volume that needs to be transported to achieve further coarsening on cubed particle radius (Ostwald ripening) and (ii) either consumption of β-TCP or the halide reagent, depending on the experimental setup.

In contrast, problems encountered during HA sintering suggest that this phase is too stable for mobilization via the formation of volatile species. As shown in Figure 31, upon sintering in HCl at 1100°C for 2 h, Cl is homogeneously distributed within the HA ceramic. Under these conditions, no simultaneous coarsening of pores and grains was achieved. As further supported by XRD and FTIR analyses, Cl^- becomes incorporated into the apatite lattice upon sintering, but only to a limited extent that serves to increase its stability (c.f. 4.3.1.2).

By recognizing the phase transformation of β-TCP into Cl-apatite as the driving force behind successful VTS, the ineffectiveness of HI as a sintering agent can be explained. In natural apatites, I^- occurs in trace amounts only. Generally, its compatibility with F^-, OH^- or Cl^- in the anion column along the c-axis has been questioned, due to the large ionic radius of I^-.[11,80] Synthesis is possible to some extent,[242-244] but not for calcium phosphate apatites, i.e. apatites *sensu stricto*. As thermodynamical calculations suggest that Ca is mobilized in the form of CaI_2 (c.f. 6.3.3), it seems plausible that conversion of β-TCP into an apatite phase is not favored in this sintering system. Indeed, only a small amount of β-TCP is transformed into halide-free HA, as determined by XRD for β-TCP ceramics (c.f. 4.3.1.1, Figure 14). Therefore, the influence of vapor transport remains negligible during sintering of β-TCP or BCP in HI atmosphere (c.f. 4.3.2.2).

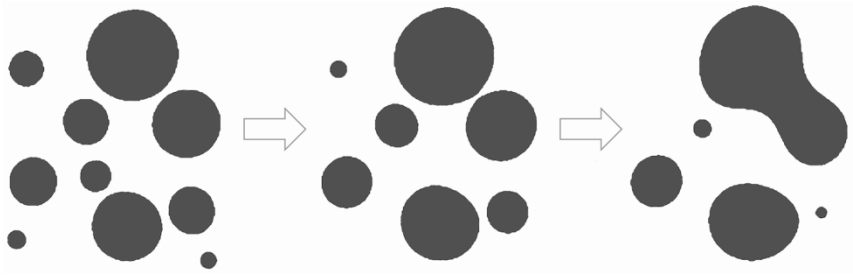

Figure 28: Schematic of the Ostwald ripening process. The model is applicable to coarsening phenomena of both particles and pores (after Ode et al. 2000).[245]

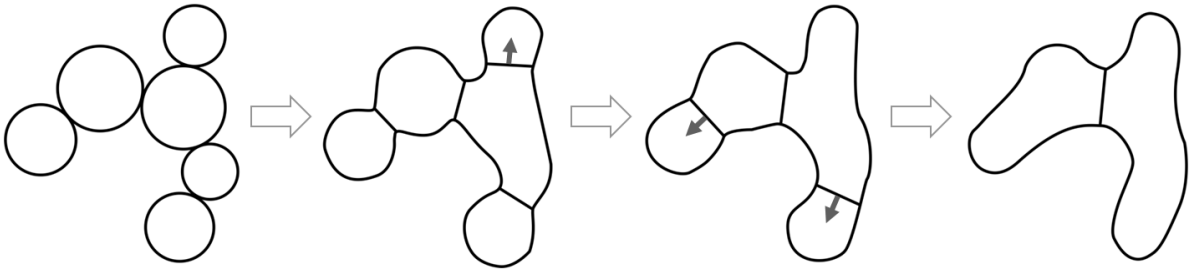

Figure 29: Schematic of the Greskovich-Lay model for shrinkage-free grain growth due to grain boundary movement (after Greskovich and Lay 1972).[241]

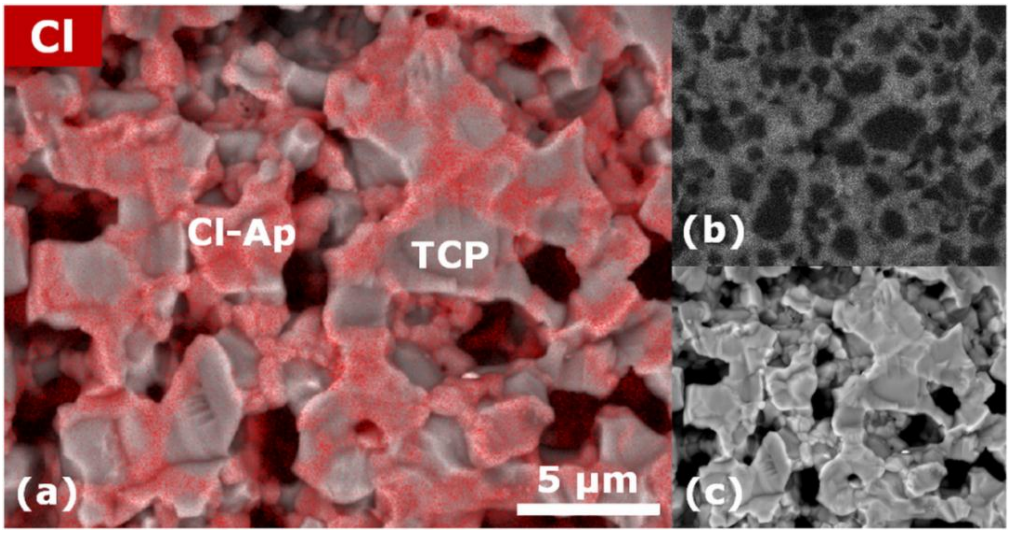

Figure 30: EDS mapping showing the heterogeneous Cl distribution in a β-TCP ceramic sintered in HCl atmosphere at 1100°C for 2 h: (a) SE image overlain by EDS signal indicating the presence of Cl, (b) EDS signal and (c) SE image. Cl-apatite accretion on β-TCP grains results in particle coarsening.

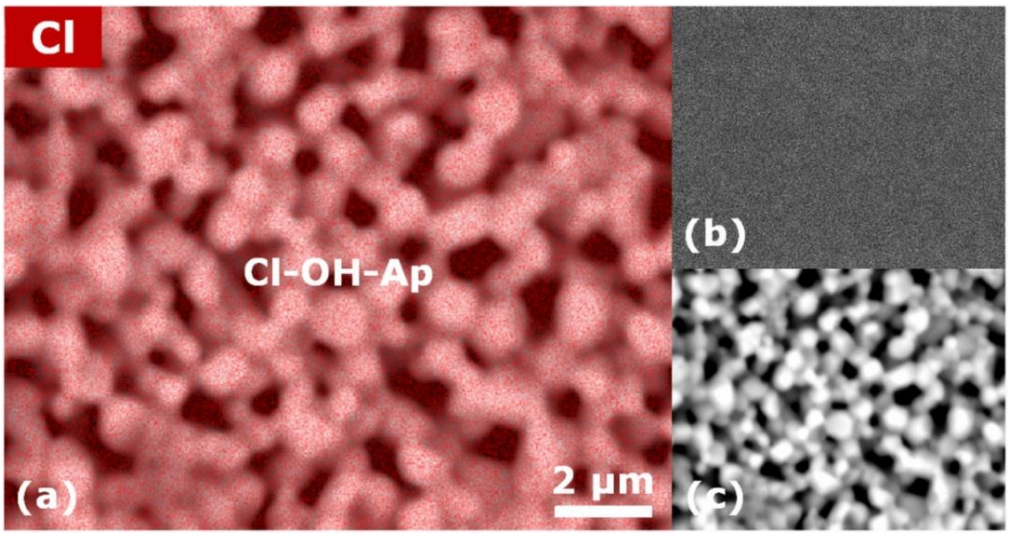

Figure 31: EDS mapping showing the homogeneous Cl distribution in a HA ceramic sintered in HCl atmosphere at 1100°C for 2 h: (a) SE image overlain by EDS signal indicating the presence of Cl, (b) EDS signal and (c) SE image. Pore and grain coarsening are impeded, while Cl^- is incorporated into the apatite lattice (no phase conversion involved).

4.3.4. Surface Diffusion

To investigate the influence of surface diffusion as an alternative process to stimulate shrinkage-free pore and grain coarsening, low-temperature sintering experiments were conducted with β-TCP, BCP and HA samples prepared as described in chapter 4.2. Free sintering was carried out at 500°C, 600°C and 700°C in air for holding times of 0.5 to 12 h using at least three samples per condition.

Shrinkage was virtually nonexistent for samples sintered at 500°C and markedly reduced for holding temperatures of 600°C and 700°C, as compared to conventional sintering at 1100°C; data are shown exemplarily for HA in Figure 33. The results are in good agreement with the observation of Raynaud et al. that densification of compacted calcium phosphate powders starts above 700°C, as indicated by the decrease of total surface area.[91] Microstructure characterization via SEM imaging showed that no substantial neck or grain growth was observable after up to 12 h of sintering at 700°C for HA, β-TCP and BCP (Figure 32). Thus, surface diffusion poses no alternative to vapor transport sintering for shrinkage-free microstructural coarsening at temperatures low enough to prevent densification caused by other transport mechanisms (c.f. 4.1, Figure 11).

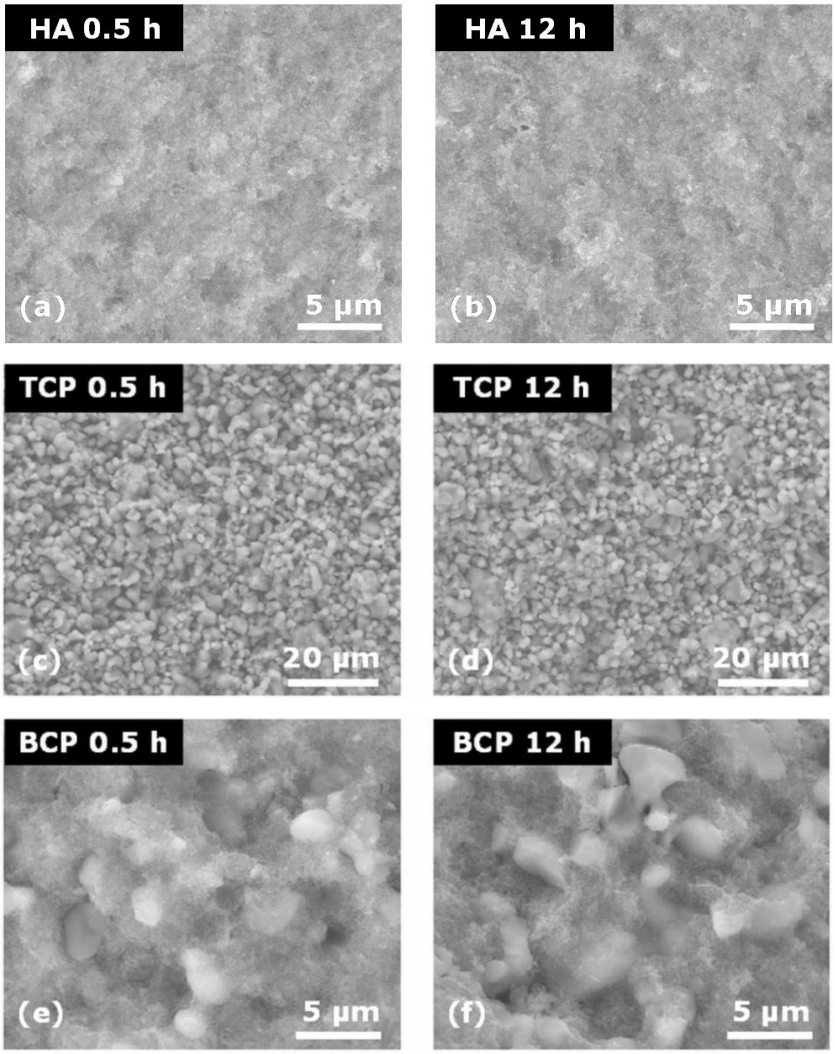

Figure 32: SEM images of calcium phosphate ceramics sintered at 700°C in air for various holding times: HA after (a) 0.5 h and (b) 12 h; β-TCP after (c) 0.5 h and (d) 12 h; BCP after (e) 0.5 h and (f) 12 h. The starting grain size of β-TCP is comparatively large due to the calcination step (c.f. 4.2.1). Therefore, BCP specimens show a bimodal grain size distribution. At this low holding temperature, no pore and grain coarsening can be observed.

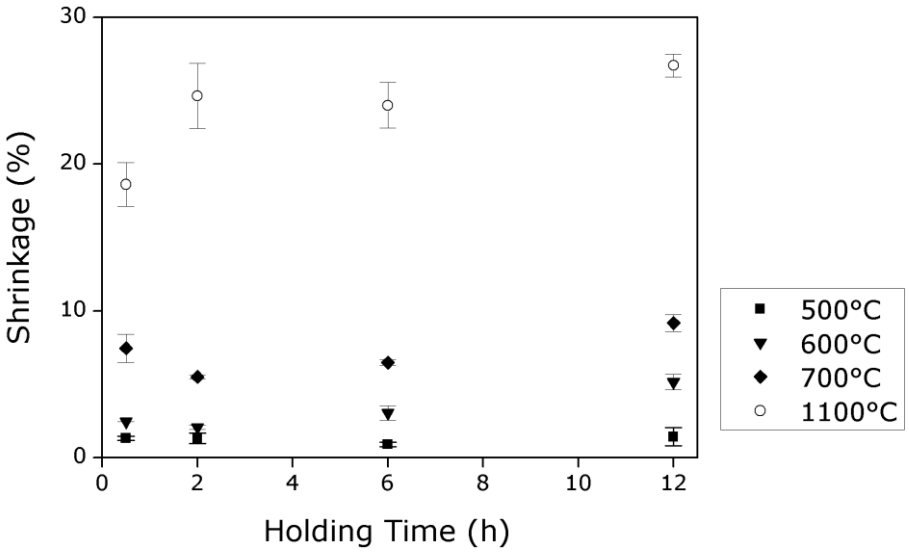

Figure 33: Shrinkage of HA ceramics upon free sintering at various temperatures and holding times. Error bars indicate the standard deviation.

4.4. Chapter Conclusion

For the first time, vapor transport sintering (VTS) in halide atmospheres was successfully applied for the fabrication of porous calcium phosphate scaffolds. During sintering, the presence of a reactive halide atmosphere enhanced evaporation and re-condensation of calcium phosphates. This promoted the simultaneous coarsening of pores and grains for both β-TCP and BCP ceramics in combination with nearly all tested additives, i.e. halide acids (HCl, HBr), as well as the easy-to-handle solid chlorides ($CaCl_2$, $MgCl_2$ and AgCl). Sintering of HA samples did not yield the expected results, however, as no significant pore coarsening could be observed. Instead, exaggerated and faceted grain growth commonly occurred.

As can be inferred from the results obtained by complementary analytical methods (i.e. XRD, FTIR and EDS), two distinct reactions are characteristic for sintering of calcium phosphates in halide atmospheres: (i) c-axis substitution of OH^- groups by halogen anions in the apatite lattice, and (ii) phase conversion of β-TCP into Cl- or Br-apatite – depending on the halide agent used –, with some degree of OH^- incorporation. Due to differing Ca/P ratios, Ca^{2+} vacancies are formed during the phase conversion of β-TCP into apatite to retain stoichiometry. However, additional cations can be introduced by appropriate halide agents, such as $CaCl_2$ and $MgCl_2$, for compensation. As the phase conversion can further be influenced by limiting the Cl^- or Br^- availability, β-TCP and BCP are both suitable starting materials for the fabrication of porous ceramics with adjustable phase composition. As

the only sintering agent among the ones tested, HI turned out to be ineffective, because the large ionic radius of I^- impairs the phase transformation of β-TCP into a halide apatite.

The Ostwald ripening model was shown to be adequate for characterizing the coarsening process during VTS. Particles grow by condensation of newly formed Cl-apatite on the precursor grains, thus facilitating grain growth by accretion. Surface diffusion as an alternative shrinkage-free process of material transport was shown to be ineffective regarding the stimulation of pore and grain coarsening.

To conclude, VTS processing of β-TCP and BCP ceramics provides a ceramic scaffold structure with fully interconnected porosity and holds potential for the near-net-shape manufacturing of custom-made ceramics. However, since the pore diameters attainable via VTS are limited to about 5 µm, it needs to be combined with other processing techniques to create adequate macroporosity with diameters on the order of 100-500 µm to meet the requirements for bone graft applications. Despite this limitation, the fine dispersion of Ag-bearing particles throughout the scaffold's interior, caused by AgCl-sintering, seemed promising with regard to an antibacterial modification of the material. Therefore, this approach was followed applying VTS in AgCl atmosphere to macroporous scaffolds derived from biogenic precursors, as reported in the following chapter.

5. Vapor Transport Sintering of Biogenic Scaffolds

5.1. Introduction to the Hydrothermal Conversion of Carbonates

Among the various processes devised for the fabrication of calcium phosphate scaffolds, the hydrothermal conversion of coral skeletons ($CaCO_3$; aragonite) into hydroxyapatite is well-established, as the pore volume and geometry of the precursor material match the requirements for bone graft applications.[19,82,246] The phase conversion takes place according to the following reaction:

$$10CaCO_3 + 6(NH_4)_2HPO_4 + 2H_2O \xrightarrow{180°C} Ca_{10}(PO_4)_6(OH)_2 + 6(NH_2)CO_3 + 4H_2CO_3$$

In clinical studies, scaffolds produced by this method have shown favorable properties with regard to cell apposition and differentiation, followed by *de novo* bone formation.[247] During the conversion process, the macroscopic structure of the coral is preserved, while the phase composition changes due to locally coupled dissolution and recrystallization.[248] However, this method is not restricted to the pseudomorphic replacement of coralline aragonite, but it can equally be applied to both biogenic and inorganically formed calcite.[248-253]

Efforts have been made to enhance the clinical performance of calcium phosphate implants by modification with antibacterial agents. Several studies on Ag-modifications applied to a range of calcium phosphate materials have demonstrated the viability of the concept, as detailed in 2.3.5. Using AgCl as a vapor transport sintering (VTS) agent, the surface modification with finely dispersed AgCl is possible due to particle condensation throughout the scaffold's interior. As shown in chapter 4, VTS allows thermal treatment of calcium phosphates with near-zero shrinkage. However, pore coarsening stagnates after holding times of several hours and the maximum average pore size obtained for powder-derived HA–TCP composites was ca. 5 µm after 6 h. Because of this limitation, VTS needs to be combined with other techniques to create the macroporosity required for bone graft applications.

For this feasibility study, two processing methods have been combined for the fabrication of macroporous calcium phosphate scaffolds with antibacterial properties: (i) hydrothermal conversion of biogenic carbonates and (ii) vapor transport sintering in chlorargyrite (AgCl) atmosphere, as a novel approach for the surface modification of calcium phosphate scaffolds with Ag-bearing particles.

5.2. Experimental Procedure

5.2.1. Hydrothermal Conversion and Sintering

Two biogenic carbonate minerals were selected as precursor materials for this study: coral skeletons (*Porites sp.*; aragonite) and sea urchin spines (*Heterocentrotus mammillatus*; Mg-bearing calcite). Aliquots of the sample material were cleaned in H_2O_2 for 6 h to remove organic residue. Hydrothermal conversion into calcium phosphate was accomplished by immersion in one-molar solution of $(NH_4)_2HPO_4$ within Teflon™-lined autoclaves that were held in a box furnace at 180°C for two weeks. Before and after thermal treatment, the autoclaves were weighed and evaporation losses were found to be consistently below 0.5 wt%. Afterwards, the samples were rinsed thoroughly with deionized water and dried at 110°C for 6 h. To obtain enough sample material for characterization, 15 g of each precursor mineral were converted in five autoclave runs. After conversion, samples were sealed off in evacuated silica ampoules together with an AgCl powder additive (0.3 g per 1 g sample material) which creates a reactive chloride atmosphere at elevated temperatures. VTS was carried out at 1100°C for 6 h.

5.2.2. Analytical Methods

Chemical analysis of the precursor materials was performed with a S8 Tiger wavelength dispersive X-ray fluorescence instrument (WDXRF; Bruker, Karlsruhe, Germany). To account for matrix absorption effects, CaO was assumed to be present in the form of calcite ($CaCO_3$), SO_3 as gypsum ($CaSO_4 \cdot 2H_2O$) and Na_2O as halite (NaCl). This seems plausible with regard to the marine environment in which the biogenic carbonates were formed. Moreover, the phase composition of samples from all processing stages was analyzed with powder XRD. Additionally, the coral-derived samples were analyzed after both conversion and subsequent free sintering with DRIFTS. Characterization of the microstructure was performed at all processing stages by SEM with integrated EDS. For this purpose, fracture surfaces were carbon sputtered to minimize charging under the electron beam. To determine the average pore diameters (Feret's diameter) from SEM images of polished samples, the Image J software package (ImageJ 1.45b, National Institutes of Health, U.S.A.) was used. TEM imaging of selected samples was performed by Stephanie Schultheiss using an FEI CM20 microscope equipped with a Gatan double tilt holder at a nominal acceleration voltage of 200 kV. TEM specimens were prepared as thin sections by polishing and subsequent ion milling to perforation.

To assess the availability of Ag^+ ions, the dissolution kinetics of AgCl and Ag_3PO_4 powder, metallic Ag, as well as Ag-modified ceramics were studied. Dissolved Ag^+ was measured as a function of time, using a silver ion-selective electrode (ISE). The electrode was calibrated against a series of $AgNO_3$ solutions with concentrations of 0.01, 0.1, 1, 10 and 100 mg/l. The Nernst gradient determined from the linear range of the standard curve was in good agreement with the theoretical value of 61.5 mV at 37°C. Batches of 50 mg of the powder reagents, a silver ring, as well as pieces of the coral- and sea urchin derived ceramics corresponding to 50 mg AgCl reagent (0.3 g reagent per 1 g ceramic) were each immersed into 98 ml deionized water with 2 ml of $NaNO_3$ (5 mol/l) added for ionic strength adaption and held at 37°C. Analyses were carried out under constant stirring until solubility equilibrium was reached, which generally occurred after a few hours. To prevent chemical alteration of the light-sensitive Ag-compounds, experiments were conducted in darkness.

5.2.3. Antibacterial Testing

In collaboration with the Chair of Microbiology and Archaea, Department of Biology, Technische Universität Darmstadt, the antibacterial properties of the Ag-modified ceramics were tested against *Staphyloccocus aureus* DSM 1104 and *Pseudomonas aeruginosa* DSM 1117. Both strains were cultivated in yeast extract dextrose (YED, 5 g/l peptone, 2.5 g/l yeast extract, 1 g/l glucose at pH 7.0) medium at 37°C and 180 rpm. To assess the antimicrobial properties of the ceramic samples (coral and sea urchin Ag-modified and non-modified), specimen were ground and 10 mg powder placed on agar plates (YED with agar 15 g/l), top layered with seeded soft agar (YED with agar 10 g/l, containing 10^8 cfu/ml). Inoculated plates were pre-incubated for 2 h at 4°C and 15 h at 37°C. After growth, five zones of inhibition (in mm) were measured per sample, starting from the outer rim of the ceramic powder. To analyze the bacterial inhibition in liquid, 50 mg powder of AgCl, Ag_3PO_4 and Ag-modified ceramic (coral) were immersed into 100 ml deionized water and stirred over night at room temperature. The solutions were adjusted to an Ag^+ concentration of 1 mg/l. Then, 1.8 ml of the solutions were transferred to a 2 ml reaction tube, mixed with 0.2 ml 10 x YED medium, serially diluted (0.9, 0.45, 0.23, 0.11, 0.06 mg/l), inoculated with a fresh over night culture of *Pseudomonas aeruginosa* (final cell suspension 1.8×10^4 cfu/ml) or *Staphyloccocus aureus* (final cell suspension 0.8×10^4 cfu/ml), respectively, and incubated for 26 h at 37°C. After incubation, bacterial growth was evaluated via optical density (OD) at 580 nm. All antimicrobial tests were performed in triplicates and conducted under ruby light.

5.3. Results and Discussion

5.3.1. Chemical and Phase Analysis

5.3.1.1. XRF

Wavelength-dispersive XRF was applied for the identification of chemical impurities within the carbonate precursor materials (c.f. *Experimental*); the results are summarized in Table 2. A notable difference between the two biogenic materials is the much higher amount of MgO in the sea urchin spine (3.96 wt%), as compared to the coral (0.31 wt%) which was found to favor the formation of Mg-TCP over HA during hydrothermal conversion (c.f. 5.3.1.2, Table 3). Correlations between Mg-content and β-TCP stabilization upon heating have been reported for both calcified tissues and synthetic calcium phosphates.[254-256] Other impurities were present in low concentrations only.

Table 2: Carbonate precursor chemistry as determined by WDXRF (in wt%).

	MgO	**CaO**	**Na_2O**	**P_2O_5**	**CO_2**	**H_2O**	**SO_3**	**Cl**	**Sr**	**Total**
Coral	**0.31**	52.63	0.51	<0.03	40.99	0.26	0.58	0.58	0.79	96.65
Sea urchin	**3.96**	52.67	0.75	<0.03	40.81	0.42	0.94	0.86	0.20	100.61

5.3.1.2. XRD

XRD analyses were performed to characterize changes in the phase composition during the subsequent processing steps, as summarized in Table 3. The precursor minerals were confirmed to be aragonite (coral; PDF 00-041-1475) and Mg-bearing calcite (sea urchin; PDF 00-043-0697); the corresponding diffractograms are not shown here. For both coral- and sea urchin-derived samples, the phase conversion from carbonate to phosphate was complete (Figures 34a and 35a). Generally, both stoichiometric and Ca-deficient HA (Ca/P ratio: 1.67 and 1.67-1.5, respectively) are more stable than β-TCP (Ca/P ratio: 1.5) under hydrothermal conditions.[84,93] However, substitution of Mg^{2+} for Ca^{2+} is possible only to a limited extent in HA, given that no further substitution reactions are physically compensating for the small ionic radius of Mg^{2+}.[11,257,258] In contrast, Mg^{2+} is readily incorporated into β-TCP occupying up to 14% of the cation sites, and preferably so if it is co-precipitated with HA.[259-261] Thus, Mg-bearing β-TCP (Mg-TCP) was formed under the given hydrothermal conditions. Corresponding to the Mg-concentrations of the precursor materials (Table 2), Mg-TCP was detected only in small amounts in coral-derived samples, but as the dominant phase in sea urchin-derived ones upon hydrothermal conversion.

For assessing phase stoichiometry, converted samples were subjected to free sintering in air at 1100°C for 6 h. Ca-deficient HA can be distinguished from stoichiometric HA by its partial or full decomposition into β-TCP upon thermal treatment, depending on the initial Ca/P ratio.[84] For the coral-derived sample, the relative amount of Mg-TCP increased upon free sintering, indicating a moderate Ca-deficiency (Figure 34b). Regarding the sea urchin-derived sample, Ca-deficiency in the converted sample was revealed by the disappearance of the minor HA phase and the formation of Ca-pyrophosphate ($Ca_2P_2O_7$; Ca/P ratio: 1.0) upon free sintering (Figure 35b). The Ca-deficiency observed in both materials is evidently caused by some degree of CO_3^{2-} substitution at the PO_4^{3-} site in the apatite lattice that is compensated by one ½ Ca^{2+} vacancy to retain charge balance (B-type substitution).[262-264] Due to the decomposition of the $CaCO_3$ precursor during hydrothermal conversion, dissolved CO_3^{2-} is available in great quantity. Since the CO_3^{2-} groups within HA are not thermally stable,[11,265] though, the substitutional reaction was revealed by phase transformations upon free sintering.

VTS of coral-derived samples in AgCl atmosphere lead to the partial substitution of OH-groups with Cl^- in the apatite lattice, as indicated by peak shifts in the diffractogram (Figure 34c). However, Cl^- is a common impurity in human bone,[266] so this should have no bearing on the material's prospective medical use. Moreover, VTS had no observable effect on the stability of Mg-TCP present in both sample materials (Figures 34c and 35c). This is remarkable, as pure β-TCP readily transforms into Cl-apatite that is necessarily Ca-deficient.[237] However, analogous to the hydrothermal setting, the presence of Mg^{2+} shifts the phase stability in favor of Mg-TCP also under VTS conditions. Generally, the substitution of Mg^{2+} for Ca^{2+} in β-TCP was reported to have favorable effects with regard to ceramic processing, by enhancing densification behavior, thermal stability and mechanical properties, as compared to the pure phase.[232] Unfortunately, the major diffraction peaks of AgCl overlap those of apatite. This precludes the analysis of small amounts of the latter phase in sea urchin-derived samples (Figure 35c).

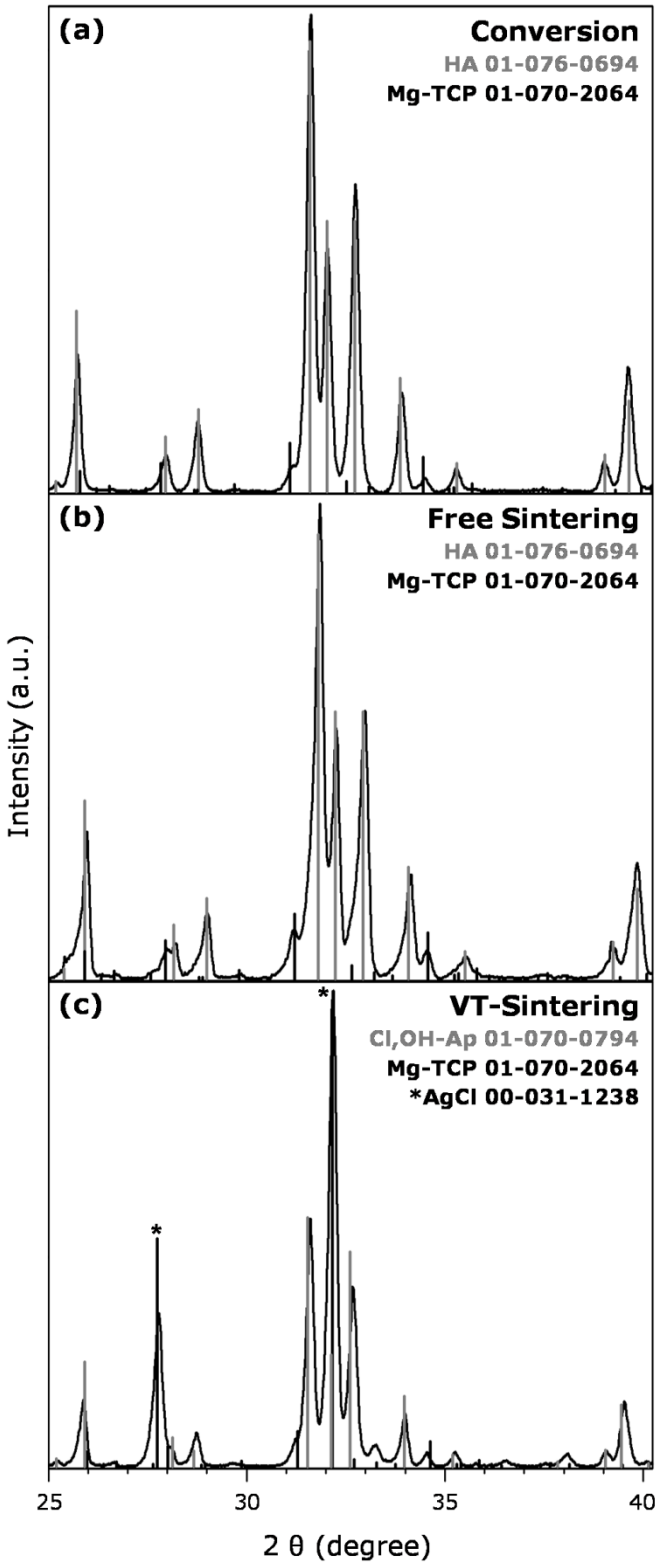

Figure 34: X-ray diffractograms of a coral-derived calcium phosphate scaffold (a) after hydrothermal conversion and after sintering at 1100°C for 6 h in (b) air and (c) in AgCl atmosphere. Numerical codes specify the powder diffraction file (PDF).

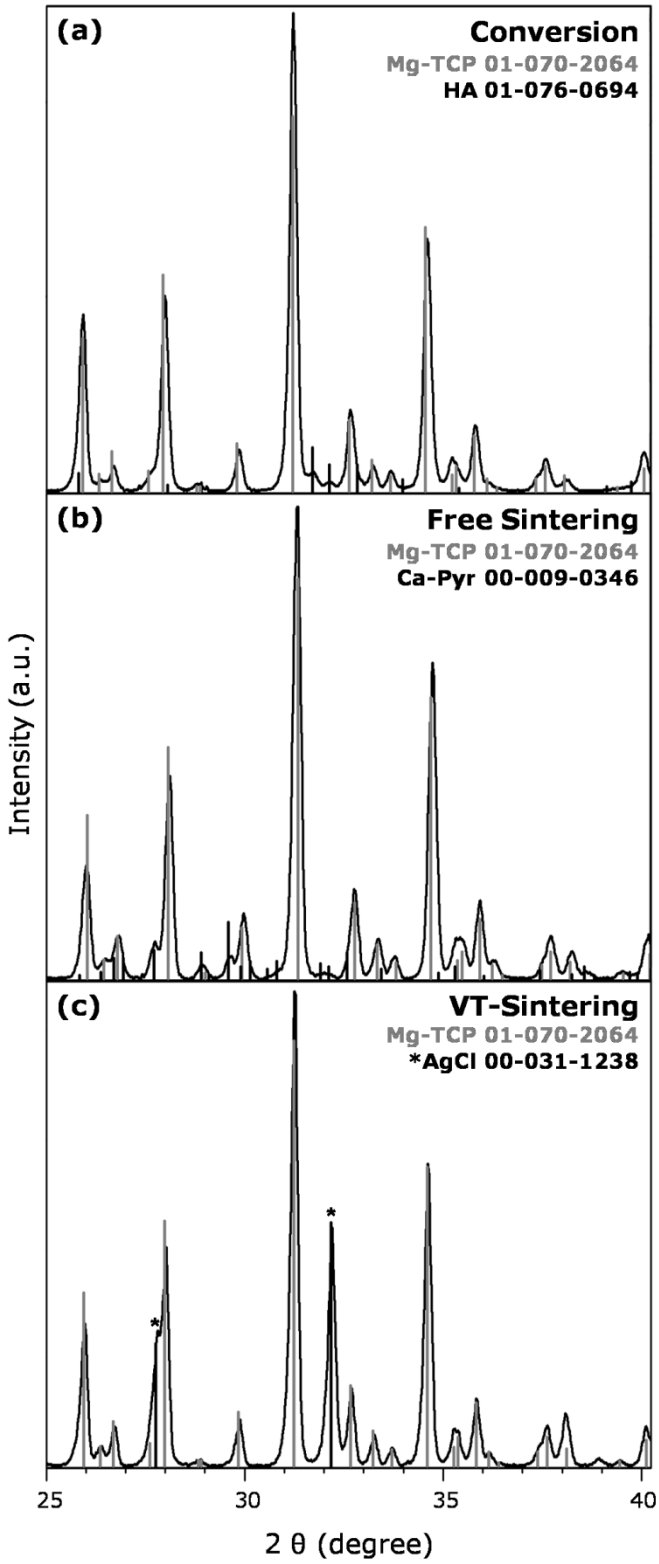

Figure 35: X-ray diffractograms of a sea urchin-derived calcium phosphate scaffold after (a) hydrothermal conversion and after sintering at 1100°C for 6 h in (b) air and (c) in AgCl atmosphere. Numerical codes specify the powder diffraction file (PDF).

Table 3: Phase chemistry as determined by XRD; major phase(s) underlined.

Coral	Precursor	Aragonite
	After hydrothermal conversion	HA, Mg-TCP
	After free sintering (1100°C, 6 h)	HA, Mg-TCP
	After VTS in AgCl (1100°C, 6 h)	Cl-HA, Mg-TCP; AgCl[#]
Sea urchin	Precursor	Mg-Calcite
	After hydrothermal conversion	Mg-TCP, HA
	After free sintering (1100°C, 6 h)	Mg-TCP, Ca-Pyrophosphate
	After VTS in AgCl (1100°C, 6 h)	Mg-TCP; AgCl[#]

[#]Photosensitive Ag_3PO_4 was not determined.

5.3.1.3. FTIR (DRIFTS)

To document the presumed carbonate substitution leading to Ca^{2+}-deficiency in HA upon hydrothermal conversion, the coral-derived samples were analyzed by DRIFTS both after conversion and subsequent free sintering. There are two positions that a CO_3^{2-} ion can possess within the apatite lattice: it may either replace two OH^- ions on the six-fold screw axis (A-type), or one PO_4^{3-} ion (B-type). The latter substitution is accompanied by the formation of one ½ Ca^{2+} vacancy to retain charge balance.[262-264] Considering the substitutions as point defects within the lattice, the reactions can be expressed in Kröger-Vink notation:[267]

$$\text{A-type:} \quad CO_3^{2-} \xrightarrow{HA} CO_{3\,OH^-}' + V_{OH}^{\bullet}$$

$$\text{B-type:} \quad CO_3^{2-} \xrightarrow{HA} CO_{3\,PO_4^{3-}}^{\bullet} + \tfrac{1}{2}\, V_{Ca}^{''}$$

Due to the complex chemical situation during hydrothermal conversion, namely the potential contributions from bicarbonate, hydrogen phosphate and adsorbed carbonate ions, as well as the resulting two-phase composition (HA and Mg-TCP), the corresponding IR absorption bands tend to be rather broad.[11] However, good agreement was found with several studies concerned with hydrothermal conversion, namely that of Hu et al. on corals (B-type),[251] Rocha et al. on cuttlefish bone (AB-type),[252] as well as that of Zaremba et al. on gastropod nacre (A-type).[248] After hydrothermal conversion, the IR spectrum showed

several bands indicative of carbonate groups in both A-type (1545, 1450 and 880 cm^{-1}) and B-type positions (1465, 1412 and 873 cm^{-1}) (Figure 36a).[268] Moreover, the band at 2340 cm^{-1} is characteristic of molecular CO_2 trapped in the apatite lattice.[269]

Subsequent free sintering at 1100°C for 6 h had several effects on the carbonate apatite structure. While the intensity of the vibrational bands related to the B-type substitution nearly vanished, it decreased only slightly for the A-type bands (Figure 36b). This can be explained by CO_3^{2-} ions migrating from the PO_4^{3-} to the OH^- ion site upon heating.[270] As the Ca^{2+} vacancies are not stabilized any longer, a partial phase transformation into β-TCP occurs, as determined with XRD (Figure 34a). Under the given experimental conditions of sintering in ambient (i.e. humid) atmosphere, CO_3^{2-} ions in A-sites will become substituted by OH^- groups over time,[270] as confirmed by a corresponding increase of the OH^- stretching band at 3572 cm^{-1}.[11] The overall decline in intensity observed for carbonate-related bands indicates the diffusion of carbonate ions from both A- and B-sites out of the lattice. Moreover, molecular CO_2 was released during sintering, as marked by the disappearance of the corresponding band at 2340 cm^{-1}.

Although carbonate groups are driven out of the apatite lattice upon heating, it can be stated that the major phases of the converted materials remain stable during VTS. Therefore, depending on the specific application, both HA and Mg-TCP scaffolds can be produced starting from coral skeletons or sea urchin spines, respectively.

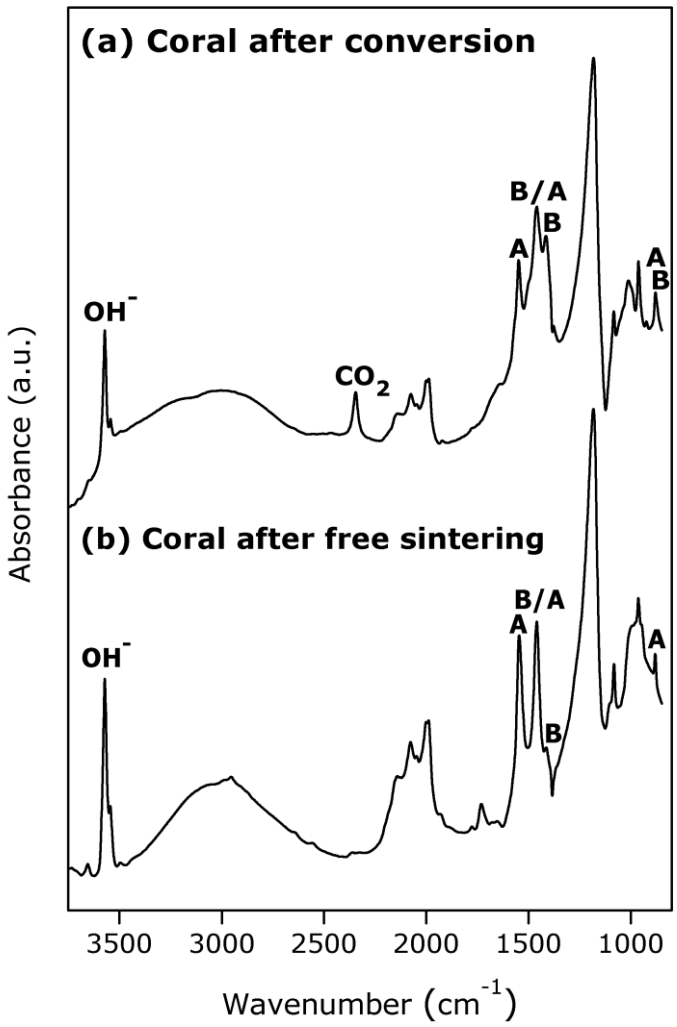

Figure 36: DRIFTS spectrum of coral-derived calcium phosphate scaffolds after (a) hydrothermal conversion and (b) subsequent free sintering at 1100°C for 6 h. Changes between the two spectra document the loss of carbonate groups from the apatite structure, particularly from B-type substitutional sites. Please note that in the TCP-based samples (i.e. sea urchin-derived) no site specific ion exchange reactions took place and hence corresponding spectra are not shown here.

5.3.2. Microstructure Development

Hydrothermal conversion of calcium carbonates into calcium phosphates was carried out to retain the intricate structures of coral skeletons and sea urchin spines which are characterized by an interconnected macroporosity. During the conversion process, the crystalline fabric of the precursor is replaced without structural coherency by a finer grained microstructure with nanoporosity compensating for a volume loss of 6 % for aragonite – HA and 12.7 % for the calcite – HA transition,[253] as demonstrated by TEM imaging (Figure 37).

During VTS, sample shrinkage is generally much reduced compared to free sintering in air.[222,237] Moreover, particles of the volatile AgCl sintering agent condensed throughout the

ceramic scaffold, as determined with EDS. Condensate size was restricted by the containing pores (Figures 38 and 39). Statistical analysis of SEM images confirmed that the average macropore size of hydrothermally converted coral- and sea urchin scaffolds was not affected by the sintering process and remained constant at ca. 200 µm and 30 µm (Feret's diameter), respectively. In contrast, microporosity contained inside the *trabeculae*, i.e. the scaffold's struts, was subject to coarsening.

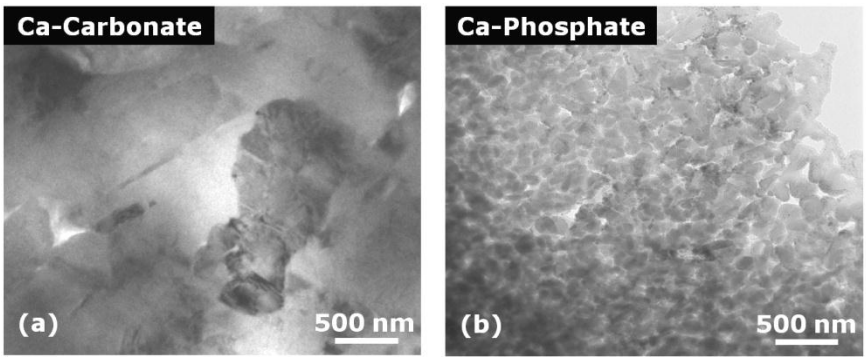

Figure 37: TEM images (bright field) of a coral skeleton (a) before and (b) after hydrothermal conversion from calcium carbonate (aragonite) into calcium phosphate (hydroxyapatite). The crystalline precursor material is replaced without structural coherency by a finer grained, nanoporous fabric. Images courtesy of S. Schultheiss.

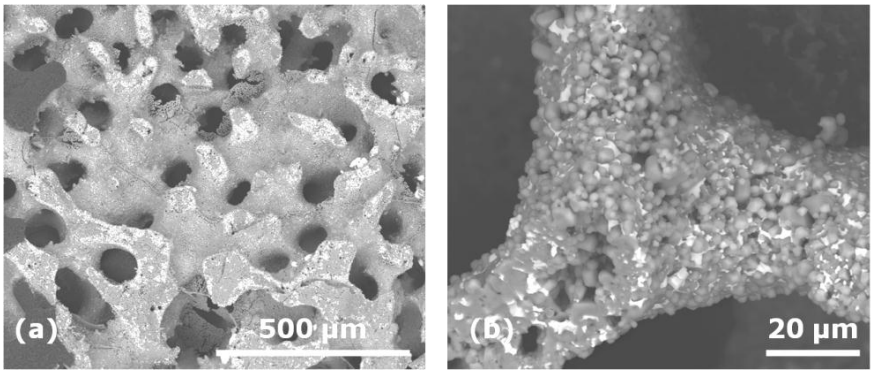

Figure 38: SEM images (BSE) of a coral-derived Ca-phosphate ceramic after vapor transport sintering at 1100°C for 6 h; (a) interconnected macroporosity of the material and (b) microporosity partly filled with fine AgCl particles (white; Z-contrast).

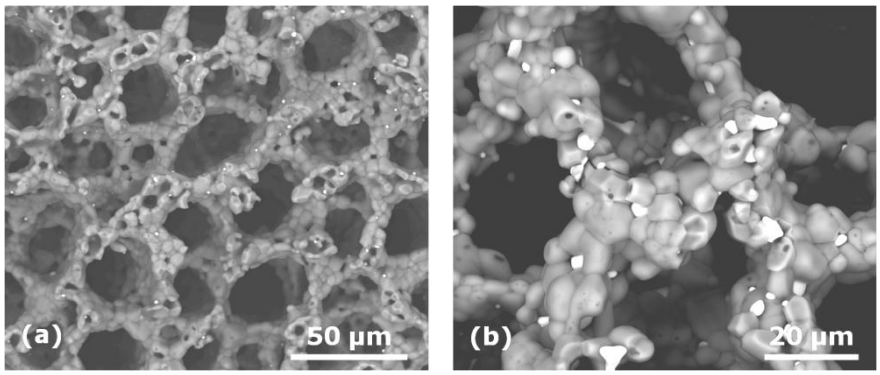

Figure 39: SEM images (BSE) of a sea urchin-derived Ca-phosphate ceramic after vapor transport sintering at 1100°C for 6 h; (a) interconnected macroporosity of the material and (b) microporosity partly filled with fine AgCl particles (white; Z-contrast).

5.3.3. Assessment of Antibacterial Properties

5.3.3.1. Ag^+-Release into Solution

As Ag^+ release into aqueous solution is a precondition to antibacterial activity, it was measured as a function of time for AgCl and Ag_3PO_4 powder, metallic Ag and both coral- and sea urchin-derived Ag-modified ceramics. Ag^+-concentration measurements showed that Ag^+ ions were released from the Ag-modified ceramics immediately upon immersion in aqueous solution (Figure 40). Within a few hours, solubility equilibria were reached, stressing the ceramics' potential for antibacterial action. Calculation of Ag^+ concentrations at solubility equilibrium from electrode potentials reached after 18 h of immersion gave values of 28.6 mg/l for Ag_3PO_4 and 2.03 mg/l for AgCl. Ag^+ concentrations derived from metallic silver constantly remained below the detection limit of the electrode (<0.1 mg/l). Concentration values for the Ag-modified ceramics were intermediate between that of the pure reagents, indicating that a mixture of the Ag-containing phases had formed during sintering. The Ag^+ solubility equilibrium obtained for the coral-derived ceramic was 3.87 mg/l, falling in between the values for AgCl and Ag_3PO_4 which points to the presence of both phases. Although the light-sensitive Ag_3PO_4 was not detected with XRD, a yellowish tinge on the sample's surface supports the assumption that it was formed during vapor transport sintering of the HA-based ceramic. Further evidence for the formation of Ag_3PO_4 derived from antibacterial testing in solution is discussed below. In contrast, the final concentration induced by the sea urchin-derived sample was 0.74 mg/l, i.e. in between the values for AgCl and metallic silver. This can be explained by the loss of Cl^- due to the formation of small amounts of Cl-apatite, thereby reducing AgCl to metallic silver, or possibly due to sample aging during storage. To further test these assumptions, experiments were conducted under otherwise same conditions for phase mixtures of

Ag_3PO_4 – AgCl powder (25 mg each) and AgCl – metal (50 mg powder; silver ring). Good agreement was achieved with the Ag^+ release rate of coral- and sea urchin-derived ceramics, respectively, which supports the presence of phase mixtures on the ceramic surfaces (Figure 41). Deviations occurring after ca. 2 h of immersion may be due to specific interactions between ceramic and solution, since depletion of the Ag^+-source which was present in excess can be ruled out.

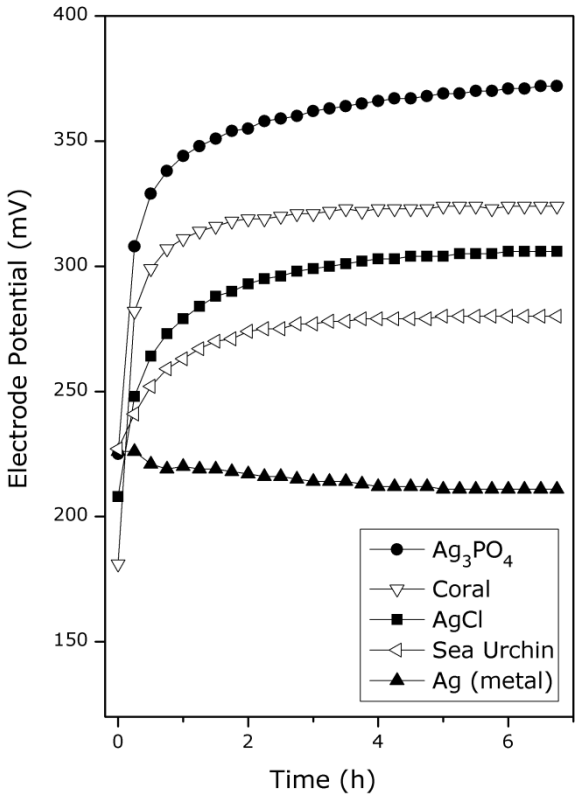

Figure 40: Ag^+-release into deionized water at 37°C determined for various Ag-containing compounds as a function of time.

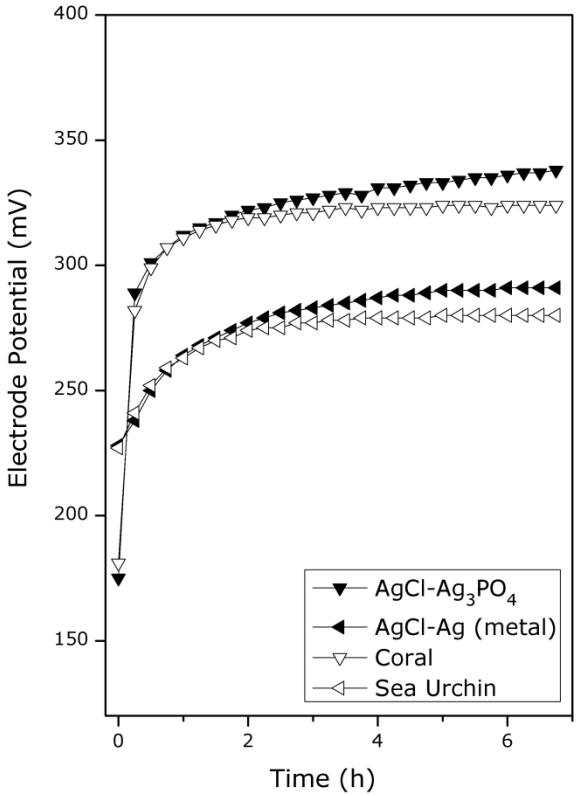

Figure 41: Ag^+-release into deionized water at 37°C determined for various Ag-containing compounds as a function of time.

5.3.3.2. Bacterial Strain Testing

Biomineral-derived ceramic samples (Ag-modified and reference), as well as solutions containing Ag^+ dissolved from AgCl and Ag_3PO_4 powders were tested with respect to their antibacterial properties against two bacterial strains, the Gram-negative *Pseudomonas aeruginosa* and the Gram-positive *Staphyloccocus aureus*. Both of them are commonly found in infected wounds in humans forming polybacterial biofilms impairing wound healing.[271] Experiments were conducted in collaboration with Sabrina Fröls and Felicitas Pfeifer at the Department of Biology, Technische Universität Darmstadt.

Bacterial growth inhibition was tested on seeded agar plates with a known number of bacteria (10^8 cfu/ml) and inoculated with ceramic powders, both Ag-modified and non-modified. Only Ag-modified ceramics showed a distinct antibacterial effect against *Pseudomonas aeruginosa* and *Staphyloccocus aureus*, whereas no growth inhibition effects were observed for the non-modified ceramics (Figure 42a). Analysis of the zone of inhibition showed that growth inhibition was stronger against the Gram-positive test strain, relative to the Gram-negative one (Figure 42b). These results are consistent with the known antibacterial effect of silver nanoparticles.[272] No substantial differences were found between the coral- and sea urchin-derived ceramics tested, *i.e. Pseudomonas aeruginosa*

(coral 2 ±0.12, sea urchin 1.9 ±0.18, n=15) and *Staphyloccocus aureus* (coral 4.1 ±0.34, sea urchin 3.1 ±0.18, n=15).

Serial dilutions of Ag^+-containing solutions prepared from Ag-modified coral ceramic, AgCl and Ag_3PO_4 powders with Ag^+ concentrations adjusted to values ranging from 0.9 mg/l to 0.06 mg/l were inoculated with equal amounts of bacteria (10^4 cfu/ml). Bacterial growth was monitored by the optical density at 580 nm after incubation. At the same ionic concentrations, the antibacterial effect of Ag_3PO_4 was up to 12 times stronger, as compared to AgCl. Moreover, the inhibitory effect of the Ag^+ ion solution derived from the Ag-modified coral ceramic was intermediate (Figure 43). This effect can be attributed to the formation of Ag_3PO_4 during VTS, as supported by sample color and the ion-selective electrode measurements. Within the AgCl sintering atmosphere, volatile phosphate is available to react with silver to form Ag_3PO_4.

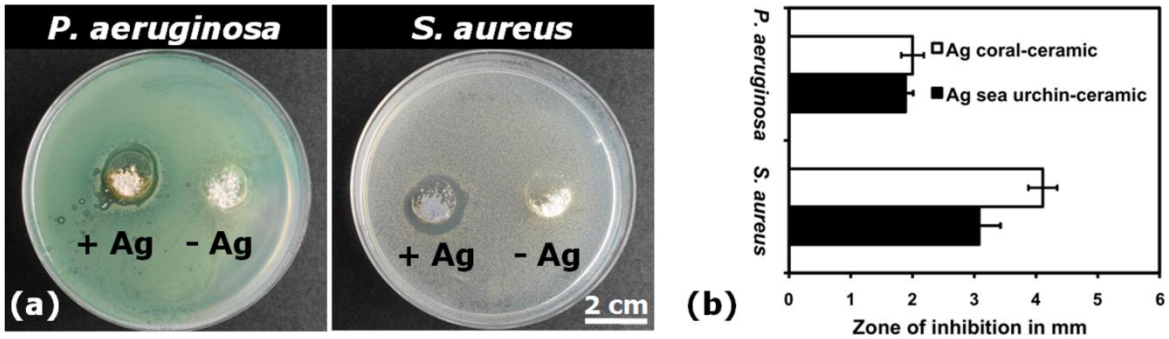

Figure 42: Antibacterial effects of Ag-modified ceramics on Gram-negative (*Pseudomonas aeruginosa*) and Gram-positive strains (*Staphyloccocus aureus*). (a) Seeded agar plates inoculated with coral-derived ceramic powder, Ag-modified (+Ag) and non-modified (-Ag); (b) zone of inhibition analysis of Ag-modified coral- and sea urchin-derived ceramic powder, each bar represents the average of 15 measurements.

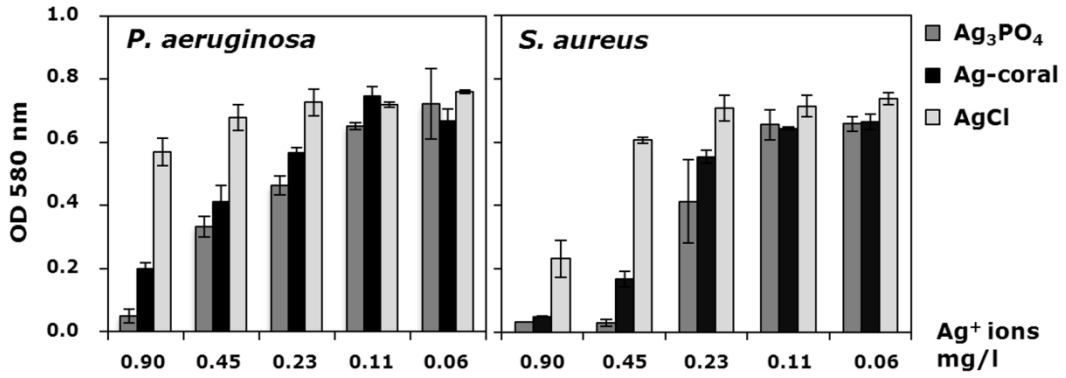

Figure 43: Optical density (OD) at 580 nm measured after 26 h in the presence of Ag^+ solutions (prepared with Ag_3PO_4, AgCl and Ag-modified coral-derived ceramic). Inocula of 10^4 cfu/ml were used for both *Pseudomonas aeruginosa* and *Staphyloccocus aureus*.

5.4. Chapter Conclusion

The combination of two processing methods, namely (i) hydrothermal conversion of biogenic carbonate scaffolds and (ii) vapor transport sintering in AgCl atmosphere, produces the interconnected pore geometry and phase composition as required for bone graft ceramics, along with a surface modification of Ag-containing phases. The Mg-content of the carbonate precursor materials used, i.e. coral skeletons and sea urchin spines, determines the phase composition of the conversion product by stabilizing Mg-bearing β-TCP at the expense of HA. Sintering in AgCl atmosphere facilitates both, microstructural coarsening without macropore shrinkage, as well as the condensation of finely dispersed AgCl and Ag_3PO_4 particles throughout the scaffold. Representing a novel class of ceramic composites, these materials are promising with regard to the antibacterial properties of Ag^+ ions. Moreover, the major phases present in the converted scaffolds remain stable during VTS, allowing the fabrication of both HA and Mg-TCP ceramics.

By determining dissolution kinetics, it could be shown for both types of Ag-modified ceramics that Ag^+ was immediately released into aqueous solution and reached solubility equilibrium within a few hours. Thus, Ag^+ availability as the precondition for antibacterial activity is given. Moreover, both Ag-modified ceramics showed an antimicrobial effect, which was stronger for Gram-positive bacteria than for Gram-negative bacteria. Growth inhibition studies with Ag^+ solutions suggest that the antibacterial effect of the ceramic was caused by a phase mixture of AgCl and Ag_3PO_4 present on the surface of the ceramic scaffold.

6. Thermodynamical Calculations

6.1. Introduction[***]

For a given temperature, the vapor pressure over a condensed phase has a distinct value; i.e. the *equilibrium vapor pressure* of sublimation. If an additional pressure acts upon the system – as exerted, for example, by an inert gas – the vapor pressure rises; it is then denoted as *equilibrium partial pressure*. Moreover, in a system that comprises condensed phases, as well as phases that exclusively occur in the vapor phase – such as water at temperatures beyond the critical point –, equilibrium will form (i) between each condensed phase and the corresponding vapor phase, and (ii) between the reaction products of all volatile species. Again, for such a complex system, the partial pressure of any volatile species in equilibrium with the corresponding condensed phase(s) is exactly determined by its thermodynamical properties, namely the enthalpy of sublimation.

However, the surface curvature of the condensed phase has an influence on the local partial pressure, with values over concave surfaces being lower relative to a flat plane. This is due to corresponding differences in the surface energy of the condensed phase. For instance, the vapor pressure over the small negative radius of a sintering neck is reduced, according to the Kelvin equation:[274]

$$RT \ln\frac{P_1}{P_0} = \frac{M\gamma}{d}\left(\frac{1}{\rho}+\frac{1}{x}\right) \qquad \text{(Kelvin equation)}$$

with ideal gas constant, R, temperature, T, equilibrium partial pressure over a flat surface, P_0, and over a curved surface, P_1, molecular weight, M, surface energy, γ, density, d, radius of the neck, ρ, and radius of the grain boundary, x.

Assuming that gas diffusion is rapid during vapor phase transport, the equilibrium partial pressures of volatile species indicate the potential for neck and particle growth via this route at sintering temperature. As will be demonstrated for several systems of interest, the equilibrium partial pressure of a species can be influenced via sintering temperature and system pressure. Moreover, the presence of highly reactive halides promotes the formation of volatile species, such as $CaCl_2$, that act as a carrier for the otherwise immobile calcium.

For clarity of presentation, the figures displayed in this chapter are reduced to information on the most relevant species. Fully annotated graphs, together with supplementary data, are provided in the Appendix.

[***]If no other source is referred to in this chapter, recourse to the handbooks of Atkins (1994)[205] and Gaskell (1981)[273] has been made.

6.2. Experimental Procedure

Thermodynamical calculations were carried out using the Thermo-Calc™ software package (Thermo-Calc Software, Stockholm, Sweden) in combination with the SGTE Substances Database (version SSUB 4). Calculations were restricted to reactions of pure TCP with various sintering agents, as no data were available for HA and Cl-apatite. The ambient atmosphere was modeled to be inert, consisting of pure Ar.

The work was carried out in collaboration with the working group of Prof. Dr. Hans Seifert, Karlsruhe Institute of Technology. Their valuable suggestions and practical help are gratefully acknowledged.

6.3. Results and Discussion

6.3.1. Equilibrium Partial Pressures for Free Sintering Conditions

For assessing the contribution of mass transport through evaporation and re-condensation during free sintering of β-TCP, the partial pressures of volatile species were calculated as a function of temperature. To estimate the importance of vapor transport relative to volume diffusion, the following equation was derived by Readey:[222]

$$\frac{\dot{x}_{VT}}{\dot{x}_D} \approx 4 \times 10^{-11} \frac{p_0}{D}$$

With rate of neck growth due to vapor transport, $\dot{x}_{VT}$, and due to volume diffusion, $\dot{x}_D$, partial pressure of the vaporizing species, p_0, and the volume diffusion coefficient, D. The units of p_0 and D are Pa and $cm^2 s^{-1}$, respectively.

For vapor transport to exert a significant influence on the coarsening process, the rate-determining species should theoretically have a partial pressure of at least 10^{-5} bar. Free sintering conditions for TCP were modeled for ambient atmosphere (considered inert) and 1 bar system pressure (Figure 44). The partial pressures of the relatively abundant P-carriers PO_2, PO, P_2O_5, P_2O_3, listed in order of their occurrence at 1100°C, all remain below 10^{-8} bar. Gaseous Ca and CaO both occur in negligible amounts with vapor pressures below 10^{-21} bar. As the slowest reactions are rate-determining, the lowest partial pressure of all relevant volatile species, i.e. that calculated for Ca, and the lowest volume diffusion coefficients, i.e. those of PO_4^{3-} with $D_{\parallel} = 1.2 \times 10^{-12} cm^2 s^{-1}$ and $D_{\perp} = 3.6 \times 10^{-12} cm^2 s^{-1}$ (at 1700K)[275] need to be taken into account for an estimation of the relative importance of material transport via the vapor phase and through the sample volume. Putting these values into the above equation, the neck growth rate due to vapor transport

turns out to be smaller by a factor of 10^{-16}, as compared to volume diffusion. Therefore, no substantial contribution of evaporation – condensation to mass transport would be expected during free sintering. However, as demonstrated below, there is a discrepancy between our theoretical calculations and experiments demanding further explanation: Vapor transport sintering was successfully carried out even for systems with calculated minimum partial pressures as low as $>10^{-9}$ bar for $POCl_3$ in the system β-TCP-H_2O-HCl at 50 bar (Figure 49d). To reconcile these findings, we propose that vapor transport sintering is driven by the phase conversion from β-TCP into more stable Cl- or Br-apatite, depending on the halide reagent used. Volatile species in equilibrium with β-TCP are constantly removed from the sintering atmosphere by apatite condensation and β-TCP constantly evaporates to sustain this equilibrium. Therefore, much more material is mobilized than is indicated by the low values calculated for the relevant species.

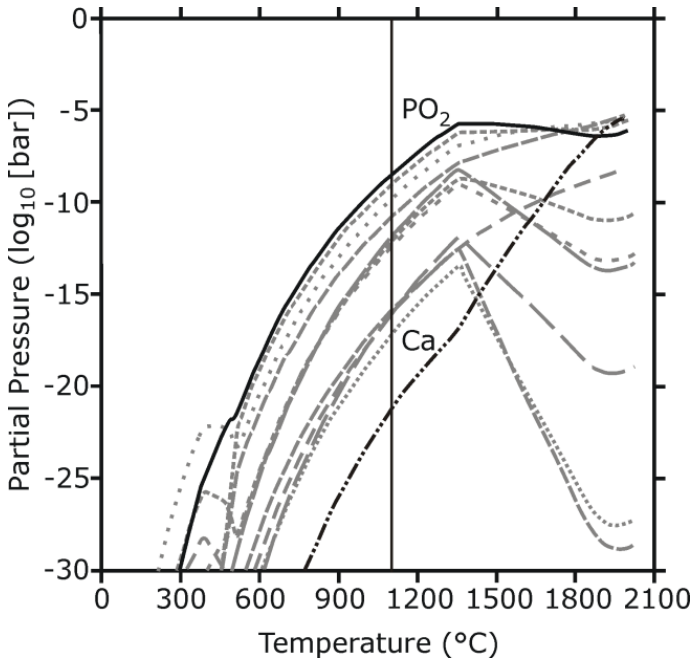

Figure 44: Partial pressures of volatile species in equilibrium with TCP. Whereas oxidized phosphorus is relatively abundant within the sintering atmosphere, the partial pressure of calcium is negligible at 1100°C.

6.3.2. Equilibrium Partial Pressures of the Sintering Agents

At 1100°C, i.e. the standard holding temperature of our sintering experiments, halide acid reagents are exclusively present in the gaseous state. Our calculations confirm the high availability of reactive halides over a broad temperature range, as exemplified for hydrochloric acid (Figure 45). Regarding halide sintering additives that are solid at room temperature and liquid under sintering conditions, our calculations showed that all possess

relevant partial pressures in the sintering atmosphere, with values of $>10^{-4}$ bar for $CaCl_2$, and$>10^{-2}$ bar for both $MgCl_2$ and AgCl (Figure 46; c.f. Appendix). Thus, they are available to form volatile species by reaction with the calcium phosphate ceramic.

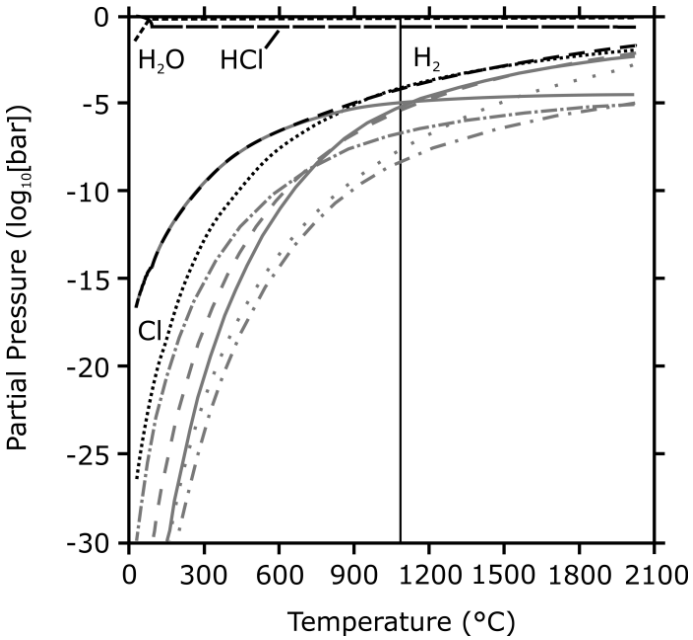

Figure 45: Equilibrium partial pressures of hydrochloric acid (37 %) and derived gaseous species at 1 bar system pressure.

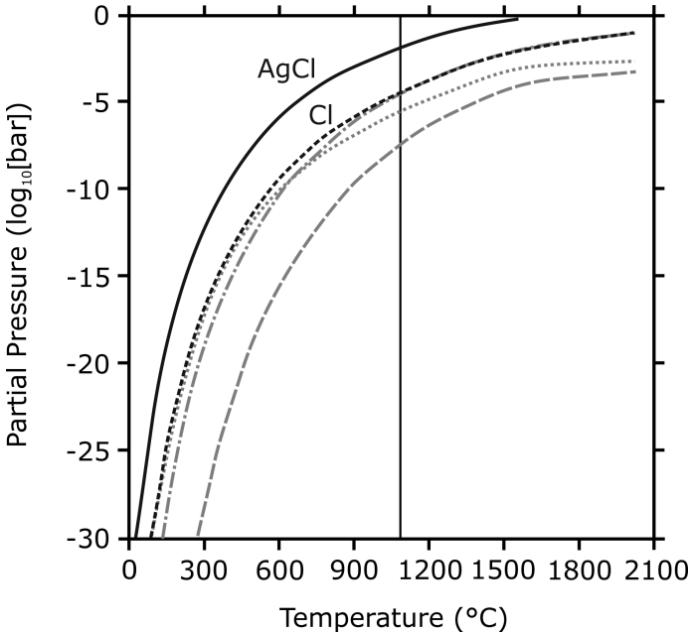

Figure 46: Partial pressures of volatile species in equilibrium with AgCl at 1 bar system pressure.

6.3.3. Equilibrium Partial Pressures for Vapor Transport Sintering Systems

From calculations of the partial pressures of volatile species in the system TCP-H_2O-HCl, it can be derived that Ca^{2+} is mobilized by the formation of $CaCl_2$ (Figure 49c, d). The same reaction was confirmed by calculations for most other sintering agents, with few exceptions: the presence of HI causes the analogous formation of CaI_2, whereas $Ca(OH)_2$ is the most abundant Ca-carrier in equilibrium with HBr and H_2O (c.f. Appendix). In all systems in which Cl-containing sintering agents are involved, Ca^{2+} is transported in conjunction with the halide. This offers a convincing explanation for the formation of Cl-apatite during vapor transport sintering, as determined with XRD (c.f. 4.3.1.1, 5.3.1.2), although it is reportedly less stable than HA at sintering temperature.[11] Phosphorus may be mobilized in its elemental or oxidized state, with PO and PO_2 as the most abundant P-carrying compounds. However, our calculations do not give an indication why the sintering process is retarded in HI atmosphere regarding both densification and coarsening, as observed experimentally. Comparatively high partial pressures of all relevant species are formed (c.f. Appendix, Figure 52b). As discussed in section 4.3.3, the conversion into an apatite phase is effectively impaired by the large ionic radius of I^-.

Although it may be inconvenient with regard to experimental handling, HCl can be introduced into the system as a gas, facilitating vapor transport sintering, as demonstrated by Readey et al. for various metal oxides.[222] The partial pressure of $CaCl_2$ in the system increases along with overall pressure, reaching high values of $>10^{-5}$ for 1 bar and $>10^{-4}$ bar for 50 bar system pressure. Partial pressures for P-carrying $POCl_3$ are slightly lower, at $>10^{-6}$ bar for both 1 and 50 bar at 1100°C.

Similarly, when introducing HCl into the system as hydrochloric acid (37 wt% HCl), ceramic samples are severely attacked when brought in direct contact (Figure 47).[276] However, vapor transport sintering is possible. Increasing partial pressures result for both $CaCl_2$ and the P-carrier, in this case PO_2 or $POCl_3$, if the system pressure rises from 1 bar to 50 bar. The latter case is more realistic, as the presence of supercritical halide acid increases the internal pressure of the reaction vessel to values on the order of 50 bar. However, at 1100°C, partial pressures for $CaCl_2$ are comparatively low at $>10^{-9}$ and $>10^{-7}$ bar, for 1 and 50 bar system pressure, respectively. For the P-carrier, pressures of $>10^{-10}$ and $>10^{-9}$ bar result, respectively, again rising along with total system pressure.

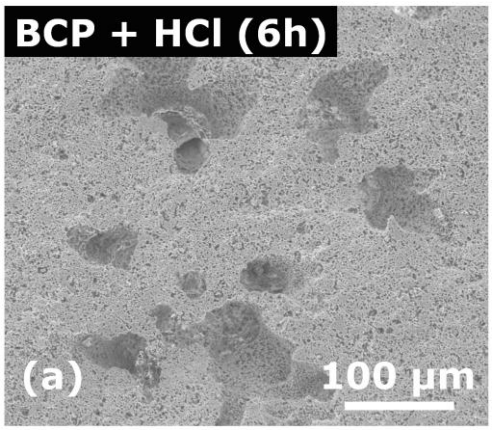

Figure 47: SEM image of a BCP ceramic after sintering at 1100°C for 6 h in hydrochloric acid (37 %). When brought into direct contact, the acid locally dissolves the ceramic, thereby creating macroporous channels.

Assessing the effect of pure H_2O on the sintering system, it is notable that the availability of Ca in the vapor phase is again raised relative to free sintering. Calcium mobilization occurs via the formation of $Ca(OH)_2$ in moderate amounts of $>10^{-14}$ bar, whereas the partial pressure of PO_2 is actually lowered to $>10^{-10}$ bar. Sintering experiments in H_2O-atmosphere were unsuccessful for both HA and β-TCP. With regard to HA, microstructural development was impeded by exaggerated grain growth, as commonly observed for this precursor material (Figure 24). By contrast, no vapor transport-mediated neck growth was observed after 2 h of sintering for β-TCP samples (Figure 48). Considering that XRD analyses showed β-TCP to remain fully stable upon sintering in H_2O (Figure 13b), the crucial role of phase conversions for vapor transport is again confirmed.

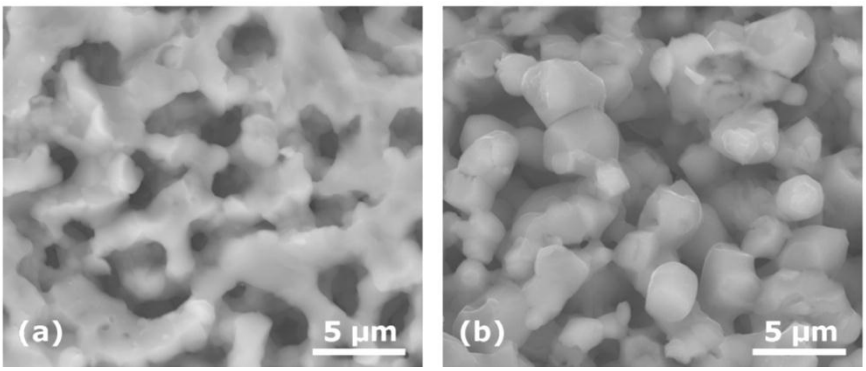

Figure 48: SEM images of β-TCP ceramics sintered at 1100°C for 2 h in (a) hydrochloric acid and (b) water vapor.

Comparing the results obtained for the solid chloride agents[†††] – $MgCl_2$, $CaCl_2$ and AgCl – notable differences in the resulting partial pressures of both $CaCl_2$ and P-carrying PO, PO_2 or $POCl_3$ occur. Particularly favorable conditions for vapor transport are provided by the $MgCl_2$ agent, with>10^{-3} bar $CaCl_2$ and>10^{-7} bar PO at 1 bar system pressure. Thus, $MgCl_2$ has a theoretical capability for Ca mobilization even surpassing that of the highly corrosive HCl gas.[‡‡‡] It is followed by the $CaCl_2$ additive (>10^{-4} bar $CaCl_2$; >10^{-12} bar PO) and by AgCl (>10^{-8} bar $CaCl_2$; >10^{-9} bar PO_2). This is in good agreement with the sintering experiments conducted (c.f. 4.3.2.1, Figure 21c, d). For all solid chlorides, an increase in system pressure from 1 bar to 50 bar has a positive effect on both Ca and P availability in the sintering atmosphere (c.f. Appendix). As confirmed by the sintering experiments, all three additives facilitate vapor transport in significant amounts. Thus, they provide easy-to-handle alternatives to both halide acids and gases.

[†††] Additional diagrams for AgBr and AgI are included in the Appendix.
[‡‡‡] It should be noted that Mg-substitution in β-TCP has a stabilizing effect, thus impeding HA formation (c.f. 5.3.1).

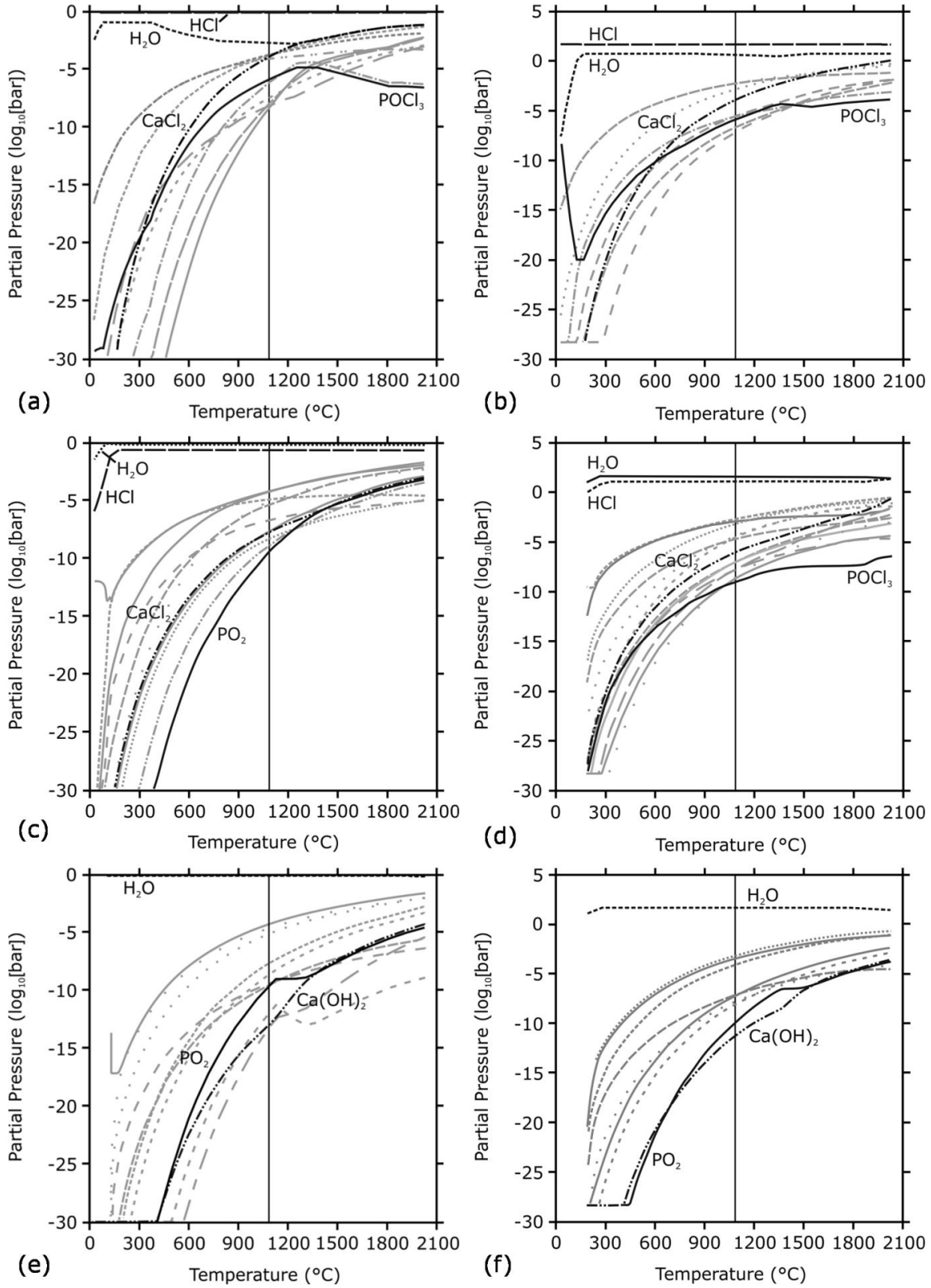

Figure 49: Partial pressures for volatile species in equilibrium with TCP and HCl gas at (a) 1 bar and (b) 50 bar; TCP and hydrochloric acid at (c) 1 bar and (d) 50 bar; TCP and water vapor (e) at 1 bar and (f) 50 bar.

6.4. Chapter Conclusion

The thermodynamic calculations performed provide a theoretical confirmation of the feasibility of vapor transport sintering of β-TCP ceramics in the presence of various halide reagents. Generally, increasing both system temperature and pressure correlates positively with the partial pressures of all relevant compounds in the vapor phase. As the rate-determining species during free sintering, calcium is mobilized in the form of $CaCl_2$, CaI_2 or $Ca(OH)_2$ using HCl gas, halide acids or easy-to-handle solid chlorides.

Although the values for the equilibrium partial pressures calculated would be too low for vapor transport to exert a significant influence on particle coarsening, material transport proceeds, because volatile species are constantly removed from the atmosphere due to Cl- or Br-apatite condensation. Vapor transport sintering of calcium phosphates is driven by this phase conversion from TCP into an apatite phase. Although the presence of H_2O increases Ca availability via the formation of $Ca(OH)_2$, the driving force – in this case, phase conversion into HA – is lacking and no substantial vapor transport takes place. Unfortunately, it is beyond the current scope of the thermodynamical databases available to take account of the apatite phases.

7. Conclusion and Outlook

Vapor transport sintering (VTS) of calcium phosphates was successfully applied to produce porous ceramic scaffolds. For the first time, it could be shown that during sintering the presence of a reactive halide atmosphere enhances vapor transport of calcium phosphates resulting in the simultaneous coarsening of pores and grains for most additives tested, i.e. halide acids (HCl, HBr), as well as solid chlorides ($CaCl_2$, $MgCl_2$ and AgCl). The VTS processing route yields ceramic scaffolds with fully interconnected porosity and facilitates the near-net-shape manufacturing of custom-made ceramics, as the process is nearly shrinkage-free.

Depending on the precursor material, either a substitutional reaction (hydroxyapatite, HA), or a phase conversion (β-tricalcium phosphate, β-TCP) takes place during vapor transport sintering, as summarized for Cl-agent atmospheres in Table 4. However, substitution of Ca^{2+} with Mg^{2+} in precursor β-TCP stabilizes the phase at the expense of HA.

The phase conversion of β-TCP to apatite, triggered by Cl- or Br-containing sintering agents, is crucial for coarsening during VTS. Grain growth proceeds by accretion of newly formed apatite on precursor grains and can be characterized as an Ostwald ripening process. As the phase conversion can be influenced by limiting the Cl^- or Br^- supply, β-TCP and biphasic calcium phosphate (BCP) are both suitable starting materials for the fabrication of biphasic ceramics of adjustable phase composition.

Table 4: Phase conversions occurring during vapor transport sintering in Cl-agent atmospheres.

Precursor	**Process**	**Product**
Hydroxyapatite	Vapor transport sintering	Cl-bearing hydroxyapatite
β-tricalcium phosphate	in Cl-agent atmosphere	Cl-apatite (Ca-deficient)
Mg-tricalcium phosphate	at 1100°C	Mg-tricalcium phosphate

As pore coarsening stagnates after reaching diameters of about 5 µm, VTS needs to be combined with other production methods to meet the requirements for bone graft applications in terms of pore geometry. Thus, the combination of two processing steps – hydrothermal conversion of biogenic carbonate scaffolds, followed by vapor transport sintering in AgCl atmosphere – was investigated further. Whereas hydrothermal conversion is a commercially established process for the fabrication of calcium phosphate scaffolds, sin-

tering in AgCl atmosphere offers additional benefits by causing the condensation of finely dispersed Ag-bearing particles on the scaffolds surface. It could be shown that Ag^+ ions were immediately released upon immersion in aqueous solution which is the precondition for antibacterial action. Bacterial growth inhibition studies with these solutions, as well as zone of inhibition analyses on seeded agar plates, confirmed the antibacterial effect that Ag-modified ceramics have on both Gram-negative (*Pseudomonas aeruginosa*) and Gram-positive strains (*Staphyloccocus aureus*). With regard to the reduction of post-surgical inflammation risks, this novel class of composite material has shown great potential.

Thermodynamic calculations provided a better understanding of material transport through the vapor phase. During free sintering, the equilibrium partial pressures of the relevant volatile species are too low for evaporation and re-condensation to have significant influence on the coarsening process. Due to chemical reactions between β-TCP and the halide agents, otherwise rate-determining calcium is successfully mobilized by the VTS method. As supported by complementary analytical methods, material transport through the vapor phase is further enhanced, because volatile species are constantly removed from the sintering atmosphere due to Cl- or Br-apatite condensation. These findings support our view that vapor transport sintering of calcium phosphates is driven by the phase conversion from β-TCP into apatite. Summing up, the VTS method offers high versatility for the fabrication of porous calcium phosphate scaffolds with fully interconnected porosity. Regarding bone graft applications, it can be combined with other processing techniques to obtain adequate pore geometry.

Future work may address some of the following issues: although the combination of hydrothermal conversion and VTS in AgCl atmosphere was successful in producing an antibacterial composite on the laboratory scale, it seems worthwhile to devise a simplified synthesis route. Clinical studies with a focus on the interaction between the Ag-modified ceramic and bone-forming cells would be the next step towards application. Moreover, VTS may well find applications beyond its intended use for bone replacement. As the flexible crystal structure of apatite minerals allows the incorporation of various toxic heavy metals, highly porous calcium phosphate ceramics might qualify for use in water purification or soil amendment.[277-279]

8. References

[1]S. Mann, "Biomineralization. Principles and concepts in bioinorganic materials chemistry." Oxford University Press, Oxford (2001).

[2]M. Epple, "Biomaterialien und Biomineralisation - Eine Einführung für Naturwissenschaftler, Mediziner und Ingenieure," pp. 162. Teubner, Wiesbaden (2003).

[3]J. Y. Wong and J. D. Bronzino, "Biomaterials." CRC Press, Boca Raton, FL (2007).

[4]J. Enax, O. Prymak, D. Raabe, and M. Epple, "Structure, composition, and mechanical properties of shark teeth," *J. Struct. Biol.*, 178 [3] 290-99 (2012).

[5]S. Weiner, "Organization of extracellularly mineralized tissues - a comparative study of biological crystal growth," *CRC Critical Reviews in Biochemistry*, 20 [4] 365-408 (1986).

[6]R. P. Blakemore, "Magnetotactic bacteria," *Annu. Rev. Microbiol.*, 36 217-38 (1982).

[7]J. D. Currey, "Mechanical properties of mother pearl in tension," *Proceedings of the Royal Society of London Series B-Biological Sciences*, 196 [1125] 443-& (1977).

[8]S. Weiner and H. D. Wagner, "The material bone: Structure mechanical function relations," *Annu. Rev. Mater. Sci.*, 28 271-98 (1998).

[9]J. D. Currey, "The structure and mechanical properties of bone," pp. 3-27 in *Bioceramics and their clinical application,* Vol. 1. Edited by T. Kokubo. CRC Press, Boca Raton, FL, (2008).

[10]R. Z. LeGeros, "Apatites in biological systems," *Prog. Cryst. Growth Charact. Mater.*, 4 [1-2] 1-45 (1981).

[11]J. C. Elliott, "Structure and chemistry of the apatites and other calcium orthophosphates," pp. 389 Vol. 18. Elsevier, Amsterdam (1994).

[12]P. Fratzl, M. Groschner, G. Vogl, H. Plenk, J. Eschberger, N. Fratzl-Zelman, K. Koller, and K. Klaushofer, "Mineral crystals in calcified tissues - a comparative study by SAXS," *J. Bone Miner. Res.*, 7 [3] 329-34 (1992).

[13]E. Wachtel and S. Weiner, "Small-angle X-ray scattering study of dispersed crystals from bone and tendon," *J. Bone Miner. Res.*, 9 [10] 1651-55 (1994).

[14]J. C. Elliott, "Calcium phosphate biominerals," pp. 427-53 in *Phosphates: Geochemical, Geobiological, and Materials Importance,* Vol. 48. *Reviews in Mineralogy & Geochemistry*. Edited by M. J. Kohn, J. Rakovan, and J. M. Hughes. Mineralogical Soc. America, Washington, (2002).

[15]M. J. Arellano-Jimenez, R. Garcia-Garcia, and J. Reyes-Gasga, "Synthesis and hydrolysis of octacalcium phosphate and its characterization by electron microscopy and X-ray diffraction," *J. Phys. Chem. Solids*, 70 [2] 390-95 (2009).

[16]R. Seidel and E. Dingeldein, "Cerabone® - Bovine based spongiosa ceramic," *Materialwiss. Werkstofftech.*, 35 [4] 208-12 (2004).

[17]C. Faucheux, R. Bareille, F. Rouais, J. Amedee, A. Liebendorfer, and M. Dard, "Biocompatibility testing of a bovine hydroxyapatite ceramic material with the use of osteo-progenitor cells isolated from human bone-marrow," *J. Mater. Sci.-Mater. Med.*, 5 [9-10] 635-39 (1994).

[18]C. Schopper, D. Moser, A. Sabbas, G. Lagogiannis, E. Spassova, F. Konig, K. Donath, and R. Ewers, "The fluorohydroxyapatite (FHA) FRIOS® Algipore® is a suitable biomaterial for the reconstruction of severely atrophic human maxillae," *Clinical oral implants research*, 14 [6] 743-9 (2003).

[19]E. C. Shors, "Coralline bone graft substitutes," *Orthop. Clin. North Am.*, 30 [4] 599-613 (1999).

[20]C. Schopper, D. Moser, F. Wanschitz, F. Watzinger, G. Lagogiannis, E. Spassova, and R. Ewers, "Histomorphologic findings on human bone samples six months after bone augmentation of the maxillary sinus with Algipore®," *J. Long-Term Eff. Med. Implants*, 9 [3] 203-13 (1999).

[21]F. Soost, "Biocoral - An alternative bone substitute," *Chirurg*, 67 [11] 1193-96 (1996).

[22]P. Christel, A. Meunier, J. M. Dorlot, J. M. Crolet, J. Witvoet, L. Sedel, and P. Boutin, "Biomechanical compatibility and design of ceramic implants for orthopedic surgery," *Annals of the New York Academy of Sciences*, 523 234-56 (1988).

[23]N.N., "Annual Report 2011/12. "BVMed (2012).

[24]B. Ben-Nissan, A. H. Choi, and R. Cordingley, "Alumina ceramics," pp. 223-42 in *Bioceramics and their clinical applications*. Edited by T. Kokubo. CRC Press, Boca Raton, FL, (2008).

[25]J. M. Lane, A. W. Yasko, E. Tomin, B. J. Cole, S. Waller, M. Browne, T. Turek, and J. Gross, "Bone marrow and recombinant human bone morphogenetic protein-2 in osseous repair," *Clin. Orthop. Rel. Res.* [361] 216-27 (1999).

[26]M. W. Chapman, R. Bucholz, and C. Cornell, "Treatment of acute fractures with a collagen-calcium phosphate graft material - A randomized clinical trial," *J. Bone Joint Surg.-Am. Vol.*, 79A [4] 495-502 (1997).

[27]C. R. Perry, "Bone repair techniques, bone graft, and bone graft substitutes," *Clin. Orthop. Rel. Res.* [360] 71-86 (1999).

[28]L. Gerstenfeld, C. Edgar, S. Kakar, K. Jacobsen, and T. Einhorn, "Osteogenic Growth Factors and Cytokines and Their Role in Bone Repair Engineering of Functional Skeletal Tissues," pp. 17-45 in*,* Vol. 3. *Topics in Bone Biology*. Edited by F. Bronner, M. C. Farach-Carson, and A. G. Mikos. Springer London, (2007).

[29]J. A. Goulet, L. E. Senunas, G. L. DeSilva, and M. Greenfield, "Autogenous iliac crest bone graft - complications and functional assessment," *Clin. Orthop. Rel. Res.* [339] 76-81 (1997).

[30]J. C. Banwart, M. A. Asher, and R. S. Hassanein, "Iliac crest bone-graft harvest donor site morbidity - a statistical evaluation," *Spine*, 20 [9] 1055-60 (1995).

[31]R. W. Hu and H. H. Bohlman, "Fracture at the iliac bone-graft harvest site after fusion of the spine," *Clin. Orthop. Rel. Res.* [309] 208-13 (1994).

[32]J. A. Turner, M. Ersek, L. Herron, J. Haselkorn, D. Kent, M. A. Ciol, and R. Deyo, "Patient outcomes after lumbar spinal fusions," *JAMA-J. Am. Med. Assoc.*, 268 [7] 907-11 (1992).

[33]M. T. Khan, C. Ibbotson, and I. Stockley, "Allograft bone transplantation: a Sheffield experience," *Ann. R. Coll. Surg. Engl.*, 80 [2] 150-53 (1998).

[34]S. W. S. Laurie, L. B. Kaban, J. B. Mulliken, and J. E. Murray, "Donor-site morbidity after harvesting rib and iliac bone," *Plast. Reconstr. Surg.*, 73 [6] 933-38 (1984).

[35]A. J. Aho, J. Eskola, T. Ekfors, I. Manner, T. Kouri, and T. Hollmen, "Immune responses and clinical outcome of massive human osteoarticular allografts," *Clin. Orthop. Rel. Res.* [346] 196-206 (1998).

[36]M. Schieker, C. Heiss, and W. Mutschler, "Bone substitutes," *Unfallchirurg*, 111 [8] 613-19 (2008).

[37]C. J. Damien and J. R. Parsons, "Bone graft and bone-graft substitutes - a review of current technology and applications," *J. Appl. Biomater.*, 2 [3] 187-208 (1991).

[38]L. L. Hench and J. Wilson, "An introduction to bioceramics," pp. 386 in Advanced Series in Ceramics. Edited by M. McLaren and D. E. Niesz. World Scientific, Singapore, New Jersey, London, etc., 1993.

[39]T. Kokubo, "Bioceramics and their clinical applications," pp. 760 in*,* Vol. 1. CRC Press, Boca Raton, FL, 2008.

[40]D. C. Dunand, "Processing of titanium foams," *Adv. Eng. Mater.*, 6 [6] 369-76 (2004).

[41]T. Mattheys, A. Braem, B. Neirinck, O. Van der Biest, and J. Vleugels, "Ti Coatings with Macropores for Improved Implant Fixation Obtained by Electrophoretic Deposition of TiH_2 Stabilized Emulsions," *Adv. Eng. Mater.*, 14 [6] 371-76 (2012).

[42]J. Breme, V. Biehl, and A. Hoffmann, "Tailor-made composites based on titanium for medical devices," *Adv. Eng. Mater.*, 2 [5] 270-75 (2000).

[43]L. L. Hench, "Bioceramics," *J. Am. Ceram. Soc.*, 81 [7] 1705-28 (1998).

[44]E. W. Fritsch and M. Gleitz, "Ceramic femoral head fractures in total hip arthroplasty," *Clin. Orthop. Rel. Res.* [328] 129-36 (1996).

[45]R. Morrell, R. Danzer, I. Milosev, and R. Trebse, "An assessment of in vivo failures of alumina ceramic total hip joint replacements," *J. Eur. Ceram. Soc.*, 32 [12] 3073-84 (2012).

[46]R. Lopes, J. M. Philippeau, N. Passuti, and F. Gouin, "High Rate of Ceramic Sandwich Liner Fracture," *Clin. Orthop. Rel. Res.*, 470 [6] 1705-10 (2012).

[47]A. Viste, J. Chouteau, R. Desmarchelier, and M. H. Fessy, "Fractures of a sandwich ceramic liner at ten year follow-up," *Int. Orthop.*, 36 [5] 955-60 (2012).

[48]S. F. Hulbert, "The use of alumina and zirconia in surgical implants," pp. 25-40 in *An introduction to bioceramics*. *Advanced Series in Ceramics*. Edited by L. L. Hench. World Scientific, Singapore, (1993).

[49]J. Chevalier and L. Gremillard, "Zirconia ceramics," pp. 243-65 in *Bioceramics and their clinical applications*. Edited by T. Kokubo. CRC Press, Boca Raton, FL, (2008).

[50]R. C. Garvie, R. H. Hannink, and R. T. Pascoe, "Ceramic steel?," *Nature*, 258 [5537] 703-04 (1975).

[51]K. Haraguchi, N. Sugano, T. Nishii, H. Miki, K. Oka, and H. Yoshikawa, "Phase transformation of a zirconia ceramic head after total hip arthroplasty," *J. Bone Joint Surg.-Br. Vol.*, 83B [7] 996-1000 (2001).

[52]J. Chevalier, "What future for zirconia as a biomaterial?," *Biomaterials*, 27 [4] 535-43 (2006).

[53]J. Chevalier, L. Gremillard, and S. Deville, "Low-temperature degradation of Zirconia and implications for biomedical implants," pp. 1-32 in *Annual Review of Materials Research,* Vol. 37. Annual Reviews, Palo Alto, (2007).

[54]A. H. De Aza, J. Chevalier, G. Fantozzi, M. Schehl, and R. Torrecillas, "Crack growth resistance of alumina, zirconia and zirconia toughened alumina ceramics for joint prostheses," *Biomaterials*, 23 [3] 937-45 (2002).

[55]J. C. Bokros, "Carbon biomedical devices," *Carbon*, 15 [6] 355-71 (1977).

[56]L. L. Hench and J. Wilson, "Surface-active biomaterials," *Science*, 226 [4675] 630-36 (1984).

[57]L. L. Hench, "The story of Bioglass®," *J. Mater. Sci.-Mater. Med.*, 17 [11] 967-78 (2006).

[58]T. J. Gao, T. K. Tuominen, T. S. Lindholm, B. Kommonen, and T. C. Lindholm, "Morphological and biomechanical difference in healing in segmental tibial defects implanted with Biocoral® or tricalcium phosphate cylinders," *Biomaterials*, 18 [3] 219-23 (1997).

[59]R. A. Yukna and C. N. Yukna, "A 5-year follow-up of 16 patients treated with coralline calcium carbonate (Biocoral™) bone replacement grafts in infrabony defects," *Journal of Clinical Periodontology*, 25 [12] 1036-40 (1998).

[60]B. K. B. Tay, V. V. Patel, and D. S. Bradford, "Calcium sulfate- and calcium phosphate-based bone substitutes - Mimicry of the mineral phase of bone," *Orthop. Clin. North Am.*, 30 [4] 615-23 (1999).

[61]J. L. Ricci, M. J. Weiner, S. Mamidwar, and H. Alexander, "Calcium sulfate," pp. 302-25 in *Bioceramics and their clinical applications*. Edited by T. Kokubo. CRC Press, Boca Raton, FL, (2008).

[62]S. V. Dorozhkin, "Bioceramics of calcium orthophosphates," *Biomaterials*, 31 [7] 1465-85 (2010).

[63]R. Z. LeGeros, "Calcium Phosphate-Based Osteoinductive Materials," *Chem. Rev.*, 108 [11] 4742-53 (2008).

[64]F. H. Albee and H. F. Morrison, "Studies in bone growth - triple calcium phosphate as a stimulus to osteogenesis," *Ann. Surg.*, 71 32-36 (1920).

[65]R. E. Holmes, "Bone regeneration within a coralline hydroxyapatite implant," *Plast. Reconstr. Surg.*, 63 [5] 626-33 (1979).

[66]M. Jarcho, "Calcium-phosphate ceramics as hard tissue prosthetics," *Clin. Orthop. Rel. Res.* [157] 259-78 (1981).

[67]K. de Groot, "Bioceramics of calcium-phosphate. "CRC Press, Boca Raton, FL (1983).

[68]H. Oonishi, H. Oonishi, J. R. Kim, S. C. Kim, L. L. Hench, J. Wilson, E. Tsuji, H. Fujita, H. Oohashi, and K. Oomamiuda, "Clinical application of hydroxyapatite," in *Bioceramics and their clinical applications*. Edited by T. Kokubo. CRC Press, Boca Raton, FL, (2008).

[69]G. Daculsi and R. Z. LeGeros, "Tricalcium phosphate/hydroxyapatite biphasic ceramics," pp. 395-423 in *Bioceramics and their clinical applications*. Edited by T. Kokubo. CRC Press, Boca Raton, FL, (2008).

[70]C. Rey, C. Combes, C. Drouet, and S. Somrani, "Tricalcium phosphate-based ceramics," pp. 326-66 in *Bioceramics and their clinical applications*. Edited by T. Kokubo. CRC Press, Boca Raton, FL, (2008).

[71]J. D. de Bruijn, K. Shankar, H. Yuan, and P. Habibovic, "Osteoinductivity and its evaluation," pp. 199-219 in *Bioceramics and their clinical applications*. Edited by T. Kokubo. CRC Press, Boca Raton, FL, (2008).

[72]T. Nakamura and M. Takemoto, "Osteoconduction and its evaluation," pp. 183-98 in *Bioceramics and their clinical applications*. Edited by T. Kokubo. CRC Press, Boca Raton, FL, (2008).

[73]F. W. Cooke, "Ceramics in orthopedic surgery," *Clin. Orthop. Rel. Res.* [276] 135-46 (1992).

[74]K. de Groot, C. P. A. T. Klein, J. G. C. Wolke, and J. M. A. de Blieck-Hogervorst, "Chemistry of calcium phosphate bioceramics," pp. 3-16 in *Calcium Phosphate and Hydroxylapatite Ceramics*. *CRC Handbook of Bioactive Ceramics*. Edited by T. Yamamuro, L. L. Hench, and J. Wilson. CRC Press, Boca Raton, FL, (1990).

[75]P. Ducheyne, S. Radin, and L. King, "The effect of calcium-phosphate ceramic composition and structure on in-vitro behavior. I. Dissolution," *J. Biomed. Mater. Res.*, 27 [1] 25-34 (1993).

[76]E. D. Eanes and J. L. Meyer, "Maturation of crystalline calcium phosphates in aqueous suspensions at physiologic pH," *Calcified Tissue Research*, 23 [3] 259-69 (1977).

[77]G. H. Nancollas and J. Zhang, "Formation and dissolution mechanisms of calcium phosphates in aqueous systems," pp. 73-81 in *Hydroxyapatite and related materials*. Edited by P. W. Brown and B. Constantz. CRC Press, Boca Raton, FL, (1994).

[78]J. C. Elliott, P. E. Mackie, and R. A. Young, "Monoclinic Hydroxyapatite," *Science*, 180 [4090] 1055-57 (1973).

[79]J. M. Hughes and J. Rakovan, "The crystal structure of apatite, $Ca_5(PO_4)_3(F,OH,Cl)$," pp. 1-12 in *Phosphates: Geochemical, Geobiological, and Materials Importance,* Vol. 48. *Reviews in Mineralogy & Geochemistry*. Edited by M. J. Kohn, J. Rakovan, and J. M. Hughes. Mineralogical Soc. America, Washington, (2002).

[80]Y. Pan and M. E. Fleet, "Compositions of the Apatite-Group Minerals: Substitution Mechanisms and Controlling Factors," *Reviews in Mineralogy and Geochemistry*, 48 [1] 13-49 (2002).

[81]R. Z. LeGeros and J. LeGeros, "Hydroxyapatite," pp. 367-423 in *Bioceramics and their clinical applications*. Edited by T. Kokubo. CRC Press, Boca Raton, FL, (2008).

[82]D. M. Roy and S. K. Linnehan, "Hydroxyapatite formed from coral skeletal carbonate by hydrothermal exchange," *Nature*, 247 [5438] 220-22 (1974).

[83]M. Jarcho, C. H. Bolen, M. B. Thomas, J. Bobick, J. F. Kay, and R. H. Doremus, "Hydroxylapatite synthesis and characterization in dense polycristalline form," *Journal of Materials Science*, 11 [11] 2027-35 (1976).

[84]S. Raynaud, E. Champion, D. Bernache-Assollant, and P. Thomas, "Calcium phosphate apatites with variable Ca/P atomic ratio I. Synthesis, characterisation and thermal stability of powders," *Biomaterials*, 23 [4] 1065-72 (2002).

[85]P. Luo and T. G. Nieh, "Preparing hydroxyapatite powders with controlled morphology," *Biomaterials*, 17 [20] 1959-64 (1996).

[86]S. H. Rhee, "Synthesis of hydroxyapatite via mechanochemical treatment," *Biomaterials*, 23 [4] 1147-52 (2002).

[87]R. R. Rao, H. N. Roopa, and T. S. Kannan, "Solid state synthesis and thermal stability of HAP and HAP - beta-TCP composite ceramic powders," *J. Mater. Sci.-Mater. Med.*, 8 [8] 511-18 (1997).

[88]A. Destainville, E. Champion, D. Bernache-Assollant, and E. Laborde, "Synthesis, characterization and thermal behavior of apatitic tricalcium phosphate," *Mater. Chem. Phys.*, 80 [1] 269-77 (2003).

[89]M. Vallet-Regi, M. Gordo, C. V. Ragel, M. V. Cabanas, and J. San Roman, "Synthesis of ceramic-polymer-drug biocomposites at room temperature," *Solid State Ion.*, 101 887-92 (1997).

[90]X. H. Yang and Z. H. Wang, "Synthesis of biphasic ceramics of hydroxyapatite and beta-tricalcium phosphate with controlled phase content and porosity," *J. Mater. Chem.*, 8 [10] 2233-37 (1998).

[91]S. Raynaud, E. Champion, and D. Bernache-Assollant, "Calcium phosphate apatites with variable Ca/P atomic ratio II. Calcination and sintering," *Biomaterials*, 23 [4] 1073-80 (2002).

[92]A. Ito, T. Hida, Y. Sogo, N. Ichinose, and R. Z. LeGeros, "Solubility of magnesium-containing beta-tricalcium phosphate: Comparison with that of zinc-containing beta-tricalcium phosphate," pp. 239-42 in *Bioceramics 18, Pts 1 and 2,* Vol. 309-311. *Key Engineering Materials*. Edited by T. Nakamura, K. Yamashita, and M. Neo. Trans Tech Publications Ltd, Zurich-Uetikon, (2006).

[93]F. H. Lin, C. J. Liao, K. S. Chen, J. S. Sun, and C. P. Lin, "Petal-like apatite formed on the surface of tricalcium phosphate ceramic after soaking in distilled water," *Biomaterials*, 22 [22] 2981-92 (2001).

[94]A. Ito, M. Otsuka, H. Kawamura, M. Ikeuchi, H. Ohgushi, Y. Sogo, and N. Ichinose, "Zinc-containing tricalcium phosphate and related materials for promoting bone formation," *Curr. Appl. Phys.*, 5 [5] 402-06 (2005).

[95]M. Ikeuchi, A. Ito, Y. Dohi, H. Ohgushi, H. Shimaoka, K. Yonemasu, and T. Tateishi, "Osteogenic differentiation of cultured rat and human bone marrow cells on the surface of zinc-releasing calcium phosphate ceramics," *J. Biomed. Mater. Res. Part A*, 67A [4] 1115-22 (2003).

[96]Y. Fang, D. K. Agrawal, D. M. Roy, and R. Roy, "Microwave sintering of hydroxyapatite ceramics," *J. Mater. Res.*, 9 [1] 180-87 (1994).

[97]S. Raynaud, E. Champion, J. P. Lafon, and D. Bernache-Assollant, "Calcium phosphate apatites with variable Ca/P atomic ratio III. Mechanical properties and degradation in solution of hot pressed ceramics," *Biomaterials*, 23 [4] 1081-89 (2002).

[98]A. J. Ruys, M. Wei, C. C. Sorrell, M. R. Dickson, A. Brandwood, and B. K. Milthorpe, "Sintering effects on the strength of hydroxyapatite," *Biomaterials*, 16 [5] 409-15 (1995).

[99]R. Z. LeGeros and J. P. LeGeros, "Dense Hydroxyapatite," pp. 139-80 in *An introduction to bioceramics*. Edited by L. L. Hench and J. Wilson. World Scientific, Singapore, (1993).

[100]E. C. Shors and R. E. Holmes, "Porous Hydroxyapatite," pp. 181-98 in *Introduction to Bioceramics*. *Advanced Series in Ceramics*. Edited by L. L. Hench and J. Wilson. World Scientific, Singapore, (1993).

[101]Y. C. Fu, M. L. Ho, S. C. Wu, H. S. Hsieh, and C. K. Wang, "Porous bioceramic bead prepared by calcium phosphate with sodium alginate gel and PE powder," *Mater. Sci. Eng. C-Biomimetic Supramol. Syst.*, 28 [7] 1149-58 (2008).

[102]H.-W. Kim, J. C. Knowles, and H.-E. Kim, "Hydroxyapatite porous scaffold engineered with biological polymer hybrid coating for antibiotic Vancomycin release," *Journal of Materials Science: Materials in Medicine*, 16 [3] 189-95 (2005).

[103]B. J. Melde and A. Stein, "Periodic macroporous hydroxyapatite-containing calcium phosphates," *Chem. Mat.*, 14 [8] 3326-31 (2002).

[104]Q.-Z. Chen, O. Bretcanu, and A. R. Boccaccini, "Inorganic and composite bioactive scaffolds for bone tissue engineering," pp. 3-44 in *Biomaterials fabrication and processing*. Edited by P. K. Chu and X. Liu. CRC Press, Boca Raton, FL, (2008).

[105]C. Kraiwattanapong, S. D. Boden, J. Louis-Ugbo, E. Attallah, B. Barnes, and W. C. Hutton, "Comparison of Healos/bone marrow to INFUSE(rhBMP-2/ACS) with a collagen-ceramic sponge bulking agent as graft substitutes for lumbar spine fusion," *Spine*, 30 [9] 1001-07 (2005).

[106]D. Neen, D. Noyes, M. Shaw, S. Gwilym, N. Fairlie, and N. Birch, "Healos and bone marrow aspirate used for lumbar spine fusion - A case controlled study comparing Healos with autograft," *Spine*, 31 [18] E636-E40 (2006).

[107]L. Le Guehennec, P. Layrolle, and G. Daculsi, "A review of bioceramics and fibrin sealant," *European cells & materials*, 8 1-10; discussion 10-1 (2004).

[108]M. Nishikawa, A. Myoui, H. Ohgushi, M. Ikeuchi, N. Tamai, and H. Yoshikawa, "Bone tissue engineering using novel interconnected porous hydroxyapatite ceramics combined with marrow mesenchymal cells: Quantitative and three-dimensional image analysis," *Cell Transplant.*, 13 [4] 367-76 (2004).

[109]H. Ohgushi, "Tissue engineering using bioceramics," pp. 718-36 in *Bioceramics and their clinical applications*. Edited by T. Kokubo. CRC Press, Boca Raton, FL, (2008).

[110]P. Kasten, J. Vogel, R. Luginbuhl, P. Niemeyer, M. Tonak, H. Lorenz, L. Helbig, S. Weiss, J. Fellenberg, A. Leo, H. G. Simank, and W. Richter, "Ectopic bone formation associated with mesenchymal stem cells in a resorbable calcium deficient hydroxyapatite carrier," *Biomaterials*, 26 [29] 5879-89 (2005).

[111]P. Niemeyer, U. Krause, J. Fellenberg, P. Kasten, A. Seckinger, A. D. Ho, and H. G. Simank, "Evaluation of mineralized collagen and alpha-tricalcium phosphate as scaffolds for tissue engineering of bone using human mesenchymal stem cells," *Cells Tissues Organs*, 177 [2] 68-78 (2004).

[112]J. A. Dong, T. Uemura, Y. Shirasaki, and T. Tateishi, "Promotion of bone formation using highly pure porous beta-TCP combined with bone marrow-derived osteoprogenitor cells," *Biomaterials*, 23 [23] 4493-502 (2002).

[113]D. Tadic, F. Beckmann, K. Schwarz, and M. Epple, "A novel method to produce hydroxyapatite objects with interconnecting porosity that avoids sintering," *Biomaterials*, 25 [16] 3335-40 (2004).

[114]M. Kawata, H. Uchida, K. Itatani, I. Okada, S. Koda, and M. Aizawa, "Development of porous ceramics with well-controlled porosities and pore sizes from apatite fibers and their evaluations," *J. Mater. Sci.-Mater. Med.*, 15 [7] 817-23 (2004).

[115]R. M. Pilliar, M. J. Filiaggi, J. D. Wells, M. D. Grynpas, and R. A. Kandel, "Porous calcium polyphosphate scaffolds for bone substitute applications - in vitro characterization," *Biomaterials*, 22 [9] 963-72 (2001).

[116]A. Tampieri, G. Celotti, S. Sprio, A. Delcogliano, and S. Franzese, "Porosity-graded hydroxyapatite ceramics to replace natural bone," *Biomaterials*, 22 [11] 1365-70 (2001).

[117]S.-H. Kwon, Y.-K. Jun, S.-H. Hong, I.-S. Lee, H.-E. Kim, and Y. Y. Won, "Calcium Phosphate Bioceramics with Various Porosities and Dissolution Rates," *J. Am. Ceram. Soc.*, 85 [12] 3129-31 (2002).

[118]N. Tamai, A. Myoui, T. Tomita, T. Nakase, J. Tanaka, T. Ochi, and H. Yoshikawa, "Novel hydroxyapatite ceramics with an interconnective porous structure exhibit superior osteoconduction in vivo," *J. Biomed. Mater. Res.*, 59 [1] 110-17 (2002).

[119]P. Sepulveda, "Gelcasting foams for porous ceramics," *Am. Ceram. Soc. Bull.*, 76 [10] 61-65 (1997).

[120]S. Deville, E. Saiz, and A. P. Tomsia, "Freeze casting of hydroxyapatite scaffolds for bone tissue engineering," *Biomaterials*, 27 [32] 5480-89 (2006).

[121]T. M. G. Chu, D. G. Orton, S. J. Hollister, S. E. Feinberg, and J. W. Halloran, "Mechanical and in vivo performance of hydroxyapatite implants with controlled architectures," *Biomaterials*, 23 [5] 1283-93 (2002).

[122]S. C. G. Leeuwenburgh, J. G. C. Wolke, J. A. Jansen, and K. De Groot, "Calcium phosphate coatings," pp. 464-84 in *Bioceramics and their clinical applications*. Edited by T. Kokubo. CRC Press, Boca Raton, FL, (2008).

[123]L. L. Hench and J. Wilson, "Introduction," pp. 1-24 in *An introduction to bioceramics*. Edited by L. L. Hench and J. Wilson. World Scientific, Singapore, New Jersey, London, etc., (1993).

[124]F. Gouin, J. Delecrin, N. Passuti, S. Touchais, P. Poirier, and J. V. Bainvel, "Biphasic macroporous calcium-phosphate ceramic bone substitute for filling bone defects - a report of 23 cases," *Rev. Chir. Orthop. Reparatrice Appareil Moteur*, 81 [1] 59-65 (1995).

[125]K. D. Johnson, K. E. Frierson, T. S. Keller, C. Cook, R. Scheinberg, J. Zerwekh, L. Meyers, and M. F. Sciadini, "Porous ceramics as bone graft substitutes in long bone defects: A biomechanical, histological, and radiographic analysis," *J. Orthop. Res.*, 14 [3] 351-69 (1996).

[126]R. W. Bucholz, "Nonallograft osteoconductive bone graft substitutes," *Clin. Orthop. Rel. Res.* [395] 44-52 (2002).

[127]M. Itokazu, T. Matsunaga, M. Ishii, H. Kusakabe, and Y. Wyni, "Use of arthroscopy and interporous hydroxyapatite as a bone graft substitute in tibial plateau fractures," *Arch. Orthop. Trauma Surg.*, 115 [1] 45-48 (1996).

[128]F. Rahimi, B. T. Maurer, and M. G. Enzweiler, "Coralline hydroxyapatite: a bone graft alternative in foot and ankle surgery," *The Journal of foot and ankle surgery : official publication of the American College of Foot and Ankle Surgeons*, 36 [3] 192-203; discussion 55-6 (1997).

[129]B. F. Shahgaldi, "Coral graft restoration of osteochondral defects," *Biomaterials*, 19 [1-3] 205-13 (1998).

[130]S. D. Boden, G. J. Martin, M. Morone, J. L. Ugbo, L. Titus, and W. C. Hutton, "The use of coralline hydroxyapatite with bone marrow, autogenous bone graft, or osteoinductive bone protein extract for posterolateral lumbar spine fusion," *Spine*, 24 [4] 320-27 (1999).

[131]K. A. Hing, S. M. Best, K. E. Tanner, W. Bonfield, and P. A. Revell, "Quantification of bone ingrowth within bone-derived porous hydroxyapatite implants of varying density," *J. Mater. Sci.-Mater. Med.*, 10 [10-11] 663-70 (1999).

[132]S. F. Hulbert, F. W. Cooke, J. J. Klawitter, R. B. Leonard, B. W. Sauer, D. D. Moyle, and H. B. Skinner, "Attachment of prostheses to musculoskeletal system by tissue ingrowth and mechanical interlocking," *J. Biomed. Mater. Res.*, 7 [3] 1-23 (1973).

[133]J. J. Klawitter and S. F. Hulbert, "Application of porous ceramics for the attachment of load bearing internal orthopedic applications," *J. Biomed. Mater. Res.*, 5 [6] 161-229 (1971).

[134]Y. Kuboki, H. Takita, D. Kobayashi, E. Tsuruga, M. Inoue, M. Murata, N. Nagai, Y. Dohi, and H. Ohgushi, "BMP-induced osteogenesis on the surface of hydroxyapatite with geometrically feasible and nonfeasible structures: Topology of osteogenesis," *J. Biomed. Mater. Res.*, 39 [2] 190-99 (1998).

[135]M. Okamoto, Y. Dohi, H. Ohgushi, H. Shimaoka, M. Ikeuchi, A. Matsushima, K. Yonemasu, and H. Hosoi, "Influence of the porosity of hydroxyapatite ceramics on in vitro and in vivo bone formation by cultured rat bone marrow stromal cells," *Journal of Materials Science: Materials in Medicine*, 17 [4] 327-36 (2006).

[136]E. Tsuruga, H. Takita, H. Itoh, Y. Wakisaka, and Y. Kuboki, "Pore size of porous hydroxyapatite as the cell-substratum controls BMP-induced osteogenesis," *J. Biochem.*, 121 [2] 317-24 (1997).

[137]P. Kasten, I. Beyen, P. Niemeyer, R. Luginbuhl, M. Bohner, and W. Richter, "Porosity and pore size of beta-tricalcium phosphate scaffold can influence protein production and osteogenic differentiation of human mesenchymal stem cells: An in vitro and in vivo study," *Acta Biomater.*, 4 [6] 1904-15 (2008).

[138]P. Habibovic, H. P. Yuan, C. M. van der Valk, G. Meijer, C. A. van Blitterswijk, and K. de Groot, "3D microenvironment as essential element for osteoinduction by biomaterials," *Biomaterials*, 26 [17] 3565-75 (2005).

[139]A. H. Reddi, "Morphogenesis and Tissue Engineering of Bone and Cartilage: Inductive Signals, Stem Cells, and Biomimetic Biomaterials," *Tissue Engineering*, 6 [4] 351-59 (2000).

[140]C. Klein, A. A. Driessen, K. de Groot, and A. Vandenhooff, "Biodegradation behavior of various calcium-phosphate materials in bone tissue," *J. Biomed. Mater. Res.*, 17 [5] 769-84 (1983).

[141]C. T. Begley, M. J. Doherty, R. A. B. Mollan, and D. J. Wilson, "Comparative study of the osteoinductive properties of bioceramic, coral and processed bone-graft substitutes," *Biomaterials*, 16 [15] 1181-85 (1995).

[142]D. Chappard, A. Zhioua, F. Grizon, M. F. Basle, and A. Rebel, "Biomaterials for bone filling: comparisons between autograft, hydroxyapatite and one highly purified bovine xenograft," *Bulletin de l'Association des anatomistes*, 77 [239] 59-65 (1993).

[143]S. E. Emery, D. A. Fuller, and S. Stevenson, "Ceramic anterior spinal fusion - Biologic and biomechanical comparison in a canine model," *Spine*, 21 [23] 2713-19 (1996).

[144]J. M. Rueger, W. Linhard, and D. Sommerfeldt, "Biological reactions to calcium phosphate ceramic implants - results of animal experiments," *Orthopade*, 27 [2] 89-95 (1998).

[145]M. Yamada, M. Shiota, Y. Yamashita, and S. Kasugai, "Histological and histomorphometrical comparative study of the degradation and osteoconductive characteristics of alpha- and beta-tricalcium phosphate in block grafts," *J. Biomed. Mater. Res. Part B*, 82B [1] 139-48 (2007).

[146]H. Monma, S. Ueno, and T. Kanazawa, "Properties of hydroxyapatite prepared by the hydrolysis of tricalcium phosphate," *J. Chem. Technol. Biotechnol.*, 31 [1] 15-24 (1981).

[147]R. L. Xin, Y. Leng, J. Y. Chen, and Q. Y. Zhang, "A comparative study of calcium phosphate formation on bioceramics in vitro and in vivo," *Biomaterials*, 26 [33] 6477-86 (2005).

[148]S. Somrani, C. Rey, and M. Jemal, "Thermal evolution of amorphous tricalcium phosphate," *J. Mater. Chem.*, 13 [4] 888-92 (2003).

[149]J. C. Le Huec, E. Lesprit, C. Delavigne, D. Clement, D. Chauveaux, and A. Le Rebeller, "Tri-calcium phosphate ceramics and allografts as bone substitutes for spinal fusion in idiopathic scoliosis: comparative clinical results at four years," *Acta orthopaedica Belgica*, 63 [3] 202-11 (1997).

[150]F. Monchau, A. Lefevre, M. Descamps, A. Belquin-myrdycz, P. Laffargue, and H. F. Hildebrand, "In vitro studies of human and rat osteoclast activity on hydroxyapatite, beta-tricalcium phosphate, calcium carbonate," *Biomol. Eng.*, 19 [2-6] 143-52 (2002).

[151]E. B. Nery, K. L. Lynch, W. M. Hirthe, and K. H. Mueller, "Bioceramic implants in surgically produced infrabony defects," *J. Periodont.*, 46 [6] 328-47 (1975).

[152]G. Daculsi, O. Laboux, O. Malard, and P. Weiss, "Current state of the art of biphasic calcium phosphate bioceramics," *Journal of Materials Science: Materials in Medicine*, 14 [3] 195-200 (2003).

[153]G. Daculsi, R. Z. Legeros, E. Nery, K. Lynch, and B. Kerebel, "Transformation of biphasic calcium phosphate ceramics in vivo: Ultrastructural and physicochemical characterization," *J. Biomed. Mater. Res.*, 23 [8] 883-94 (1989).

[154]G. Daculsi, R. Z. Legeros, and C. Deudon, "Scanning and transmission electron-microscopy, and electron-probe analysis of the interface between implants and host bone - osseo-coalescence versus osseointegration," *Scanning Microsc.*, 4 [2] 309-14 (1990).

[155]G. Daculsi, R. Z. Legeros, M. Heughebaert, and I. Barbieux, "Formation of carbonate-apatite crystals after implantation of calcium-phosphate ceramics," *Calcif. Tissue Int.*, 46 [1] 20-27 (1990).

[156]E. B. Nery, R. Z. Legeros, K. L. Lynch, and K. Lee, "Tissue-response to biphasic calcium-phosphate ceramic with different ratios of HA/beta-TCP in periodontal osseous defects," *J. Periodont.*, 63 [9] 729-35 (1992).

[157]R. Z. LeGeros, S. Lin, R. Rohanizadeh, D. Mijares, and J. P. LeGeros, "Biphasic calcium phosphate bioceramics: preparation, properties and applications," *Journal of Materials Science: Materials in Medicine*, 14 [3] 201-09 (2003).

[158]H. Yamasaki and H. Sakai, "Osteogenic response to porous hydroxyapatite ceramics under the skin of dogs," *Biomaterials*, 13 [5] 308-12 (1992).

[159]R. Z. LeGeros, "Properties of osteoconductive biomaterials: calcium phosphates," *Clin. Orthop. Rel. Res.* [395] 81-98 (2002).

[160]C. Klein, K. de Groot, W. Q. Chen, Y. B. Li, and X. D. Zhang, "Osseous substance formation induced in porous calcium-phosphate ceramics in soft-tissues," *Biomaterials*, 15 [1] 31-34 (1994).

[161]E. M. Erbe, J. G. Marx, T. D. Clineff, and L. D. Bellincampi, "Potential of an ultraporous beta-tricalcium phosphate synthetic cancellous bone void filler and bone marrow aspirate composite graft," *Eur. Spine J.*, 10 S141-S46 (2001).

[162]P. Habibovic, M. C. Kruyt, M. V. Juhl, S. Clyens, R. Martinetti, L. Dolcini, N. Theilgaard, and C. A. van Blitterswijk, "Comparative in vivo study of six hydroxyapatite-based bone graft substitutes," *J. Orthop. Res.*, 26 [10] 1363-70 (2008).

[163]A. J. Wagoner Johnson and B. A. Herschler, "A review of the mechanical behavior of CaP and CaP/polymer composites for applications in bone replacement and repair," *Acta Biomater.*, 7 [1] 16-30 (2011).

[164]Z. Z. Zyman, I. G. Ivanov, and V. I. Glushko, "Possibilities for strengthening hydroxyapatite ceramics," *J. Biomed. Mater. Res.*, 46 [1] 73-79 (1999).

[165]J. M. Bouler, M. Trecant, J. Delecrin, J. Royer, N. Passuti, and G. Daculsi, "Macroporous biphasic calcium phosphate ceramics: Influence of five synthesis parameters on compressive strength," *J. Biomed. Mater. Res.*, 32 [4] 603-09 (1996).

[166]S. V. Dorozhkin, "Calcium orthophosphate-based biocomposites and hybrid biomaterials," *Journal of Materials Science*, 44 [9] 2343-87 (2009).

[167]D. S. Metsger, M. R. Rieger, and D. W. Foreman, "Mechanical properties of sintered hydroxyapatite and tricalcium phosphate ceramic," *J. Mater. Sci.-Mater. Med.*, 10 [1] 9-17 (1999).

[168]L. C. Palmer, C. J. Newcomb, S. R. Kaltz, E. D. Spoerke, and S. I. Stupp, "Biomimetic Systems for Hydroxyapatite Mineralization Inspired By Bone and Enamel," *Chem. Rev.*, 108 [11] 4754-83 (2008).

[169]Y. M. Kong, S. Kim, H. E. Kim, and I. S. Lee, "Reinforcement of hydroxyapatite bioceramic by addition of ZrO_2 coated with Al_2O_3," *J. Am. Ceram. Soc.*, 82 [11] 2963-68 (1999).

[170]Z. E. Erkmen, Y. Genc, and F. N. Oktar, "Microstructural and mechanical properties of hydroxyapatite-zirconia composites," *J. Am. Ceram. Soc.*, 90 [9] 2885-92 (2007).

[171]Y. Nayak, R. P. Rana, S. K. Pratihar, and S. Bhattacharyya, "Pressureless sintering of dense hydroxyapatite-zirconia composites," *J. Mater. Sci.-Mater. Med.*, 19 [6] 2437-44 (2008).

[172]I. Mobasherpour, M. S. Hashjin, S. S. R. Toosi, and R. D. Kamachali, "Effect of the addition ZrO_2-Al_2O_3 on nanocrystalline hydroxyapatite bending strength and fracture toughness," *Ceram. Int.*, 35 [4] 1569-74 (2009).

[173]C. L. Chu, X. Y. Xue, J. C. Zhu, and Z. D. Yin, "Fabrication and characterization of titanium-matrix composite with 20 vol% hydroxyapatite for use as heavy load-bearing hard tissue replacement," *J. Mater. Sci.-Mater. Med.*, 17 [3] 245-51 (2006).

[174]N. Nomura, K. Sakamoto, K. Takahashi, S. Kato, Y. Abe, H. Doi, Y. Tsutsumi, M. Kobayashi, E. Kobayashi, W. J. Kim, K. H. Kim, and T. Hanawa, "Fabrication and Mechanical Properties of Porous Ti/HA Composites for Bone Fixation Devices," *Mater. Trans.*, 51 [8] 1449-54 (2010).

[175]D. K. Pattanayak, B. T. Rao, and T. R. R. Mohan, "Calcium phosphate bioceramics and bioceramic composites," *J. Sol-Gel Sci. Technol.*, 59 [3] 432-47 (2011).

[176]A. Rapacz-Kmita, A. Slosarczyk, and Z. Paszkiewicz, "Mechanical properties of HAp-ZrO_2 composites," *J. Eur. Ceram. Soc.*, 26 [8] 1481-88 (2006).

[177]K. Ioku, S. Somiya, and M. Yoshimura, "Hydroxyapatite ceramics with tetragonal zirconia particles dispersion prepared by HIP postsintering," *J. Ceram. Soc. Jpn.*, 99 [3] 196-203 (1991).

[178]G. Dewith and A. J. Corbijn, "Metal fiber reinforced hydroxy-apatite ceramics," *Journal of Materials Science*, 24 [9] 3411-15 (1989).

[179]T. K. Chaki and P. E. Wang, "Densification and strengthening of silver-reinforced hydroxyapatite-matrix composite prepared by sintering," *J. Mater. Sci.-Mater. Med.*, 5 [8] 533-42 (1994).

[180]D. G. Guo, K. W. Xu, and Y. Han, "The in situ synthesis of biphasic calcium phosphate scaffolds with controllable compositions, structures, and adjustable properties," *J. Biomed. Mater. Res. Part A*, 88A [1] 43-52 (2009).

[181]T. Shiota, M. Shibata, K. Yasuda, and Y. Matsuo, "Influence of beta-tricalcium phosphate dispersion on mechanical properties of hydroxyapatite ceramics," *J. Ceram. Soc. Jpn.*, 116 [1357] 1002-05 (2008).

[182]S. F. Hulbert, S. J. Morrison, and J. J. Klawitter, "Tissue reaction to 3 ceramics of porous and non-porous structures," *J. Biomed. Mater. Res.*, 6 [5] 347-74 (1972).

[183]V. Alt, T. Bechert, P. Steinrucke, M. Wagener, P. Seidel, E. Dingeldein, E. Domann, and R. Schnettler, "An in vitro assessment of the antibacterial properties and cytotoxicity of nanoparticulate silver bone cement," *Biomaterials*, 25 [18] 4383-91 (2004).

[184]J. K. Liu, X. H. Yang, and X. G. Tian, "Preparation of silver/hydroxyapatite nanocomposite spheres," *Powder Technol.*, 184 [1] 21-24 (2008).

[185]M. Diaz, F. Barba, M. Miranda, F. Guitian, R. Torrecillas, and J. S. Moya, "Synthesis and Antimicrobial Activity of a Silver-Hydroxyapatite Nanocomposite," *J. Nanomater.* (2009).

[186]T. N. Kim, Q. L. Feng, J. O. Kim, J. Wu, H. Wang, G. Q. Chen, and F. Z. Cui, "Antimicrobial effects of metal ions (Ag^+, Cu^{2+}, Zn^{2+}) in hydroxyapatite," *J. Mater. Sci.-Mater. Med.*, 9 [3] 129-34 (1998).

[187]J. J. Buckley, A. F. Lee, L. Olivi, and K. Wilson, "Hydroxyapatite supported antibacterial Ag_3PO_4 nanoparticles," *J. Mater. Chem.*, 20 [37] 8056-63 (2010).

[188]Y. Ando, H. Miyamoto, I. Noda, N. Sakurai, T. Akiyama, Y. Yonekura, T. Shimazaki, M. Miyazaki, M. Mawatari, and T. Hotokebuchi, "Calcium phosphate coating containing silver shows high antibacterial activity and low cytotoxicity and inhibits bacterial adhesion," *Materials Science and Engineering: C*, 30 [1] 175-80 (2010).

[189]M. Shirkhanzadeh, M. Azadegan, and G. Q. Liu, "Bioactive delivery systems for the slow-release of antibiotics: Incorporation of Ag^+ ions into micro-porous hydroxyapatite coatings," *Mater. Lett.*, 24 [1-3] 7-12 (1995).

[190]Q. L. Feng, T. N. Kim, J. Wu, E. S. Park, J. O. Kim, D. Y. Lim, and F. Z. Cui, "Antibacterial effects of Ag-HAp thin films on alumina substrates," *Thin Solid Films*, 335 [1-2] 214-19 (1998).

[191]Y. K. Chen, X. B. Zheng, Y. T. Xie, C. X. Ding, H. J. Ruan, and C. Y. Fan, "Anti-bacterial and cytotoxic properties of plasma sprayed silver-containing HA coatings," *J. Mater. Sci.-Mater. Med.*, 19 [12] 3603-09 (2008).

[192]X. A. Bai, K. More, C. M. Rouleau, and A. Rabiei, "Functionally graded hydroxyapatite coatings doped with antibacterial components," *Acta Biomater.*, 6 [6] 2264-73 (2010).

[193]S. Nath, S. Kalmodia, and B. Basu, "Densification, phase stability and in vitro biocompatibility property of hydroxyapatite-10 wt% silver composites," *J. Mater. Sci.-Mater. Med.*, 21 [4] 1273-87 (2010).

[194]N. Rameshbabu, T. S. S. Kumar, T. G. Prabhakar, V. S. Sastry, K. Murty, and K. P. Rao, "Antibacterial nanosized silver substituted hydroxyapatite: Synthesis and characterization," *J. Biomed. Mater. Res. Part A*, 80A [3] 581-91 (2007).

[195]N. Matsumoto, K. Sato, K. Yoshida, K. Hashimoto, and Y. Toda, "Preparation and characterization of beta-tricalcium phosphate co-doped with monovalent and divalent antibacterial metal ions," *Acta Biomater.*, 5 [8] 3157-64 (2009).

[196]L. C. Gerber, D. Mohn, G. Fortunato, M. Astasov-Frauenhoffer, T. Imfeld, T. Waltimo, M. Zehnder, and W. J. Stark, "Incorporation of reactive silver-tricalcium phosphate nanoparticles into polyamide 6 allows preparation of self-disinfecting fibers," *Polymer Engineering & Science*, 51 [1] 71-77 (2011).

[197]I. Manjubala, M. Sivakumar, T. S. S. Kumar, and K. P. Rao, "Synthesis and characterization of functional gradient materials using Indian corals," *J. Mater. Sci.-Mater. Med.*, 11 [11] 705-09 (2000).

[198]I. Manjubala and T. S. S. Kumar, "Effect of TiO_2-Ag_2O additives on the formation of calcium phosphate based functionally graded bioceramics," *Biomaterials*, 21 [19] 1995-2002 (2000).

[199]Q. L. Feng, J. Wu, G. Q. Chen, F. Z. Cui, T. N. Kim, and J. O. Kim, "A mechanistic study of the antibacterial effect of silver ions on Escherichia coli and Staphylococcus aureus," *J. Biomed. Mater. Res.*, 52 [4] 662-68 (2000).

[200]A. B. G. Lansdown, "Silver in health care: antimicrobial effects and safety in use," *Current problems in dermatology*, 33 17-34 (2006).

[201]M. Yamanaka, K. Hara, and J. Kudo, "Bactericidal actions of a silver ion solution on Escherichia coli, studied by energy-filtering transmission electron microscopy and proteomic analysis," *Appl. Environ. Microbiol.*, 71 [11] 7589-93 (2005).

[202]C. L. Fox and S. M. Modak, "Mechanism of silver sulfadiazine action on burn wound infections," *Antimicrob. Agents Chemother.*, 5 [6] 582-88 (1974).

[203]O. Choi, K. K. Deng, N. J. Kim, L. Ross, R. Y. Surampalli, and Z. Q. Hu, "The inhibitory effects of silver nanoparticles, silver ions, and silver chloride colloids on microbial growth," *Water Res.*, 42 [12] 3066-74 (2008).

[204]J. S. Kim, E. Kuk, K. N. Yu, J. H. Kim, S. J. Park, H. J. Lee, S. H. Kim, Y. K. Park, Y. H. Park, C. Y. Hwang, Y. K. Kim, Y. S. Lee, D. H. Jeong, and M. H. Cho, "Antimicrobial effects of silver nanoparticles," *Nanomed.-Nanotechnol. Biol. Med.*, 3 [1] 95-101 (2007).

[205]P. W. Atkins, "Physical Chemistry,"pp. 1106. Oxford University Press, Oxford (1994).

[206]A. Putnis, "Introduction to Mineral Sciences."Cambridge University Press, Cambridge (1992).

[207]D. A. Skoog, F. J. Holler, and T. A. Nieman, "Principles of Instrumental Analysis."Brooks Cole (1997).

[208]B. Schrader, "General survey of vibrational spectroscopy," pp. 7-64 in *Infrared and Raman Spectroscopy. Methods and Applications*. Edited by B. Schrader. VCH, Weinheim, (1995).

[209]N.N., "Rocksolid™ manual, Bruker,"Karlsruhe, Germany.

[210]P. Hahn-Weinheimer, A. Hirner, and K. Weber-Diefenbach, "Grundlagen und praktische Anwendung der Röntgenfluoreszenzanalyse (RFA),"pp. 253. Vieweg, Braunschweig (1984).

[211]H. Mommsen, "Archäometrie: Neuere naturwissenschaftliche Methoden und Erfolge in der Archäologie."Teubner Verlag, Wiesbaden (1986).

[212]S. L. Flegler, J. W. Heckman, and K. L. Klomparens, "Scanning and Transmission Electron Microscopy."Oxford University Press, Oxford (1993).

[213]J. Goldstein, D. Newbury, D. Joy, C. Lyman, P. Echlin, E. Lifshin, L. Sawyer, and J. Michael, "Scanning electron microscopy and X-ray microanalysis,"pp. 690. Springer, Heidelberg, New York (2003).

[214]R. D. Deslattes, E. G. Kessler, P. Indelicato, L. de Billy, E. Lindroth, and J. Anton, "X-ray transition energies: new approach to a comprehensive evaluation," *Rev. Mod. Phys.*, 75 [1] 35-99 (2003).

[215]C. E. Mortimer, "Chemistry."Wadsworth Publishing, Belmont, CA (1986).

[216]N.N., "Oxford Dictionary of Chemistry,"pp. 602. Oxford University Press, Oxford (2004).

[217]W. D. Kingery, H. K. Bowen, and D. R. Uhlmann, "Introduction to ceramics,"pp. 1056. John Wiley & Sons (1976).

[218]M. N. Rahaman, "Sintering of Ceramics. "CRC Press, Boca Raton, FL (2008).

[219]H. Salmang and H. Scholze, "Keramik, "pp. 1148. Springer, Luxemburg, Berlin (2007).

[220]J. L. Shi, Y. Deguchi, and Y. Sakabe, "Relation between grain growth, densification and surface diffusion in solid state sintering - a direct observation," *Journal of Materials Science*, 40 [21] 5711-19 (2005).

[221]T. Quadir and D. W. Readey, "Microstructure development of zinc-oxide in hydrogen," *J. Am. Ceram. Soc.*, 72 [2] 297-302 (1989).

[222]D. W. Readey, "Vapor transport and sintering," pp. 86-110 in *Sintering of advanced ceramics*. *Ceramic Transactions*. Edited by C. A. Handwerker, J. E. Blendell, and W. A. Kaysser. The American Ceramic Society, (1990).

[223]M. J. Readey and D. W. Readey, "Sintering of ZrO_2 in HCl atmospheres," *J. Am. Ceram. Soc.*, 69 [7] 580-82 (1986).

[224]M. J. Readey and D. W. Readey, "Sintering TiO_2 in HCl atmospheres," *J. Am. Ceram. Soc.*, 70 [12] C358-C61 (1987).

[225]Y. K. Jun, S. H. Hong, and Y. M. Kong, "Effect of co-precipitation on the low-temperature sintering of biphasic calcium phosphate," *J. Am. Ceram. Soc.*, 89 [7] 2295-97 (2006).

[226]O. Gauthier, J. M. Bouler, E. Aguado, R. Z. Legeros, P. Pilet, and G. Daculsi, "Elaboration conditions influence physicochemical properties and in vivo bioactivity of macroporous biphasic calcium phosphate ceramics," *J. Mater. Sci.-Mater. Med.*, 10 [4] 199-204 (1999).

[227]K. Yanagisawa, J. C. Rendon-Angeles, N. Ishizawa, and S. Oishi, "Topotaxial replacement of chlorapatite by hydroxyapatite during hydrothermal ion exchange," *Am. Miner.*, 84 [11-12] 1861-69 (1999).

[228]G. C. Maiti and F. Freund, "Incorporation of chlorine into hydroxy-apatite," *Journal of Inorganic & Nuclear Chemistry*, 43 [11] 2633-37 (1981).

[229]J. M. Hughes, M. Cameron, and K. D. Crowley, "Structural variations in natural F, OH, and Cl apatites," *Am. Miner.*, 74 [7-8] 870-76 (1989).

[230]T. K. Ekstrom, "Synthetic and natural chlorine-bearing apatite," *Contrib. Mineral. Petrol.*, 38 [4] 329-38 (1973).

[231]H.-S. Ryu, H.-J. Youn, K. Sun Hong, B.-S. Chang, C.-K. Lee, and S.-S. Chung, "An improvement in sintering property of β-tricalcium phosphate by addition of calcium pyrophosphate," *Biomaterials*, 23 [3] 909-14 (2002).

[232]S. Kannan, A. F. Lemos, J. H. G. Rocha, and J. M. F. Ferreira, "Characterization and mechanical performance of the Mg-stabilized beta-$Ca_3(PO_4)_2$ prepared from Mg-substituted Ca-deficient apatite," *J. Am. Ceram. Soc.*, 89 [9] 2757-61 (2006).

[233]S. Kannan, I. A. F. Lemos, J. H. G. Rocha, and J. M. F. Ferreira, "Synthesis and characterization of magnesium substituted biphasic mixtures of controlled hydroxyapatite/beta-tricalcium phosphate ratios," *J. Solid State Chem.*, 178 [10] 3190-96 (2005).

[234]R. Z. LeGeros, "Biological and synthetic apatites," pp. 3-28 in *Hydroxyapatite and related materials*. Edited by P. W. Brown and B. Constantz. CRC Press, Boca Raton, FL, (1994).

[235]D. K. Smith, "Calcium phosphate apatites in nature," pp. 29-44 in *Hydroxyapatite and related materials*. Edited by P. W. Brown and B. Constantz. CRC Press, Boca Raton, FL, (1994).

[236]E. Dykes and J. C. Elliott, "Occurrence of chloride ions in apatite lattice of Holly Springs hydroxyapatite and dental enamel," *Calcified Tissue Research*, 7 [3] 241-& (1971).

[237]M. Schlosser and H.-J. Kleebe, "Vapor Transport Sintering of Porous Calcium Phosphate Ceramics," *J. Am. Ceram. Soc.*, 95 [5] 1581-87 (2012).

[238]D. W. Readey, J. Lee, and T. Quadir, "Vapor transport and sintering of ceramics," pp. 115-36 in *Sintering and heterogeneous catalysis*. Edited by G. C. Kuczynski, A. E. Miller, and G. A. Sargent. Plenum Press, New York and London, (1984).

[239]I. M. Lifshitz and V. V. Slyozov, "The kinetics of precipitation from supersaturated solid solutions," *J. Phys. Chem. Solids*, 19 [1-2] 35-50 (1961).

[240]C. Wagner, "Theorie der Alterung von Niederschlägen durch Umlösen (Ostwald-Reifung)," *Zeitschrift Fur Elektrochemie*, 65 [7-8] 581-91 (1961).

[241]C. Greskovich and K. W. Lay, "Grain-growth in very porous Al_2O_3 compacts," *J. Am. Ceram. Soc.*, 55 [3] 142-46 (1972).

[242]K. Sudarsanan, R. A. Young, and A. J. C. Wilson, "Structures of some cadmium apatites $Cd_5(MO_4)_3X$. 1. Determination of structures of $Cd_5(VO_4)_3I$, $Cd_5(PO_4)_3Br$, $Cd_5(AsO_4)_3Br$ and $Cd_5(VO_4)_3Br$," *Acta Crystallogr. Sect. B-Struct. Commun.*, 33 [OCT] 3136-42 (1977).

[243]A. J. C. Wilson, K. Sudarsanan, and R. A. Young, "Structures of some cadmium apatites $Cd_5(MO_4)_3X$. 2. Distributions of halogen atoms in $Cd_5(VO_4)_3I$, $Cd_5(PO_4)_3Br$, $Cd_5(AsO_4)_3Br$, $Cd_5(VO_4)_3Br$ and $Cd_5(PO_4)_3Cl$," *Acta Crystallogr. Sect. B-Struct. Commun.*, 33 [OCT] 3142-54 (1977).

[244]G. Baud, J. P. Besse, G. Sueur, and R. Chevalier, "Structure of new rhenium apatite similar to voluminous anions - $Ba_{10}(ReO_5)_6X_2$ (X=Br, I)," *Mater. Res. Bull.*, 14 [5] 675-82 (1979).

[245]M. Ode, T. Suzuki, S. G. Kim, and W. T. Kim, "Phase-field model for solidification of Fe–C alloys," *Science and Technology of Advanced Materials*, 1 [1] 43-49 (2000).

[246]W. Eysel and D. M. Roy, "Topotactic reaction of aragonite to hydroxyapatite," *Z. Kristall.*, 141 [1-2] 11-24 (1975).

[247]H. Ohgushi, "Coral derived porous framework having different chemical compositions as a scaffold for osteoblastic differentiation," *Porous Materials for Tissue Engineering*, 250 209-20 (1997).

[248]C. M. Zaremba, D. E. Morse, S. Mann, P. K. Hansma, and G. D. Stucky, "Aragonite-hydroxyapatite conversion in gastropod (abalone) nacre," *Chem. Mat.*, 10 [12] 3813-24 (1998).

[249]M. A. Araiza, J. Gomez-Morales, R. R. Clemente, and V. M. Castano, "Conversion of the echinoderm Mellita eduardobarrosoi calcite skeleton into porous hydroxyapatite by treatment with phosphated boiling solutions," *J. Mater. Synth. Process*, 7 [4] 211-19 (1999).

[250]A. Kasioptas, C. Perdikouri, C. V. Putnis, and A. Putnis, "Pseudomorphic replacement of single calcium carbonate crystals by polycrystalline apatite," *Mineral. Mag.*, 72 [1] 77-80 (2008).

[251]J. Hu, J. J. Russell, B. Ben-Nissan, and R. Vago, "Production and analysis of hydroxyapatite from Australian corals via hydrothermal process," *J. Mater. Sci. Lett.*, 20 [1] 85-87 (2001).

[252]J. H. G. Rocha, A. F. Lemos, S. Agathopoulos, S. Kannan, P. Valerio, and J. M. F. Ferreira, "Hydrothermal growth of hydroxyapatite scaffolds from aragonitic cuttlefish bones," *J. Biomed. Mater. Res. Part A*, 77A [1] 160-68 (2006).

[253]A. Putnis, "Mineral Replacement Reactions," pp. 87-124 in *Thermodynamics and Kinetics of Water-Rock Interaction,* Vol. 70. *Reviews in Mineralogy & Geochemistry*. Edited by E. H. Oelkers and J. Schott. Mineralogical Society of America, Chantilly, (2009).

[254]A. Bigi, E. Foresti, R. Gregorini, A. Ripamonti, N. Roveri, and J. S. Shah, "The role of magnesium on the structure of biological apatites," *Calcif. Tissue Int.*, 50 [5] 439-44 (1992).

[255]S. Baravelli, A. Bigi, A. Ripamonti, N. Roveri, and E. Foresti, "Thermal behaviour of bone and synthetic hydroxyapatites submitted to magnesium interaction in aqueous medium," *J. Inorg. Biochem.*, 20 [1] 1-12 (1984).

[256]A. Bigi, F. Marchetti, A. Ripamonti, N. Roveri, and E. Foresti, "Magnesium and strontium interaction with carbonate-containing hydroxyapatite in aqueous medium," *J. Inorg. Biochem.*, 15 [4] 317-27 (1981).

[257]I. R. Gibson and W. Bonfield, "Preparation and characterization of magnesium/carbonate co-substituted hydroxyapatites," *J. Mater. Sci.-Mater. Med.*, 13 [7] 685-93 (2002).

[258]W. L. Suchanek, K. Byrappa, P. Shuk, R. E. Riman, V. F. Janas, and K. S. TenHuisen, "Preparation of magnesium-substituted hydroxyapatite powders by the mechanochemical-hydrothermal method," *Biomaterials*, 25 [19] 4647-57 (2004).

[259]D. Clement, J. M. Tristan, M. Hamad, P. Roux, and J. C. Heughebaert, "The Mg^{2+}/Ca^{2+} substitution in beta-tricalcium ortho-phosphate," *J. Solid State Chem.*, 78 [2] 271-80 (1989).

[260]S. Kannan, F. Goetz-Neunhoeffer, J. Neubauer, A. H. S. Rebelo, P. Valerio, and J. M. F. Ferreira, "Rietveld Structure and In Vitro Analysis on the Influence of Magnesium in Biphasic (Hydroxyapatite and beta-Tricalcium Phosphate) Mixtures," *J. Biomed. Mater. Res. Part B*, 90B [1] 404-11 (2009).

[261]R. Enderle, F. Gotz-Neunhoeffer, M. Gobbels, F. A. Muller, and P. Greil, "Influence of magnesium doping on the phase transformation temperature of beta-TCP ceramics examined by Rietveld refinement," *Biomaterials*, 26 [17] 3379-84 (2005).

[262]R. M. Wilson, J. C. Elliott, and S. E. P. Dowker, "Rietveld refinement of the crystallographic structure of human dental enamel apatites," *Am. Miner.*, 84 [9] 1406-14 (1999).

[263]Y. Suetsugu, Y. Takahashi, F. P. Okamura, and J. Tanaka, "Structure analysis of A-type carbonate apatite by a single-crystal X-ray diffraction method," *J. Solid State Chem.*, 155 [2] 292-97 (2000).

[264]T. I. Ivanova, O. V. Frank-Kamenetskaya, A. B. Kol'tsov, and V. L. Ugolkov, "Crystal structure of calcium-deficient carbonated hydroxyapatite. Thermal decomposition," *J. Solid State Chem.*, 160 [2] 340-49 (2001).

[265]J. V. Rau, S. N. Cesaro, D. Ferro, S. M. Barinov, and I. V. Fadeeva, "FTIR study of carbonate loss from carbonated apatites in the wide temperature range," *J. Biomed. Mater. Res. Part B*, 71B [2] 441-47 (2004).

[266]R. Murugan, S. Ramakrishna, and K. P. Rao, "Nanoporous hydroxy-carbonate apatite scaffold made of natural bone," *Mater. Lett.*, 60 [23] 2844-47 (2006).

[267]F. A. Kroger and H. J. Vink, "Relations between the concentrations of imperfections in crystalline solids," *Solid State Physics-Advances in Research and Applications*, 3 307-435 (1956).

[268]J. C. Elliott, D. W. Holcomb, and R. A. Young, "Infrared determination of the degree of substitution of hydroxyl by carbonate ions in human dental enamel," *Calcif. Tissue Int.*, 37 [4] 372-75 (1985).

[269]S. E. P. Dowker and J. C. Elliott, "Infrared study of trapped carbon-dioxide in thermally treated apatites," *J. Solid State Chem.*, 47 [2] 164-73 (1983).

[270]D. W. Holcomb and R. A. Young, "Thermal decomposition of human tooth enamel," *Calcif. Tissue Int.*, 31 [3] 189-201 (1980).

[271]A. K. Seth, M. R. Geringer, S. J. Hong, K. P. Leung, R. D. Galiano, and T. A. Mustoe, "Comparative analysis of single-species and polybacterial wound biofilms using a quantitative, in vivo, rabbit ear model," *PLoS One*, 7 [8] e42897 (2012).

[272]M. Guzman, J. Dille, and S. Godet, "Synthesis and antibacterial activity of silver nanoparticles against gram-positive and gram-negative bacteria," *Nanomed.-Nanotechnol. Biol. Med.*, 8 [1] 37-45 (2012).

[273]D. R. Gaskell, "Introduction to metallurgical thermodynamics," pp. 611. Taylor & Francis, Washington D.C. (1981).

[274]W. D. Kingery and M. Berg, "Study of the initial stages of sintering solids by viscous flow, evaporation-condensation, and self-diffusion," *J. Appl. Phys.*, 26 [10] 1205-12 (1955).

[275]H. den Hartog, D. O. Welch, and B. S. H. Royce, "The diffusion of calcium, phosphorus, and OD-ions in fluorapatite," *Phys. Status Solidi*, 53 [1] 201-212212 (1972).

[276]S. V. Dorozhkin, "Dissolution mechanism of calcium apatites in acids: A review of literature," *World Journal of Methodology*, 2 [1] 1-17 (2012).

[277]P. A. O'Day and D. Vlassopoulos, "Mineral-Based Amendments for Remediation," *Elements*, 6 [6] 375-81 (2010).

[278]P. Miretzky and A. Fernandez-Cirelli, "Phosphates for Pb immobilization in soils: a review," *Environmental Chemistry Letters*, 6 [3] 121-33 (2008).

[279]J. Reichert and J. G. P. Binner, "An evaluation of hydroxyapatite-based filters for removal of heavy metal ions from aqueous solutions," *Journal of Materials Science*, 31 [5] 1231-41 (1996).

9. Appendix: Equilibrium Partial Pressures for Various Vapor Transport Sintering Systems

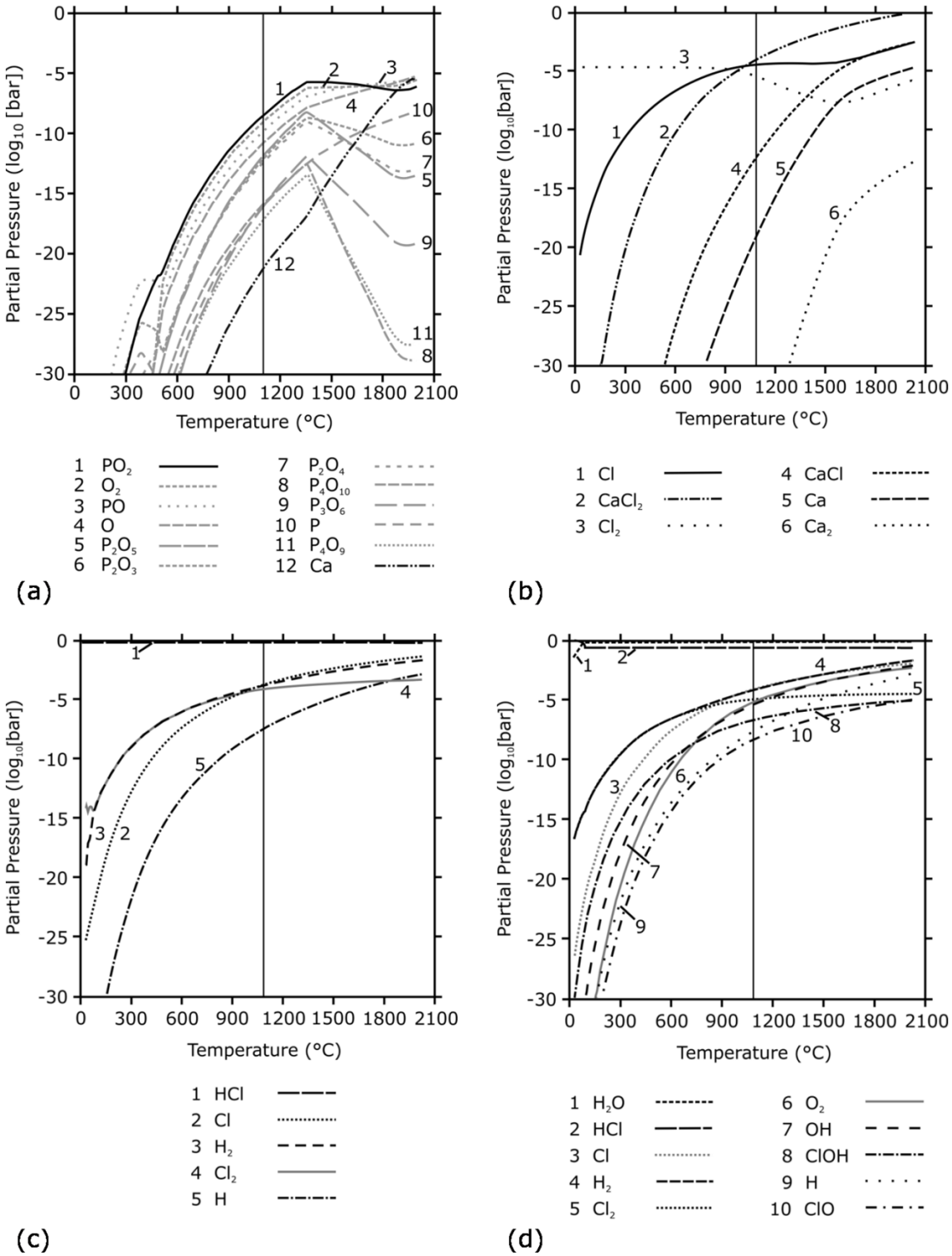

Figure 50: Equilibrium partial pressures over (a) tricalcium phosphate (free sintering condition), (b) $CaCl_2$, (c) HCl_{gas}, (d) hydrochloric acid (37%); the system pressure is 1 bar. Continued on next page.

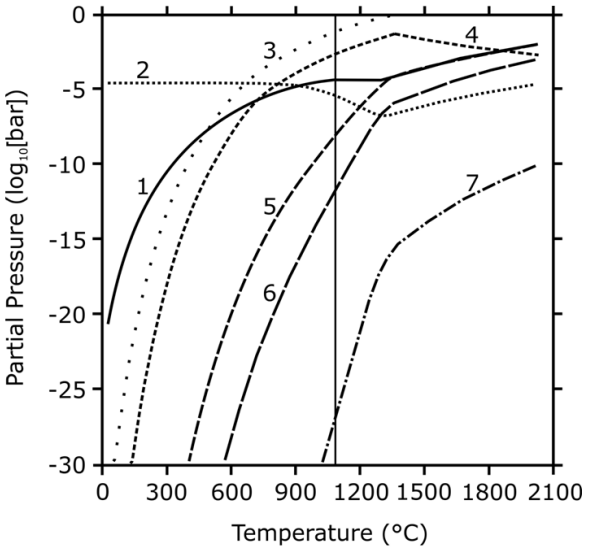

(e)

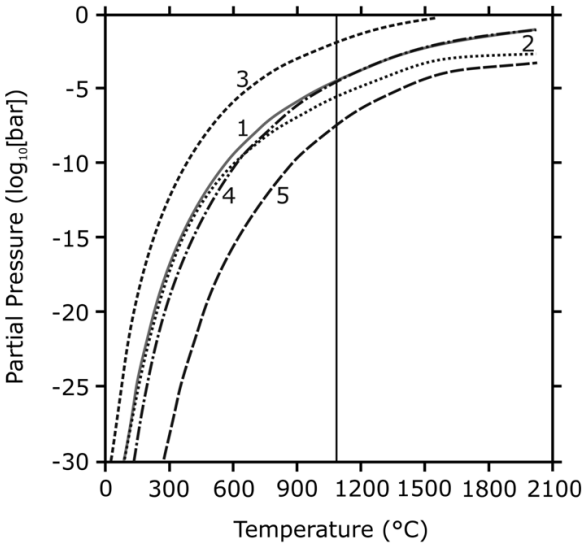

(f)

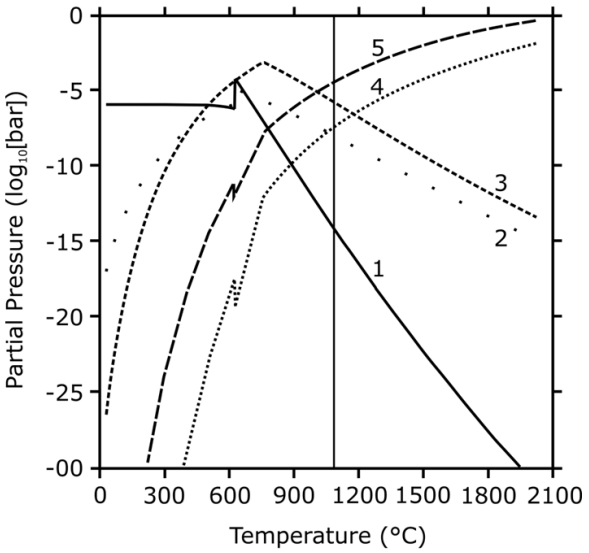

(g)

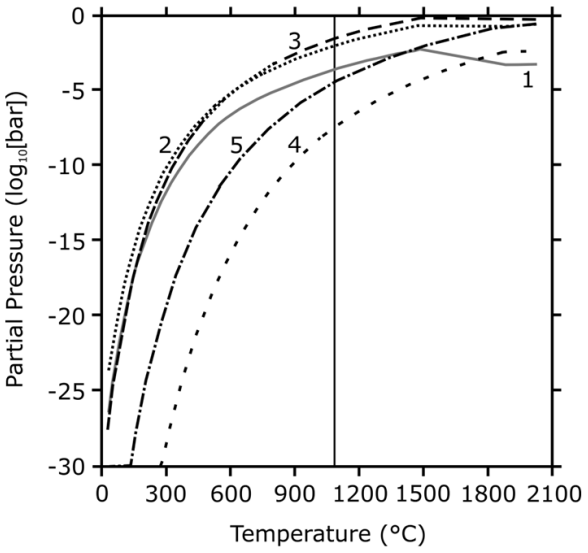

(h)

Figure 50 (cont'd): Partial pressures over (e) $MgCl_2$, (f) AgCl, (g) AgBr and (h) AgI; the system pressure is 1 bar.

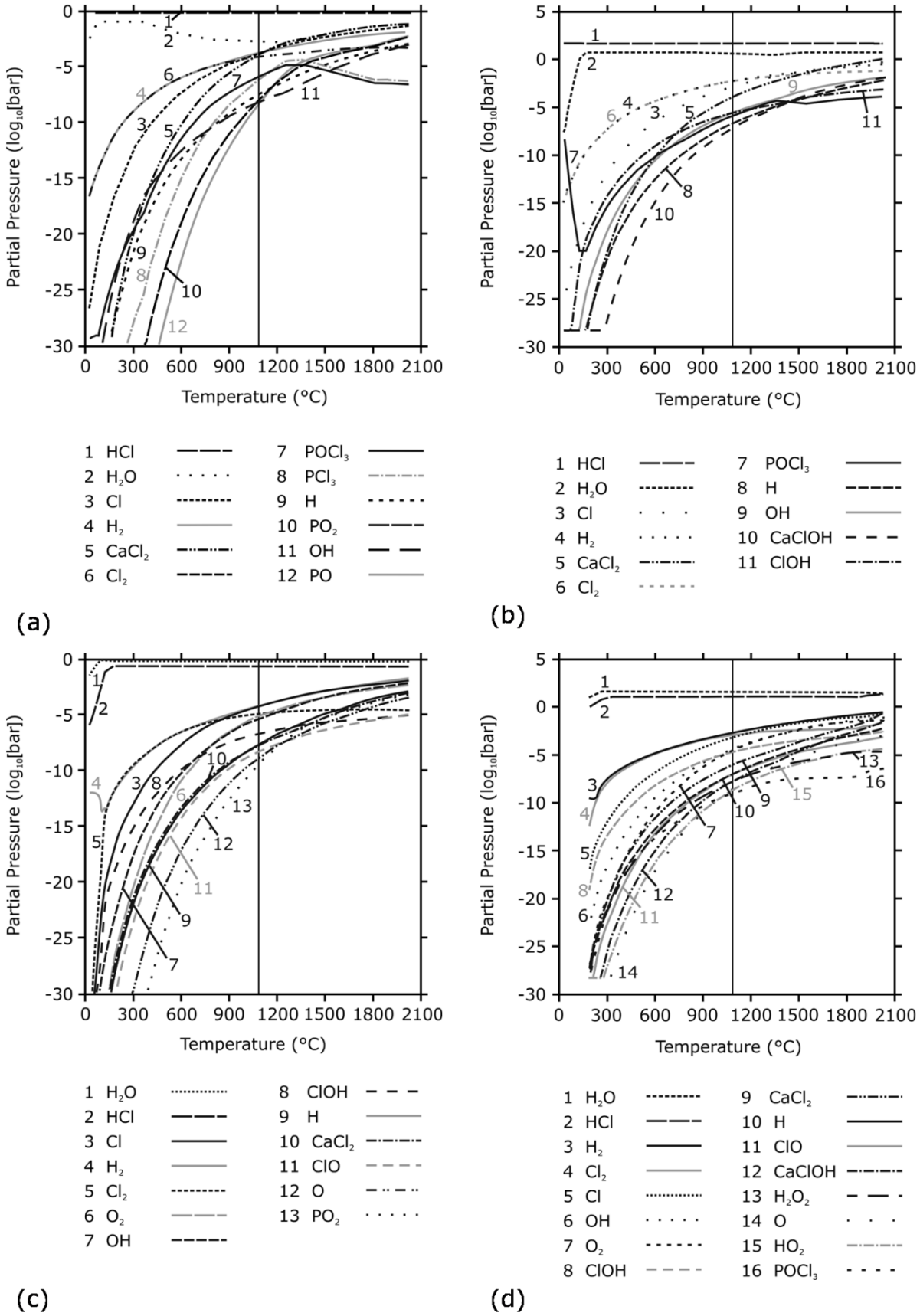

Figure 51: Partial pressures for the sintering system TCP–HCl_{gas} at system pressures of (a) 1 bar and (b) 50 bar; for TCP–hydrochloric acid (37%) at (c) 1 bar and (d) 50 bar.

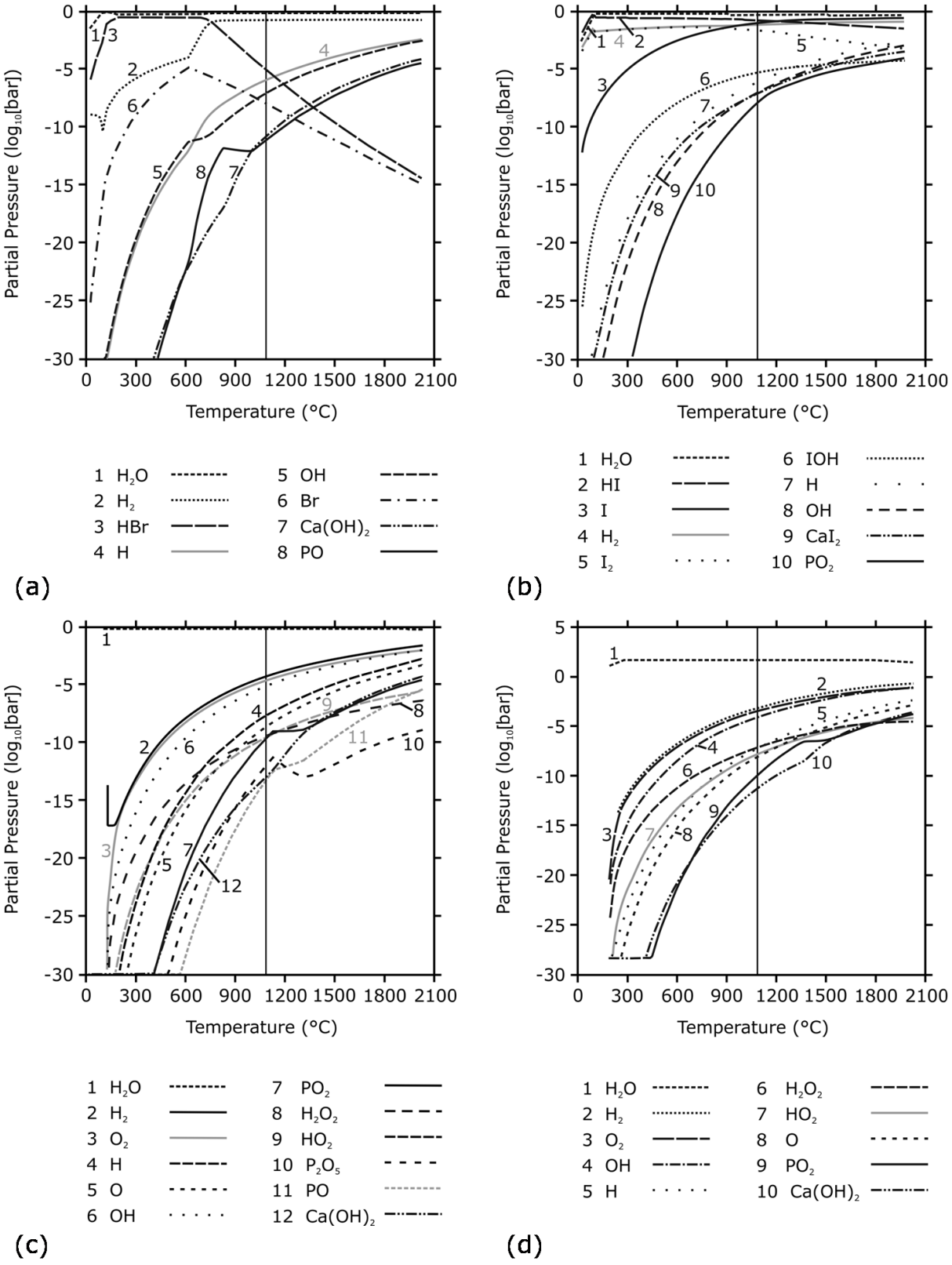

Figure 52: Partial pressures for the sintering systems (a) TCP–bromide acid (47%), (b) TCP-iodine acid (57%), both at 1 bar system pressure; for TCP–H_2O at system pressures of (c) 1 bar and (d) 50 bar.

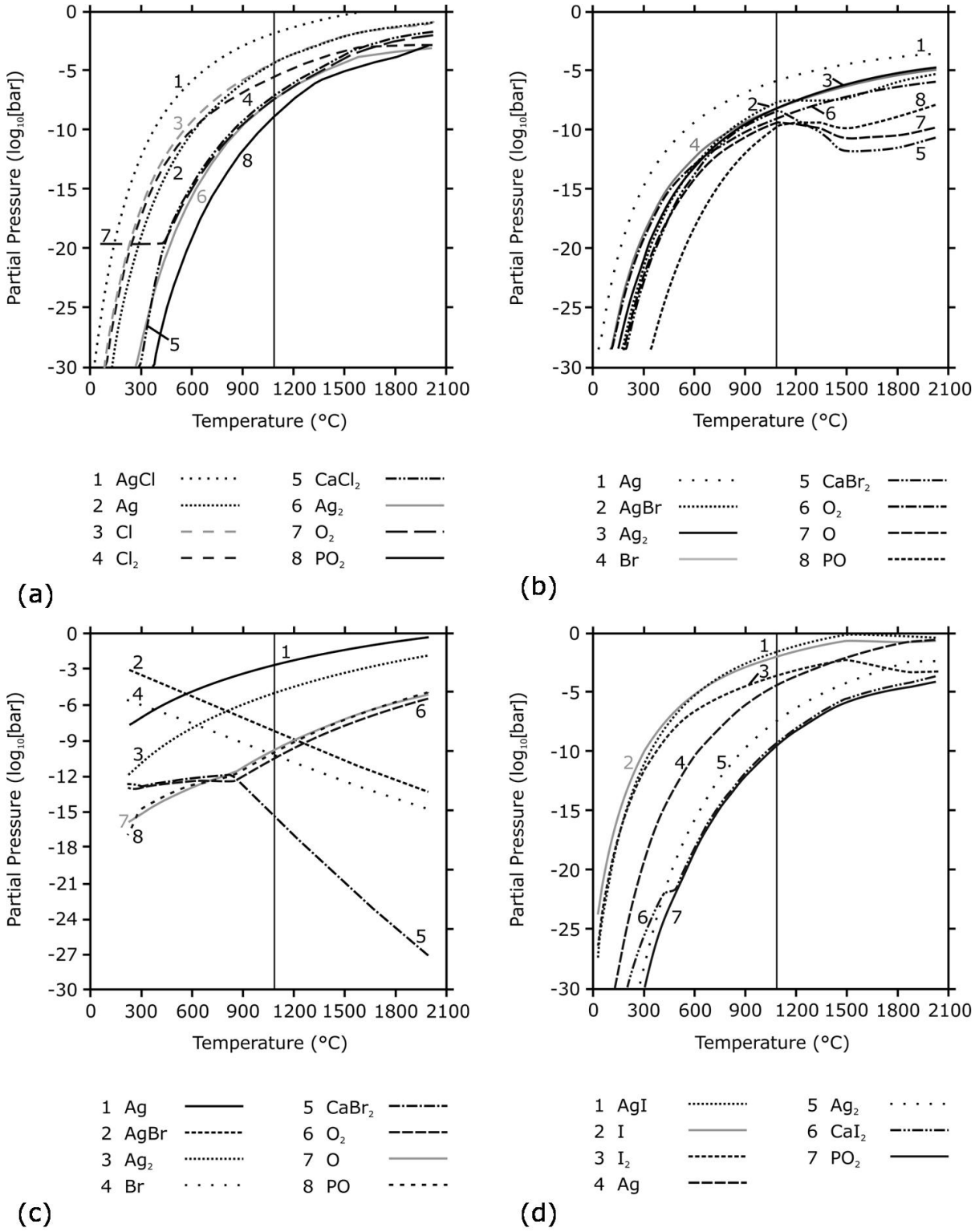

Figure 53: Partial pressures for the sintering systems TCP–AgCl at system pressures of (a) 1 bar, (b) 50 bar; (c) for TCP–AgBr and (d) TCP–AgI, both at 1 bar system pressure.

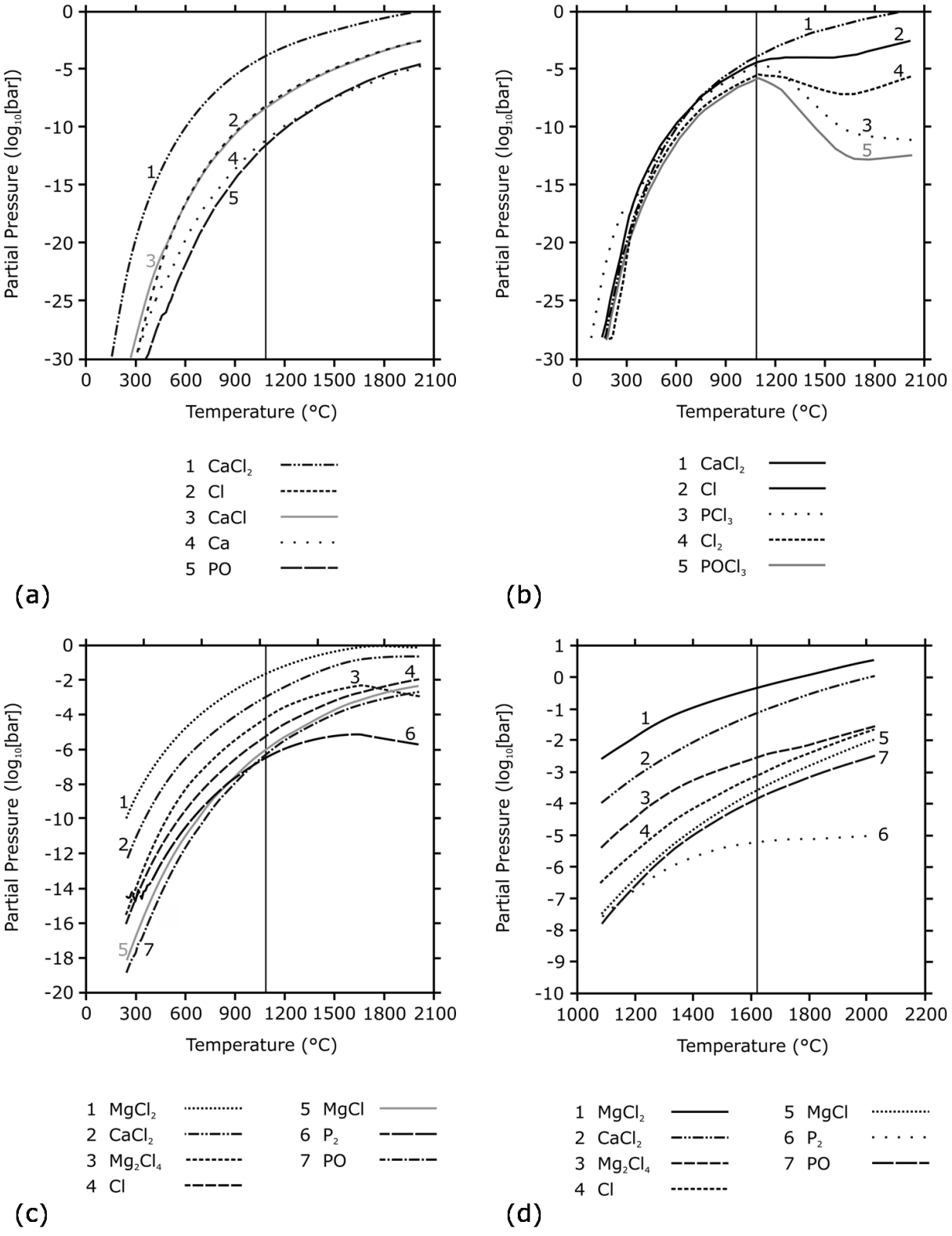

Figure 54: Partial pressures for the sintering system TCP–$CaCl_2$ at (a) 1 bar and (b) 50 bar; for TCP–$MgCl_2$ at (c) 1 bar and (d) 50 bar.

Acknowledgements

What we need most in life is someone who persuades us to do what we are capable of.

R. W. Emerson

Feeling indebted to many people that supported me in one way or the other, I wish to express my gratitude

…to Achim Kleebe for his continuous efforts of persuasion, his encouragement and trust.

…to Christoph Schüth, Wolfgang Ensinger and Olivier Guillon who readily agreed to burden themselves with the task of evaluating my thesis.

…to Fanny Schultheiß, my congenial roommate, and Ingo Sethmann. With both I spent quite some memorable days and evenings.

…to Stefania Hapis, Katharina Nonnenmacher, Marina Zakhozheva, Stefan Lauterbach, Mathis Müller and Horst Purwin, whose great company I valued no less than their helpful suggestions and practical support.

…to Tanuja Bammidi, Ulla Hauf, Wibke Krücker, Katharina Schütze, Kerstin Stricker, Ivo Nemetz, Timo Prenzer, Sven Schildt, Sehab Uddin and David Wiesemann with whom I collaborated in laboratory and office.

…to Stefan Weinbruch, Martin Ebert and Konrad Kandler who unreservedly supported my work at the ESEM lab.

…to Thomas Dirsch, ever-helpful and knowledgeable, though never impressed by convention.

…to Branimir Segvic and Norbert Laskowski, colleagues from the working group of Rafael Ferreiro Mählmann, for help and advice on matters of XRD, XRF and beyond.

…to Ingrid Hirsmüller who untiringly drew and redrew many of the figures provided in this volume.

…to Angelika Willführ and Astrid Zilz for patiently responding to my many requests.

…to Ulrike Kunz, Bernd Dreieicher and Holger Scheibner for sharing their long experience with me.

…to Petra Kraft for making inaccessible publications accessible.

…to Felicitas Pfeifer and Sabrina Fröls, two most welcoming and thorough researchers at the Department of Biology.

…to Sandra Saenze and Toni Groß, colleagues from the working group of Christian Hess at the Department of Chemistry, who initiated me into the DRIFTS technique.

…to Hans Seifert, Damian Cupid and all other members of the Thermophysics and Thermodynamics group at the KIT for an enjoyable and successful collaboration.

…to Caner Durucan and his working group for making my stay at the Middle East Technical University in Ankara productive, stimulating and simply unforgettable.

…to Christine Jamin, Jami Winzer and all the strong women on our faculty's gender equality board.

…to Jörg Faßbinder and Detlef Köpsel whose benevolence shaped my career, but which I best remember for their restless curiosity and keen wit.

…to my family on whose guidance and patient support I rest.

…to Jan-Helge, my companion and jester-in-chief.

…to all my friends living in Darmstadt and beyond, making my days fly by.

…to all the ones that I have omitted without bad faith, although acknowledgement would be due.

Der Lebenslauf ist in der Online-Verison aus Gründen des Datenschutzes nicht enthalten.

Der Lebenslauf ist in der Online-Verison aus Gründen des Datenschutzes nicht enthalten.

Publikationsliste

Fassbinder J., Becker H., and Schlosser M.: Magnetic prospection. In: Vatandoust A., Parzinger H., Helwing B. (Hrsg.): Early mining and metallurgy on the western central Iranian Plateau. Archäologie in Iran und Turan 9, Berlin, 19-27 (2011).

Schlosser M., Gebhard R., and Pernicka E.: Beobachtungen zu Herstellung, Gebrauch und Reparaturen urnenfelderzeitlicher Bronzegefäße. Restaurierung und Archäologie 4, Mainz, 1-14 (2011).

Schlosser M., Kleebe H.-J.: Vapor Transport Sintering of Porous Calcium Phosphate Ceramics. Journal of the American Ceramic Society, Vol. 95(5), 1581–1587 (2012).

Schlosser M., Froels S., Schultheiss S., Hauf U., Sethmann I., Pfeifer F., and Kleebe H.-J.: Combined hydrothermal conversion and vapor transport sintering of AgCl-modified calcium phosphate scaffolds. Journal of the American Ceramic Society (eingereicht).

Schultheiss S., Sethmann I., Schlosser M., and Kleebe H.-J.: Pseudomorphic transformation of Ca/Mg carbonates with focus on dolomite conversion. Mineralogical Magazine (eingereicht).

Konferenzbeiträge

Schlosser M., Berthold Chr., Pernicka E., Gebhard R.: Malachit – ein Echtheitskriterium? Zerstörungsfreie µXRD² an einem Gefäßhort unbekannter Herkunft. *Posterpräsentation bei "Archäometrie und Denkmalpflege 2009", 25.-28. März 2009, München, Deutschland.*

Schlosser M., Kleebe H.-J.: Gas phase sintering of biphasic calcium phosphate (BCP) scaffolds for bone replacement applications. *Posterpräsentation bei "JuniorEuromat 2010", 26.-30. Juli 2010, Lausanne, Schweiz.*

Schlosser M., Kleebe H.-J.: Gas phase sintering of hydroxyapatite/beta-tricalcium phosphate scaffolds for bone replacement applications. *Vortrag bei "Materials Science and Engineering 2010", 24.-26. August 2010, Darmstadt, Deutschland.*

Schlosser M., Kleebe H.-J.: Vapor transport sintering of biphasic calcium phosphate ceramics in AgCl atmosphere for bone replacement applications. *Posterpräsentation bei "EnCAMP 2011", 25.-29. Mai 2011, Kappadokien, Türkei.*

Schlosser M., Kleebe H.-J.: AgCl-sintering of biogenic calcium phosphate scaffolds. *Posterpräsentation bei der "Jahrestagung der Deutschen Gesellschaft für Biomaterialien", 01.-03. November 2012, Hamburg, Deutschland.*

Forschungsaufenthalt

Besuch der Arbeitsgruppe von Dr. Caner Durucan, Assistant Professor of Metallurgical and Materials Engineering, Middle East Technical University, Ankara, Türkei. *Förderung im Rahmen des IntenC-Programms des Bundesministeriums für Bildung und Forschung (BMBF), 23. April - 05. Juni 2010.*